Computational Modelling of Electrohydrodynamic Jetting (Taylor Cone Formation, Dripping & Jet Evolution): Case Study of Electrospinning

A thesis submitted in partial fulfilment of
the requirements for the degree of

Doctor of Philosophy
By
Babatunde Aramide

Supervised by:
Professor Yiannis Ventikos
and
Professor Suwan Jayasinghe

Department of Mechanical Engineering

University College London

Torrington Place, London WC1E 7JE

United Kingdom

March 2022

DECLARATION

I, Babatunde Aramide, confirm that the work presented in this thesis is my own. Where information has been derived from other sources, I confirm that this has been indicated in the thesis.

[redacted]

Aramide Babatunde

ABSTRACT

Over the years, there has been growing interest in the phenomena that arise during fluid flow and electric field interactions. Manipulation of the flow and operating parameters gives rise to unique flow patterns that can be adapted for various applications ranging from field-like atomic ionization, microfluidics, electrospraying, electrospinning etc. This study aims to look at the critical phases of some of these processes and postulate how the electric field influences the fluid flow and vice versa. The electrohydrodynamic (EHD) equations coupled with the electrostatic equation describe this process mathematically and have been examined numerically in this study.

Physical properties of water were used for the liquid medium, enveloped by air as applicable. The choice of media does not diminish the generality of the model. Both the liquid and the gaseous phases are active and interact via their contact surface. The conservation of mass and momentum, with appropriate additional force terms coming from the presence of the electric field (i.e., the EHD system) and the electrostatic equations were coupled together and solved using the Finite Volume method to simulate the flow- reflecting the effect of the fluid flow on the electric field and vice versa. The Volume of Fluid (VOF) technique was used to track the free surface. The solution procedure was such that the electric body forces were calculated from the electrostatic equation and then included in the Navier-Stokes equation to predict the velocity field and other fluid parameters. No initial shape was assumed for the fluid shape and charge distribution.

We have conducted a series of simulations, aiming to establish the model, to obtain test results and to examine, the influence of some of the parameters at play. Samples of such results obtained are presented in the relevant chapter of this report. Axisymmetric models were constructed, highlighting interesting features of these flows, like the formation of a Taylor cone, jet evolution, droplet break-up and fibre extrusion. This thesis focuses on some features from the early stages of the flows examined. Results agree well with both existing experimental and computational reports. Emphasis is placed on the generality methodology developed, that can handle geometric configurations of arbitrary complexity and any combination of liquid/gas. The interaction of the electric field with the fluid, as studied and analysed numerically in this work, offers great potential for control of emerging features.

IMPACT STATEMENT

This dissertation investigated the electrospinning phenomenon in the cone-jet region. It highlighted the capability of the adapted methodology by demonstrating cases like the formation of a Taylor cone, jet evolution and droplet breakup. The methodology presented handled two-dimensional and axisymmetric configurations of high levels of realism and is capable of solving for full 3D configurations in a completely straightforward manner.

The results obtained compared well both with experimental and computational works - both for the flow profiles and distribution of the flow field characteristics. The effect of flow rate, voltage and rheological properties (including viscosity, conductivity, and permittivity) has been accurately captured by the computations made so far.

The axisymmetric model has shown results that compare well with literature. It has been shown that the model developed has the capability to handle the complex multiphase EHD problem very well. We have been able to depict the coupling between the electric field and the flow field- showing that the electric field influences the flow and the flow influences the electric field as well. The use of the VOF technique has proved suitable for capturing the fluid interface, alongside structured meshing; as against unstructured meshing.

This work paves way for economical means of predicting the key features of electrospun and electrosprayed materials. It also provides a base-model for further research to explore the adaptability of this model to co-axial EHD problems like co-axial electrospraying and electrospinning.

Economically, the results of this work have great importance in fields like ink-jet printing where the control of jetting and jet orientation is very important. Researchers will find the methodology presented invaluable to expand EHD research.

PUBLICATIONS AND CONFERENCES

Journal Article

- B. Aramide, A. Kothandaraman, M. Edirisinghe, S. N. Jayasinghe, and Y. Ventikos, “General Computational Methodology for Modeling Electrohydrodynamic Flows: Prediction and Optimization Capability for the Generation of Bubbles and Fibers,” Langmuir, vol. 35, no. 31, 2019.
- B. Aramide, S. N. Jayasinghe, and Y. Ventikos Insight into the Roles of Conductivity and Dielectric Constant in EHD Flows (in preparation)

Conference Series

- B. Aramide, S. N. Jayasinghe, and Y. Ventikos ‘Fluid Viscosity and Corresponding Effects on Fluid flow, Velocity Magnitude and Electric Field Distribution in Electrohydrodynamic Jetting. (Accepted for publication in Journal of Physics Conference Series.)

Conference Presentations

- B. Aramide, S. N. Jayasinghe, and Y. Ventikos ‘Fluid Viscosity and Corresponding Effects on Fluid flow, Velocity Magnitude and Electric Field Distribution in Electrohydrodynamic Jetting. Electrostatic 2019, Institute of Physics, Manchester, April 2019 (Poster Presentation)
- B. Aramide, S. N. Jayasinghe, and Y. Ventikos, ‘CFD Simulation of Taylor Cone Formation, Jet Evolution and Whipping Instability in Electrohydrodynamic Flows’. 8th World Congress of Biomechanics, July 2018. (Poster Presentation)

- B. Aramide, S. N. Jayasinghe, and Y. Ventikos, Departmental PhD conference, Department of Mechanical Engineering, UCL, London, UK, June 2016 (Poster and Technical Presentation).
- B. Aramide, S. N. Jayasinghe, and Y. Ventikos, Departmental PhD conference, Department of Mechanical Engineering, UCL, London, UK, June 2015 (Poster and Technical Presentation).

ACKNOWLEDGEMENTS

I would like to appreciate the efforts of individuals and organizations that have contributed to the completion of this work in every way possible.

My first gratitude goes to my supervisor, Prof Yiannis Ventikos for his tutoring, time, advice and vote of confidence throughout the project. He gave the needed attention when I needed him. He taught me how to write (I am still getting better). He took me through how to think about a scientific problem. When I felt like dropping, he told me “it is possible!”

Secondly. I want to appreciate my second supervisor, Prof Suwan Jayasinghe, for always lending me listening ears when I needed him. My academic history will not be complete with him.

To all members of the Fluidics and Biocomplexity Group, you are awesome. I will never forget the help of Dr John Vardakis, your wise counsels and tips gave me a lot of confidence and always pushed me to work harder- you were just like a big brother!

In addition, I would like to acknowledge the financial support by the PTDF– Petroleum Technology Development Fund, under the umbrella of the Federal Government of Nigeria, on whose sponsorship I studied at the University College London. Absolutely none of these will be possible without their funding.

My profound gratitude goes to my family, my Dad and Mum, and my sibling Dr Kola, Tosin and Afolabi Aramide for being there for me, always looking out and

checking for the progress of my studies. I love you all. Not forgetting my group of friends- Tanidabi, Deji, Funmibi, Dara, John, Tosin, I want to say a big thank you to you all.

Finally, to a very important family to me, the Dream Centre family under the leadership of my Coach, Rev. and Rev. (Mrs) Olusola Areogun, I want to say a big thank you for your prayers and advices all the time. I pulled through because of you.

Contents

NOMENCLATURE

SYMBOLS

a, b	Link coefficients
d	Capillary to collector distance
D	Volume charge density
d_c	Local cell dimension
D_d	Droplet diameter
d_n	Capillary inner diameter
e	Exponential
E	Electric field intensity
F	Fluid fraction
F_g	Gravitational force
F_e	Finite electric force
F_γ	Total Capillary force
$F_{dielectric}$	Virtual dielectric force
f^e	Electric force density
f_k^e	Kelvin force density
f_{KH}^e	Korteweg-Helmhotz force density
F^e	Resultant force
f_e	Coulombic force
g	Gravitational force
G	Interfacial charge density
H	Air gap distance
I	Identity matrix
i	Total current
i_c	Convective current

i_o	Ohmic Current
$\vec{J}$	Electric Charge field
K	Conductivity
L_{cp}	Length of capillary tube
$\dot{m}$	Mass flow rate
n	Normal to surface
$\hat{n}_w$	Unit normal of contact angle directed to wall
p	Hydrostatic pressure
P	Corrected value of pressure field
P'	Pressure correction
P^*	Guessed value of Pressure
P_r	Polarization density
q	Free surface charge density
q_0	Free charge density at $t = 0$
Q	Flow rate
r	Radius of droplet
r_0	Radius of fluid meniscus
r_p	Density ratio of fluids
R_{cp}	Internal Radius of capillary tip
S	Source term
Δt	Time step
Δt_f	False time step
Δt_c	Maximum allowable timestep in a cell
t	Time
$\hat{t}_w$	Unit tangent of contact angle directed to the wall
$T_{n,}T_t$	Normal and Tangential electrical stresses
T^e	Maxwell Stress Tensor
T_k^e	Maxwell Stress Tensor corresponding to Kelvin force density

T_{KH}^{e}	Maxwell Stress Tensor corresponding to Korteweg-Helmhotz force density
$\vec{u}$	Velocity vector field
u	Corrected value of velocity field
u'	Velocity correction
u^{*}	Guessed value of velocity
U,V,W	Velocity in the x, y, z direction
V	Applied voltage
V_c	Critical value of applied voltage for jetting
$\vec{V}$	Velocity field
$\vec{V}_f$	Velocity vector of the fluid
$\vec{V}_w$	Velocity vector of the wall
v	Applied Voltage on dielectric fluid

GREEK SYMBOLS

ε	Permittivity of medium
$\varepsilon_o, \varepsilon_l, \varepsilon_m$	Relative permittivity of free space, liquid and medium
Γ	Gamma function
ρ	Fluid density
γ	Surface tension of fluid
Υ	Geometric weighting function
λ	Under-relaxation factor
∇	Divergence
σ	Electrical Conductivity
ϕ, ϕ_{l}, ϕ_m	Electric Field Potential of liquid and medium
Θ	Calculated auxiliary variable with no relaxation
Θ^{new}	Updated value of auxiliary variable after relaxation
Θ^{*}	Current iteration value of auxiliary variable
θ	Contact angle

μ	Viscous stress
τ	Bulk relaxation time
T	Total resultant tangential force
χ	Fluid property
υ	Specific volume
$\bar{\upsilon}_c$	Local cell velocity

ABBREVIATIONS

BC	Boundary conditions
BEM	Boundary element method
CFD	Computational Fluid Dynamics
CGS	Conjugate gradient solver
CSF	Continuous surface force
DC	Direct Current
DMF	Dimethylformamide
DTF	Data transfer facility
EHD	Electrohydrodynamic
FDE	Finite difference equation
FVM	Finite volume method
GGD	Geometry grid definition
GMRES	Generalized minimum residual solver
GUI	Graphics user interface
H_2O	Water
KH	Korteweg-Helmhotz
NITER	Number of iterations
NSTEPS	Number of time steps
PEO	Polyethylene oxide
PLIC	Piecewise linear interface construction
PS	Polystyrene
PVA	Polyvinyl alcohol
PVC	Polyvinyl Chloride
PVDF	Polyvinylidene fluoride

SIMPLEC	Semi-implicit method for pressure linked equations- consistent
SiO_2	Silicon oxide
SLIC	Single Linear Interface Construction
THF	Tetrahydrofuran
TiO_2	Titanium oxide
VOF	Volume of fluid

LIST OF FIGURES

LIST OF TABLES

1. INTRODUCTION - Motivation, Scope, Aim and Objectives.

1.1 Preamble

There has been growing interest in the use of features generated through electrohydrodynamic processes, with applications adopted in areas like tissue engineering, absorption, filtration, printing, protective clothing, wound healing, material reinforcement, energy generation etc. Thavasi et al [1] also pointed out some other possible future use in areas like gas turbine and engine filters, nose masks, fuel cells, hydrogen gas storage, and artificial heart valves.

Electrohydrodynamics (EHD) involves studying the fluid motion induced by electrical fields [2], in other words, it deals with the interaction of fluid flow and electric fields [3]. It is an interdisciplinary field involving branches such as hydrodynamics, thermophysics, electrochemistry and electrostatics [4]. EHD transport phenomena are fundamental to a range of applications in engineering, including electrospray ionization, electrospinning, electrostatic printing, electrokinetic assays etc. [5]. The electrostatic field generated exerts additional electromechanical forces in the normal and tangential direction of the liquid [6].

Generally, this work is based on the use of Computational Fluid Dynamics techniques that include the multiphysics ability of a coupled EHD for two-phase flow. The fluid flow of the jet unto the grounded surface from an electrified capillary/emitter/nozzle results in a unique phenomenon: At a properly selected combination of the parameters including electrical, geometric and rheological ones, a conical meniscus leading to a very thin jet (relative to the nozzle diameter) is developed at the nozzle. This cone is called the *Taylor cone* [7]. This is the foundation upon which the process under investigation is predicated and the modelling is attempting to capture and examine. A typical illustration of the development of Taylor cone can be seen in Figure 1.1.

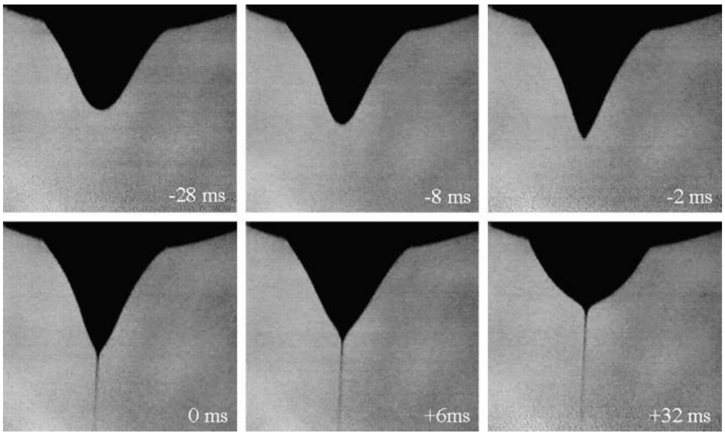

Figure 1.1- Evolution of the shape of a Fluid drop, showing Taylor cone [8]*. The time 0ms was taken as the frame when the first jet appears.*

This dissertation investigates the electrospinning phenomenon in the cone-jet region. It highlights the capability of the adapted methodology by demonstrating cases like the formation of a Taylor cone, jet evolution and droplet breakup. The methodology presented handles two-dimensional and axisymmetric configurations of high levels of realism and is capable of solving for full 3D configurations in a completely straightforward manner.

1.2 Motivation

Over time, the EHD process, though vast in its applications, has had a couple of drawbacks some of which form the motivation for this study/research. Researches have been carried out to address these challenges but not always with outright success. Some of these associated problems are highlighted below:

- The process and development of jet formation takes place in milliseconds and the jets are in the micrometre range, therefore it becomes challenging to study using conventional experimental process. This is particularly true when parameters inside the Taylor cone and jets are of interest. Computational modelling presents an opportunity to understand the physical process at time-scales and length-scales that are pertinent to the phenomena at play and with exquisite detail.
- Viswanadam and Chase [9] modified the electric field by positioning charged electrodes capable of altering the electric field and similarly, in their own work, Bellan and Craighead [10] investigated this by positioning electrodes between the tip and the grounded collector with the aim of suppressing the whipping mode of the jet. Yang et al [11], also modified the electric field using polyvinyl chloride (PVC) insulating tubes to facilitate concentrated and uniform distribution of electric field. Finally, in a recent patent by Barinov and Levon [12], jet control was achieved by the combination of magnets and using multiple collectors, with the magnetic field generated changing the direction of the jet stream. The problem of jet control in EHD has attracted a lot of studies to enhance oriented jets and align the jets in a pre-described pattern/layout.
- Issues of scale-up and mass production. The throughput achieved in EHD applications like electrospinning is rather low. This has called for different investigations on how to increase throughput. Many methods, especially the possibility of the needleless jetting system, have been employed [13]. A computational model will help to investigate the possibility of increasing throughput.
- Understand the effect of parameters. The effects of wide ranges of flow rates and electric fields for various fluids can be alternatively studied more conveniently by computer simulation methods.

- The interactions among fluid flow, electric field, fluid (both solution and environment) properties are difficult to interpret experimentally, but computational models, once validated, will enhance our understanding regarding the relationship among the underlying parameters.
- Finally, the dependence of jet formation and jet instability on process parameters and fluid properties along with the prediction of resulting jet under a new combination of parameters will be aided using this model.

1.3 Scope

This work focused on the use of computational modelling techniques to simulate the process of fibre formation. The model was built within the framework of an established multiphysics/multiscale solver (CFD-ACE+, ESI Group, Paris, France). Axisymmetric computations were conducted, which correspond to full 3D volumetric conditions but exclude the emergence of circumferentially variant features (for example, instabilities in the third dimension). The domain in this report accounts for the zone encapsulating the capillary needle and tip, the atmosphere and the collection plate.

1.4 Aim and Objectives

The aim of this thesis is to use computational simulation techniques to model the Electrohydrodynamic Jetting (including the Taylor Cone Formation, Dripping mode & Jet Evolution) using the case study of Electrospinning with the following specific objectives:

1. To propose a mathematical framework for the numerical simulation of the electrospinning process.
2. To carry out modelling and simulation of the process.

3. To investigate the effect of the EHD parameters (including the rheology properties of the solution) on the resulting jets.
4. To investigate the possibility of controlling the jet orientation.
5. To propose possible new applications based on our enhance knowledge on electrohydrodynamics.

1.5 Organization of Thesis

With the case study being electrospinning, chapter 2 was dedicated to reviewing this process, looking at the history, set-up, stages of fibre generation, the dielectric behaviour of polymers and the relationship between electrospinning and Electrohydrodynamics. Chapter 3 is a review of the different jetting modes that can occur in an EHD flow, while the fourth chapter reviews some previous EHD modelling cases that gave this work a base understanding. In the fifth chapter, the governing equations and mathematical formulations were explained. The setup of the model used, the initial conditions and the boundary conditions were detailed in chapter 6.

The results of the cone-jet formation were presented in chapter 7 and that of the dripping mode were presented in chapter 8. Extracts of these chapters were published in a special issue of Langmuir journal (March 2019). Chapter 9 was dedicated to reporting results from the effects of operating parameters on the EHD flow, while Chapters 10 and 11 reports the influences of fluid viscosity and solution conductivity and permittivity respectively. This research was concluded in chapter 12, highlighting main findings and proposed future researches to be carried out.

2. LITERATURE REVIEW

2.1 Nanofiber processing techniques

Nanofibers can be fabricated by different techniques, including solvent casting, particulate leaching, phase separation, gas forming, self-assembly, template synthesis, drawing, freeze-drying, rapid prototyping/solid freeform fabrication and electrospinning. Of all the techniques available, electrospinning is the most favourable as the equipment and setup are relatively simple; the procedure is also relatively cheap and versatile. [14].

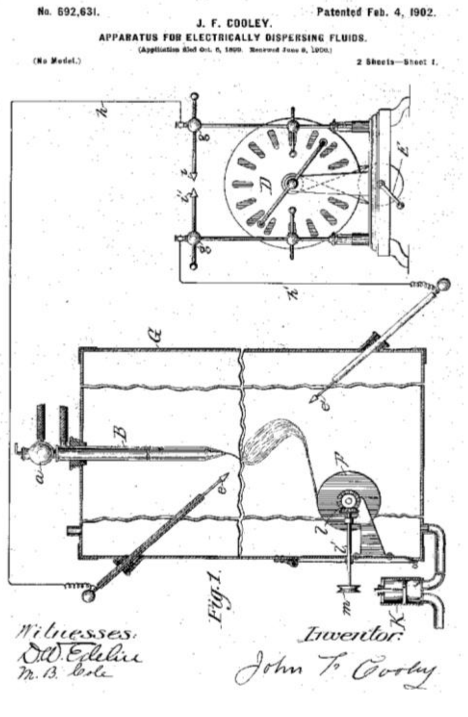

Figure 2.1- Electrically dispersing fluid apparatus from patented work of Cooley, 1902 [15]

2.2 Concept of Electrospinning

Electrospinning also known as electrostatic spinning [16] has its first reported patent dated back to 1902 by John F. Cooley [15]. Figure 2.1 shows Cooley's equipment as patented, detailing the connection of the electrodes (to develop the electrostatic field) and other important components of his apparatus.

Between 1934-1944, Formhlas published some patents on the experimental procedure and set up for fabrication of polymeric fibres with the aid of electrostatic force [17]. His spinning process was made up of a movable thread-collecting device to collect the fibres in a stretched condition like that of a conventional spinning drum in recent years. The first spinning procedure that he adopted had a drawback in that the fibres after spinning were wet, due to the short distance between the spinning tip and the collection zone. This was later overcome by increasing the distance [18].

In addition to these, some of the other worthy preliminary works on electrospinning include a study by Taylor in the 1960s, where he looked into the jet formation/initiation process [19]. Around 1987, Hayati *et al*. investigated the influence of electric field, processing environment, and other factors that affect the fibre atomization and formation of stable jets [20]. Larrondo and Manley [21] in their own work, described the technique of melt electrospinning which is very useful for polymers that don't dissolve in common solvents. A very significant experimental procedure that gave better perception into the electrospinning process was presented by Warner *et al* [22]*,* where the process equipment was designed and fabricated, the electrohydrodynamics of the process, characterization/evaluation of both the fluid instabilities and fibre morphology were done and they also developed a technique for generating oriented fibres. A more detailed historical development of the electrospinning process was presented by Nick et al [23]

2.2.1 Process

“Theoretically, the process is influenced by electrical forces on the free positive charges at either the peripheral or inside the polymer solution” [24]. Inbetween the polymeric solution and the collector, a high electric field is generated. The solution is forced along the syringe/capillary tube by either a pump or gravity (depending on the arrangement). The polymeric solution- in the form of pendant droplets, is initially held at the capillary tube/syringe tip through the mechanism of surface tension. Once the charge is induced, a mutual charge repulsion is generated and this exerts a force that is opposite to the surface tension.

Increase in this field intensity stretches the hemispherical shape of the surface into a conical shape, called the Taylor cone. At a certain critical value in which the surface tension force in the solution is overcome by the electric force, there is a discharge of the jet off the cone tip. Where the voltage is not high enough the jet might break up into tiny droplets; whereas if high enough a stable jet formation is observed at the tip. As the jet flows towards the collector, the diameter is reduced due to the stretching of the solution and solvent evaporation, hence leaving a dry fibre on the collector. The polymer chain strength disallows the breakage of the jet hence resulting in fibre formation [25]–[27]. Summarily, the whole process can be described diagrammatically as given in Figure 2.2.

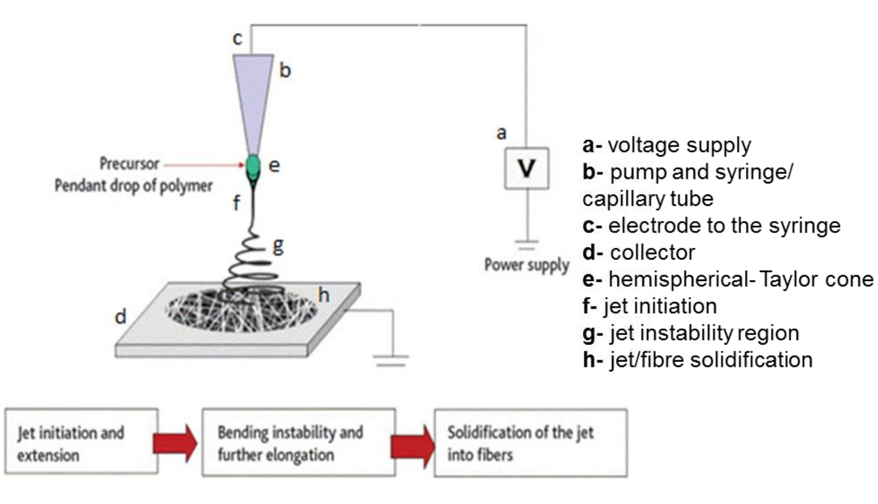

Figure 2.2- Schematic diagram illustrating the electrospinning Principle, adapted from [28]

2.2.2 Set-up

The apparatus consists of three distinct components including high voltage supply, a conductive collecting plate/screen/drum, and a metallic capillary pipe, usually with either a pipette or a small needle called the spinneret [17]. The high voltage source is usually in the range of 1-30kV [29]. The positive end of the electrode of the voltage source is attached to the tip of the spinneret while the other end is either grounded or connected to the collector.The capillary tube is filled with either a melt solution or a polymer blend and the solution is driven along with either the mechanism of gravity or the advancement of a pump [30]. The collector can be grounded [29] or charged with the negative electrode of the voltage source. Some of the various setups used in the electrospinning process are presented in Figure 2.3 (a-d).

2.2.3 Processing Parameters

Several parameters are interwoven to affect the result of the electrospun fibres. These are the solution parameters, which include the polymer concentration, surface tension, viscosity, conductivity, and molecular weight; process parameters/controlled variables like flow rate (aka “hydrostatic pressure” in the capillary), applied voltage

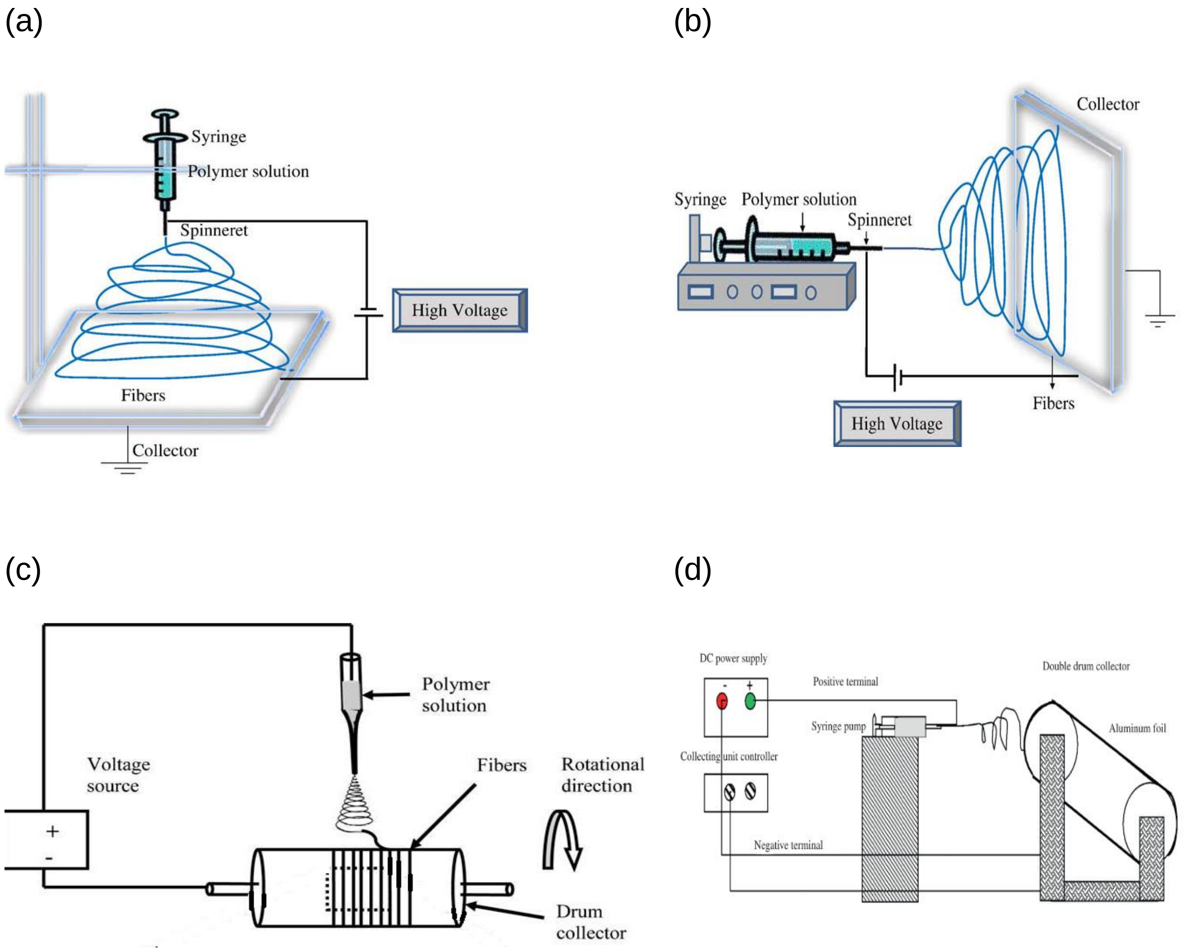

Figure 2.3-(a) Vertical Setup- Flat Collector [31], (b) Horizontal Setup-Flat Collector [31], (c) Vertical Setup-Rotating Collector [16]; (d) Vertical Setup-Rotating Collector [32]. The set up (B) is what has been adopted for this research work.

at the ‘tip-to-collector screen’ and distance. Another important set of parameters are ambient factors which include temperature, atmospheric humidity and velocity of the air in the spinning chamber or the atmosphere [31], [33]. Other important parameters are the mode of collection of the fibre, either a plain screen or a rotating drum. These parameters have different influences on the morphology, porosity or thickness of the fibres produced. Some of these have been summarized in Table 2.1 and will be explained in the later part of this chapter.

Table 2.1- Summary of Effects of Parameters on Fibres

S/N	PARAMETER	EFFECTS	REF
1	Polymer Concentration	- At low concentration, the solution only sprays into droplets as against fibres.	[34]
		- At extremely high concentrations, electrospinning is suppressed.	[34]
		- Fibre diameters increases with concentration.	[35], [36]
2	Surface Tension	- At lower magnitude, the electrospinning process occurs at lower electric field strength.	[37]
3	Viscosity	- The fibre diameter increases with the viscosity of the solution.	[37]
		- With increasing viscosity, there is a possibility of beads-on-string morphology.	[38]
4	Solution Conductivity	- Beadless fibres are achieved at higher conductivities.	[39]
5	Molecular Weight	- The fibre diameter increases with the molecular weight.	[40]
6	Flow rate	- Affects the solution transfer rate and jet velocity.	[18]
		- Affects the fibre shape and size	[41]
7	Voltage	- Increase in the voltage changes the shape of jet and decreases jet stability.	[35]
		- Fibre diameter can either increase, decrease or remain unchanged with voltage.	[24], [42], [43]
8	Tip-to-collector distance	- This affects the fibre orientation and morphology due to the variation in deposition time, whipping interval and rate of evaporation.	[18]
		- More aqueous solution requires longer distances than volatile ones to facilitate drying.	[44]

2.3 Stages of fibre formation in electrospinning- Physics of Electrospinning

The surface tension, inertia, gravity, electrostatic forces and viscosity are the major parameters that contribute to the elongation of jet during electrospinning [45]. The major stages involved in the process of fibre formation are: droplet formation, the jet initiation stage, bending instability stage (either with or without branching/splitting of the jet) and the fibre solidification stage; in that order. Understanding the physical processes will go a long way to provide the information needed for the modelling.

2.3.1 Droplet Formation

This process is initiated by the pumping of the polymeric solution at a low rate into the capillary tube. In the absence of electric charges, the solution form into droplets at the tip of the capillary and invariably fall, eventually, under the force of gravity.

Given fluid density, ρ acted upon by gravitational force of F_g and surface tension, γ, the radius, r_0 of the meniscus formed at the capillary tip (with an internal radius, R_{cp}) is given as [46]:

$$r_0 = \left(3R_{cp}\gamma/2\rho g\right)^{1/3} \quad \text{……………………………………….(1)}$$

The solution will continue to 'drip' until the applied voltage on the conductive fluid is high enough to generate a finite electric force of F_e, therefore constituting a balance of capillary forces,

$$F_\gamma = F_e + F_g \quad \text{……………………………………………….(2)}$$

At this instant, the droplet size at the tip of the capillary is reduced to r $(r < r_0)$.

The electric force, F_e can be expressed as [47]:

$$F_e = \left(4\pi\varepsilon V^2 \Big/ \ln\left(\frac{4d}{R_{cp}}\right)^2 \right) \text{……………………………………(3)}$$

Given that d is the distance between the capillary tip and the grounded collector surface, V is the positive applied voltage and ε is the permittivity of the medium.

Also, the droplet radius after the application of electric force is expressed as [47]

$$r = \left\{ (3/2\rho g) \left(R\gamma - \left(2\varepsilon V^2\right) \Big/ \ln\left(\frac{4d}{R_{cp}}\right) \right) \right\}^{1/3} \text{……………………..(4)}$$

Equation (4) can be used to determine the droplet size as a function of the applied voltage. As the applied voltage increases, the value of r becomes smaller until the bending instability begins and the value of the applied voltage $V = V_c$ [46].

2.3.2 Taylor Cone formation

The Taylor cone formation is inarguably the most important stage of the whole process. Figure 2.4 shows the schematic of this formation [16]. The Coulombic force induced by the electric field and the Electrostatic repulsive force due to the surface charges are the two main electrostatic forces that the polymer drop experiences [48]. suppressing the application of the high voltage to the spinneret, the tip of the polymer droplet is held by its own surface tension [49].

(A) Hemispherical shape due to the presence of electric field, electric charges are generated at the tip of the droplet. At this stage, the Coulombic force is predominant.

(B) Droplet becomes elongated, transforming from the hemispherical shape into a conical shape, during which the charge tries to oppose the surface tension of the droplet.

(C) Final deformation of the droplet tip to form the Taylor cone due to same-charge repulsion. The Taylor cone is formed when the surface tension balances the electric field. The angle of the cone was found to be 49.3 degrees [19].

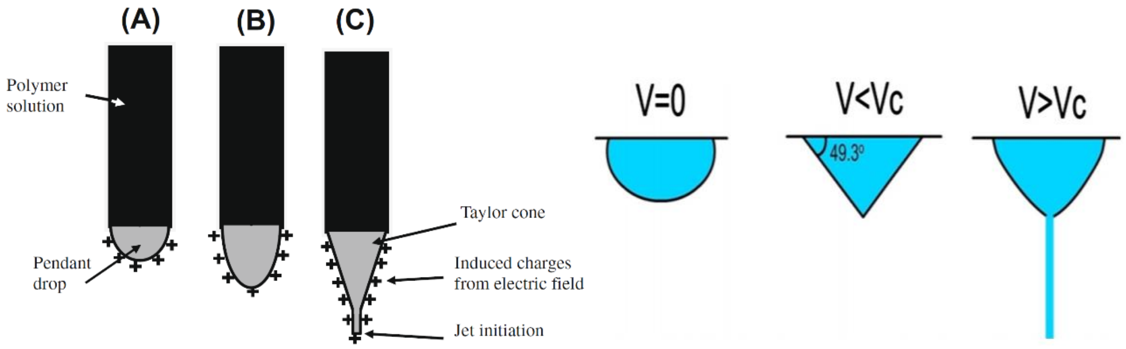

Figure 2.4- Jet Initiation showing the Taylor cone formation angle [13], [37]

As the electric field attains a critical value, the electrostatic forces finally overcome the surface tension in the polymeric solution and this commences the ejection of the polymer jet from the tip of the Taylor cone [49].

The critical value of the electric field needed for jet initiation (at which value the electrostatic forces overcome the surface tension of the polymeric solution from the tip of the cone) is given by Taylor [19] as:

$$V_c^2 = 4\left(\frac{H^2}{L_{cp}{}^2}\right)\left(\mathrm{In}\frac{2L_{cp}}{R_{cp}} - 1.5\right)\left(0.117\pi R_{cp}\gamma\right) \ldots\ldots\ldots\ldots\ldots\ldots\ldots\ldots\ldots\ldots\ldots (5)$$

Where, V_c is the critical value of the electric field needed for jet initiation (kV), H is the air gap distance (cm), L_{cp} is the length of the capillary tube (cm), R_{cp} is the radius of the tube (cm) and γ is the surface tension of the fluid (dyn/cm).

2.3.3 Bending Instability

An essential mechanism in electrospinning is the instability of the jet. The electrified jet continues on an approximately straight path for a short distance, after which it is then bent into complex paths and consequently other changes in shape occur [50]. These changes are driven by the electric field and the aerodynamic nature of the surrounding space [51]. Three forms of instabilities are experienced in the path of the electrified jets: Rayleigh (axisymmetric instability), electric field-induced axisymmetric instability and electric field-induced whipping instability [52]. As quoted by Hohman et al [52], [53] “The dominant instability strongly depends on the fluid parameters of the jet (viscosity, dielectric constant, conductivity) and also the static charge density on the jet. In particular, for a high conductivity fluid, when there is no static charge density on the jet, the varicose mode (where the jet remains in the axisymmetric but the jet diameter is modulated) dominates the whipping mode. When there is a large static charge density, the whipping mode tends to dominate; the reason for this is that a high surface charge simultaneously suppresses the axisymmetric Rayleigh mode and enhances the whipping mode.”

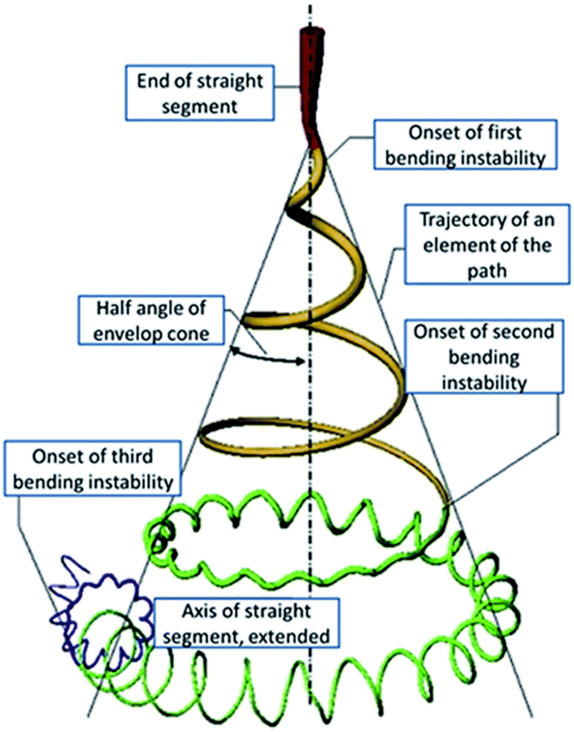

Figure 2.5- Onset and development of bending instabilities [8]

2.3.4 Solidification of fibre

The final stage of the process is the solidification stage; as the (whipping) fibre travel towards the collector/target, the solvent is lost via evaporation and this leaves only the well entangled, continuous and stretched chain of the fibre. The fibre is then collected as tiny strands in the micro/nano range.

2.4 Electrospinning vs Electrohydrodynamics (EHD)

Electrospinning is an extremely complex process that involves high-speed nonlinear EHD, transport of electric charges in a field, complex rheology, mass transport and finally heat transport within the electrified polymer jets [49]. Zhakin [4] highlighted that EHD is an interdisciplinary field that encompasses hydrodynamics, thermophysics, electrochemistry and electrostatics (electrokinetics- deals with the behaviour of charged particles in fluids). EHD focuses on weakly-conducting fluids i.e. leaky dielectrics having low electrical conductivity in the range of $10^{-7} - 10^{-12} \Omega^{-1} cm^{-1}$.

Since in electrospinning the fluids are poorly conducting, this makes EHD the ideal approach to detail the process. In EHD, the fluid dynamics and the electric field distributions are coupled; this electromechanical coupling is at the core of the observed behaviour. The coupling of the two fields is bi-directional. There is additional stress on the momentum equation due to the applied field and the movement of the polarized particles and the evolving fluid patterns also alter the distribution of the permittivity $(\varepsilon)$and the free charge(q) in space [54]. Melcher and

Taylor and Melcher [55], noted that EHD is a field of fluid mechanics that studies the effects of electric forces and also the influence of the media on electric fields [55]. It is also to be noted that this coupling only takes place at the interface of two fluids.

The charges are transported and reside at the interfaces which introduce electrical stresses of a unique type [56].

2.5 Dielectric behaviour of polymer

Based on the responses to the electric field, polymeric fluids can be categorized as:

1. Perfect dielectric- Also called perfect insulators, they do not have any free charges and hence their conductivity is zero.
2. Perfect conductors- They have charges which are free to move. The electric field and charge density are zero in the bulk. With or without an electric field, the charges align themselves to the surface to perfectly cancel out the field-effect, hence all the charges are located at the surfaces of the media.
3. Poor conducting- Leaky dielectric- They allow electric charge to accumulate at the drop interface, hereby permitting tangential electric stress to be generated, this stress drags the fluid in motion which by implication generates hydrodynamic stresses at the liquid drop interface [20]. In leaky dielectrics, free charges accumulate on the interface of the fluids and hereby modify the field, particularly producing shear stress.

Dielectrics are substances with no free charges; all the electrons are associate and bounded together with the nearest atoms. Dielectric constant represents the permittivity (ε) of a medium. The permittivity expresses the capacity of the medium to polarise under the influence of an electric field. More precisely, the dielectric constant relates the ratio of the permittivity of dielectric medium to that of vacuum. By implication, the dielectric constant is proportional to the degree of the resultant polarization in a media under an applied electric field. The interplay of the mechanism of the electric field and polarization contribute to the dielectric property of the polymer.

Physically, polarization occurs when the polymer is under the influence of an electric field. Until the application of electric field, electrons are evenly distributed. Upon application, the cloud of electrons is displaced in the opposite direction of the applied field. The resultant effect of this is the separation of the positive and negative charges, making the molecules act like electric dipoles [57]. There are four modes of polarization that take place in dielectrics and it is a combination of these four that contributes to the overall polarization of the medium:

a. Orientational polarization- dipolar or molecular polarization. This aligns the disoriented/randomized ions in the direction of the applied field.
b. Atomic polarization- ionic polarization.
c. Electronic polarization- In the absence of an electric field, the nucleus of an atom appears spheroid, but this becomes deformed when a field is applied. The positive and negative ions separate, with the positive ions migrating in the direction of the applied field.
d. Space-charge polarization/Interfacial Polarization- In the absence of electric field, the positive and negative charges are not separated but under the influence of a field, the positive charges migrate in the direction of the field and are pushed to the interface of the body.

Generally, inorganic/ceramics have higher dielectric constants than polymers because they contain ions and polar groups in them which enhance their permittivity. It is worthy to mention the nature of water, even though with high dielectric constant, it fluctuates because of impurities. Also, air, which is the reference medium has a value of 1.02 [58].

Table 2.2- Dielectric Constant of Certain Materials/Media [58]

Material	**Dielectric constant, ε**	**Material**	**Dielectric constant, ε**
TiO_2	100	Fluorinated polyimide	2.5-2.9
H_2O	78	Methylsilsesquioxane	2.6-2.5
Neoprene	9.8	Polyarelene ether	2.8-2.9
PVDF	6.0	Polyethylene	2.3-2.7
SiO_2	3.9-4.5	Polystyrene	2.5-2.9
Fluorosilicate Glass	3.2-4.0	Teflon AF	2.1
Polyimide	2.8-3.2	Air	1.02

2.6 Electrospinning parameters

A couple of parameters are interwoven to affect the result of the electrospun fibres. These are the solution properties, which includes the polymer concentration, surface tension, viscosity, conductivity, and molecular weight; process parameters/controlled variables like flow rate (aka “hydrostatic pressure” in the capillary), applied voltage at and ‘tip-to-collector screen’ distance, another important set of parameters are ambient factors which include temperature, atmospheric humidity and velocity of the air in the spinning chamber or the atmosphere [31], [33]. Other important parameters are the mode of collection of the fibre, either a plain screen or a rotating drum. These parameters have different influences on the morphology, porosity or the thickness of the fibre produced.

2.6.1 Polymer Solution Parameters

Several studies have been conducted to check the influence of the solution parameters on the fibre formed from a polymeric solution. This section will take a brief review of the correlation between the parameters and the resulting generated fibres.

2.6.1.1 Polymer concentration

In the preparation of polymers, the appropriate concentration is important. When the concentration is too low, droplets (electrosprays) are formed instead of fibres, while at very high concentrations, electrospinning is totally suppressed; therefore an adequate range of polymer concentration is required for electrospinning to occur [34]. In their work, Deitzel et al [35] discovered that the concentration has a strong effect on fibre size, noting that the fibre diameter increases with the concentration. Similarly, Yang et al [36] investigated PVP in a solvent of ethanol/DMF (50/50w/w) and observed that the same trend, see Figure 2.6.

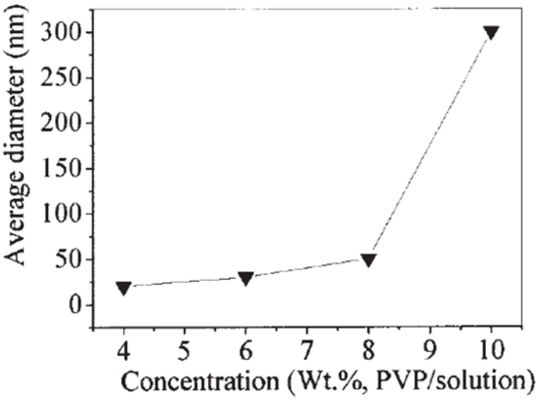

Figure 2.6- Effect of Polymer Concentration on Fibre Diameter [36]

Finally, Li and Wang [59] in a report noted that there are four levels of concentrations ranging from low to high as seen in Figure 2.7:

a) Very low Concentration: at this level, the polymer solution tends to electrospray as against electrospinning, this is due to the low viscosity and surface tension. Also, a morphology with micro/nanoparticle is generated

b) At a little higher concentration; there is a mixture of beads and fibres strings.

c) At a suitable polymer concentration, smoother fibres are developed.

d) Finally, when the concentration is on the high side, a non-nanoscale fibre, having a helix-shaped micro-ribbon is obtained [59].

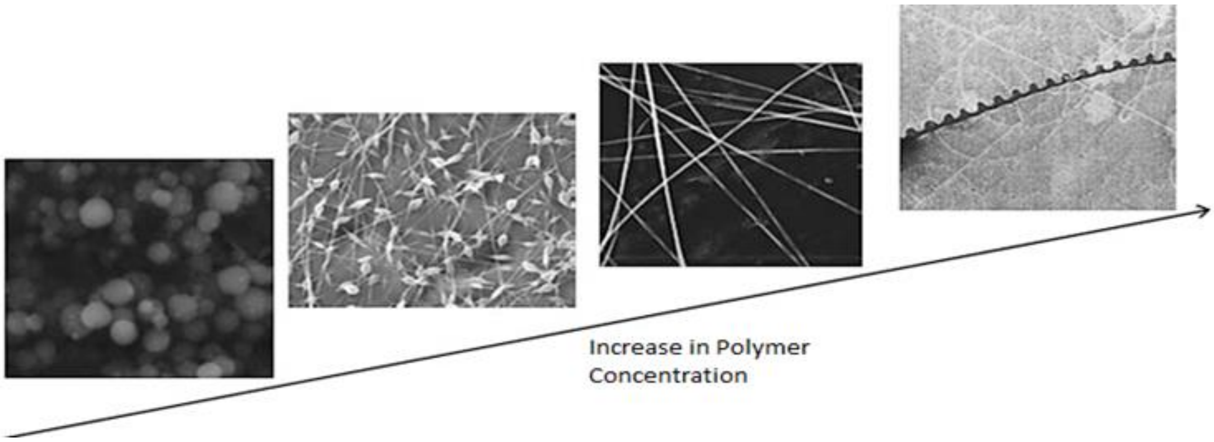

Figure 2.7- Effect of Polymer Concentration on Fiber morphology [59]

2.6.1.2 Solvent Composition

Nitanan et al [60] checked the effect of solvent composition by varying the composition of DMF and THF on polystyrene polymer. It affected the viscosity, conductivity, surface tension and consequently the morphology of the generated fibre. Hence the effect of the solvent composition can be determined by checking the solution properties like conductivity and surface tension. Figure 2.8 is an example of how the fibre diameter is affected by this parameter.

2.6.1.3 Surface Tension

This has been reported to be a function of the solvent composition [59] and negligibly on the polymeric solution [61]. When the surface tension is reduced, beadled fibres are likely to be formed [31]. The development from droplets to bead to fibres is subject to the surface tension of the polymeric solution, when lower it initiates a spinning process that occurs at a reduced electric field [61].

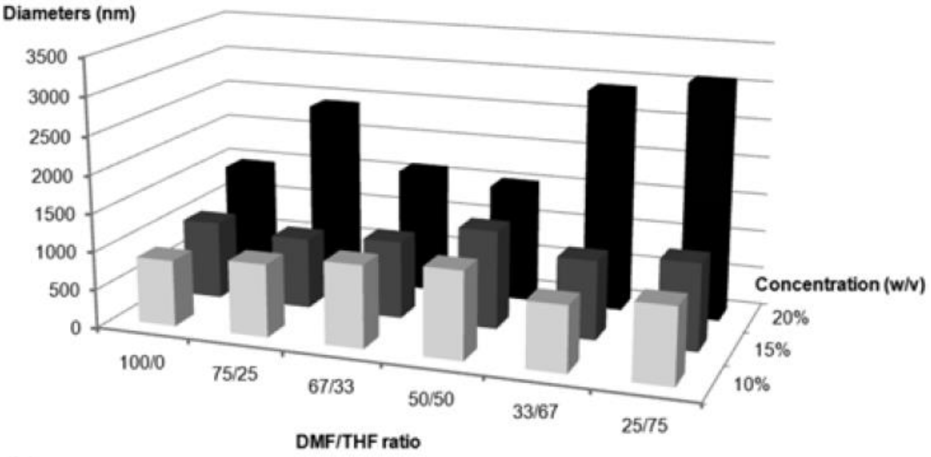

Figure 2.8- Effect of Solvent Composition on Fibre Diameter [60]

2.6.1.4 Viscosity

It is reported that the fibre thickness increases with the solution viscosity, also there is a very high probability of generating fibres with beads when the viscosity is low [61]. Invariably the bead develops larger and the inter-bead distance increases as the solution becomes more viscous, i.e. the bead shape changes from a sphere to a spindle-like shape [38], see Figure 2.9.

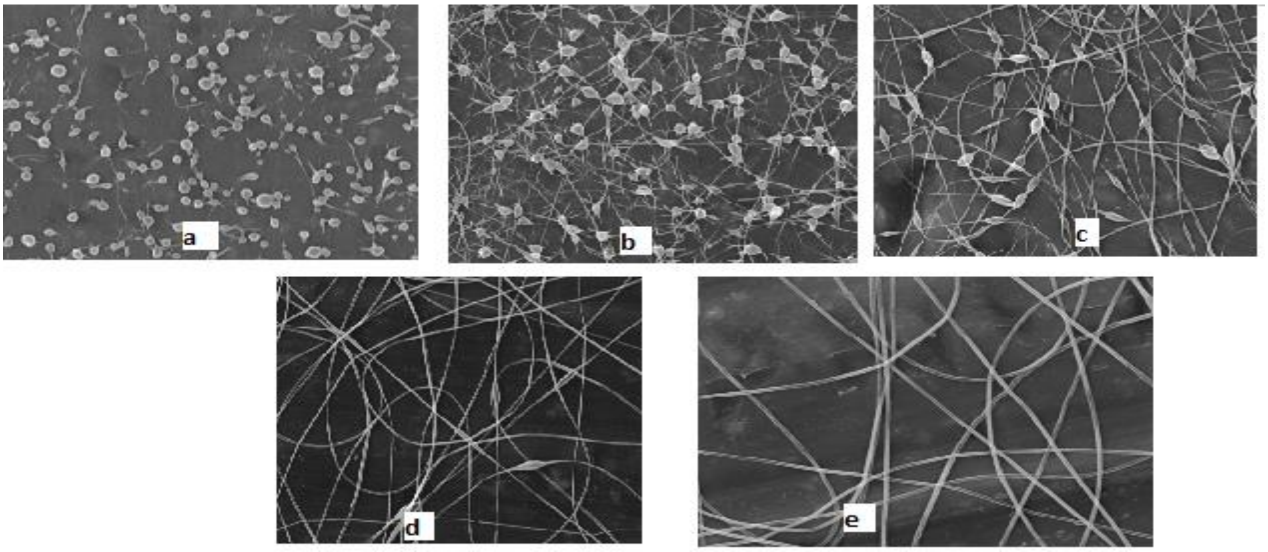

Figure 2.9- Effect of Viscosity on Fibre Morphology and bead development. (a) viscosity= 13 centipoise, (b) 32 centipoise, (c)160 centipoise, (d) 527 centipoise and (e) 1835 centipoise. The beads deform from a spherical shape into spindle-like shape as the viscosity increases [38].

2.6.1.5 Solution Conductivity

This is mainly a function of the polymer type and the solvent used [59]. In experiments while electrospinning PS, Uyar and Besenbacher [39] used different grades of DMF and some other solvents like $CHCL_3$, THF etc. to prepare the polymeric solution, the solution resulted in different conductivity parameters and it was observed that at higher conductivity beadless fibres were developed.

2.6.1.6 Molecular Weight

The viscosity and surface tension of a polymer increase with molecular weight which leads to a more densely packed entangled polymer chain, these effects play a vital role in defining the surface morphology and diameter of fabricated scaffold [62]. Koski et al. [40], while investigating the influence of molecular weight on fibrous PVA; PVA with molecular weight ranging from 9,000-186,000g/mol were electrospun under same parameters, it was noted that fibre diameter increased with molecular weight. Also, at low molecular weigh the fibres gave a circular cross-section and the flat fibres were recorded at higher molecular weight. Likewise, increase in the molecular weight lead to an increase in the size of fibre and lesser uniformly shaped pores on the fibres [63].

2.6.1.7 Solvent Volatility

It is worthy of note that electrospinning process involves both the phase separation and the rapid vaporization of the solvent (this, as well as the drying time of the solvent are dependent on the vapour pressure of the solvent used). The solvent volatility affects the development of nanostructures by manipulating the phase separation stage [18]. Megelski et al [64] also observed that a combination of micro and nanofibre morphologies were generated with solvents with higher volatility, while microstructures were mainly observed at lower volatility. Also, they reported that decrease in volatility results in a smoother microtexture.

2.6.2 Operating Process Parameters

Like the solution parameters, the processing parameters play a significant part in the formation of fibre and its arrangement. Sill and von Recum [41] stated (in the order of impact), the process parameters to include the applied voltage, flow/feed rate and the capillary tip-to-collector screen distance.

2.6.2.1 Flow Rate

Generally, the flow rate affects both the jet velocity and the solution transfer rate [18]. It was reported that the polymer flow rate influences the size, porosity and the shape of the fibre generated [41]. In a work by Megelski et al [64], it was concluded that the pore sizes increases with flow rate.

2.6.2.2 Voltage

Deitzel et al, [35] argued that there was a strong correlation between the voltage and the formation of bead defects in the fibres. They noted that increasing the applied voltage changes the shape of the jet initiation as a consequence of a decrease in the stability of the jet, this has been connected with a rise in the number of beads formed on the electrospun fibre. Largely, fibre bead density increased with jet instability, this can be observed from Figure 2.10.

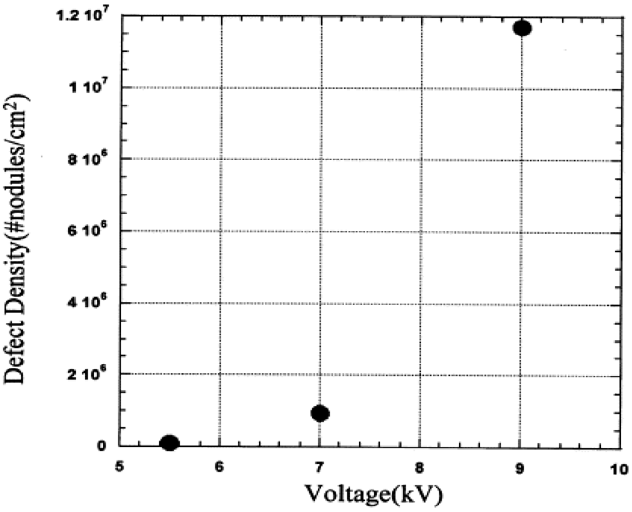

Figure 2.10- The Effect of Voltage on the Development of Beads on Electrospun Fibres [35]

There are variations of opinion on the effect of the voltage on the fibre, specifically on the surface morphology and fibre diameter. Zhang et al [42], in their own view noted that the fibre diameter increases with voltage due to more amount of polymer being ejected, Larrondo and Manley [21] reported a decrease in fibre diameter by almost half due to a doubling the applied voltage, while Reneker and Chun [65] argued that there is no significant influence of the voltage on the diameter.

2.6.2.3 Capillary Tip-to-Collector Screen Distance

“The fibre arrangement and surface morphology are majorly affected by the capillary tip-to-collector distance due to their reliance on the rate of evaporation, deposition time, and the whipping/instability interval” [18]. Notwithstanding the polymer concentration, short deposition distances results into wet fibres and/or beads hitting the surface of the collector [44] as the polymeric solvent does not have enough time to evaporate and dry off before collection and the phase separation is incomplete. Also, Buchko et al [44] noted that more aqueous solutions will require more distances than the volatile ones to enhance drying of the fibre.

2.6.3 Ambient Process Parameters

2.6.3.1 Atmospheric Humidity

At a humidity greater than 30%, electrospun fibres begin to show surface features“Controlling surface morphology of electrospun polystyrene fibers: Effect of humidity and molecular weight in the electrospinning process,”/pores. Humidity has been found to affect the surface morphology of the spun fibres. When the humidity is increased, the diameter and shape of the pores are increased, also the distribution of the pores is increased [63], as shown in Figure 2.11.

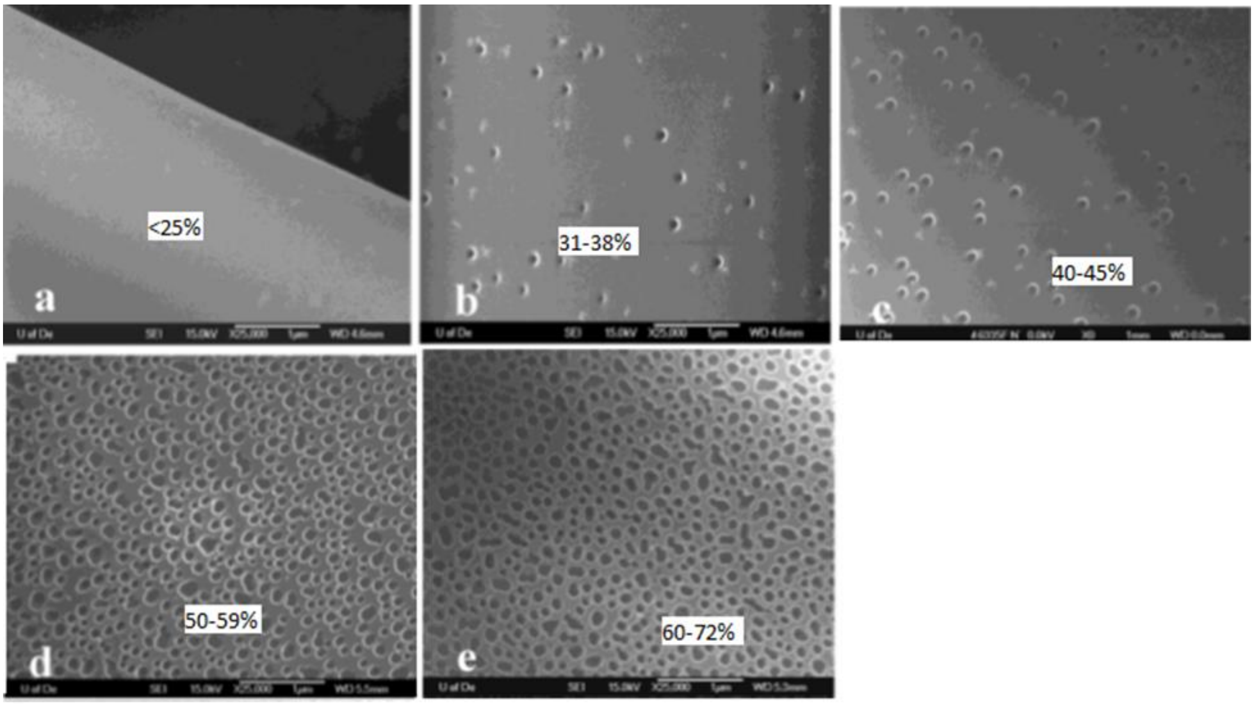

Figure 2.11- Effect of Humidity on Morphology, showing increased density of pores on the fibre and non-uniformity of the pores as the humidity increases. [63]

2.6.3.2 Temperature

When the temperature of the polymeric solution is increased, the conductivity, surface tension and the viscosity of the solution are decreased, this invariably leads to thinner fibre and the fibres have a higher deposition rate on the collector [66]. While electrospinning PA-6, Mit-uppatham et al [66] also noted that at various temperatures, the morphologies were found to be similar save for the average fibre diameter. Explaining the molecular transformation in the polymer, they noted that as the temperature is elevated, the polymer molecules are expanded, and this leads to a drop in the chain entanglements hence a decrease in viscosity of the solution. This decrease implies that the viscoelastic force that is meant to oppose the Coulombic force at stretching is reduced, hence a general reduction in fibre diameter is observed [66].

3. CLASSIFICATIONS OF EHD MODES

There are various classifications of the EHD modes by different researchers including [67]–[72]. Jaworek and Krupa [73] summarised these modes as shown in Table 3.1. This categorization is based on the **form of the meniscus at the capillary tip** and **the developed jet** as it travels in the direction of the applied field. It is worthy of note that jet deformation varies based on the applied external or internal force (either electrical, fluid surface tension or mechanical forces). These modes are also affected by the solution parameters and the operating parameters of the EHD process. This chapter will take a brief review into each of these modes.

Table 3.1- Classifications of EHD Modes. Adapted from [73]

EHD Classification Based on Shape of Meniscus		**EHD Classification Based on the Developed liquid Jet**	
Dripping Mode	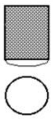	Cone-jet mode	
Microdripping Mode		Oscillating-jet mode	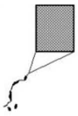
Spindle mode	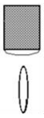	Precession mode	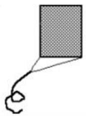
Multispindle mode	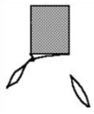	Multijet mode	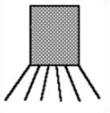
Ramified-meniscus mode	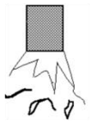	Ramified-jet mode	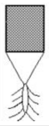

3.1 Electrohydrodynamic Modes based on the Geometrical form of the Liquid at the Capillary Tip.

As shown in Table 3.1, the first category includes the dripping, microdripping, spindle, multispindle and ramified-meniscus modes, depending on the meniscus profile at the tip of the nozzle, as the droplet is formed.

3.1.1 The dripping mode

There is a formation of droplet at the tip of the capillary even in the absence of electric field; under the influence of gravitational force, the droplet detaches from the mainstream. When electric force is exerted, there is an increase in the frequency of droplet emission and there is a decrease in size [68]. The drops are formed as regular spheres detaching from the capillary as the droplet weight and the electric field forces overcome is surface tension and other capillary forces of the fluid [70]. As the field gets stronger, the meniscus elongates resulting in smaller droplets dripping from the mainstream. After the detachment, the meniscus contracts into the capillary assuming a hemispherical shape.

3.1.2 The microdripping mode

In this mode, fluid at the capillary tip forms a stable hemispherical pendant, at the end of which a droplet with diameter smaller than the capillary emerges. The droplet detaches and does not undergo any further disintegration. The mode only occurs at a combination of low flow rates and relatively low voltage. The difference between this mode and the dripping mode is that there is no meniscus contraction after droplet detachment [73]. The droplet size is in the $1\mu m - 100\mu m$ range.

3.1.3 Spindle mode

The shape of the emerging jet is spindle-like hence the name of the mode [74]. “In this mode, the meniscus of liquid elongates in the direction of electric field as a thick jet and detaches as a vast spindle-like fragment of liquid” [70]. At the post detachment stage, this spindle occasionally disrupts into droplets with smaller and varying sizes which disband from the capillary axis.

3.1.4 The multi-spindle mode

In their work, Jaworek and Krupa [70] observed this mode in EHD flows having solutions with higher viscosities. It has similar features with the spindle mode, except that the spindles are emitted intermittently from at the circumference of the capillary and they jet out in the form of short spindles. After this jetting, they disintegrate into smaller droplets. With increase in applied voltage, the number of jetting points increases. The generated droplets are smaller than spindles developed in the spindle mode, as shown in Table 3.1.

3.1.5 The ramified-meniscus mode

The liquid meniscus is ejected in the form of irregular short jets from the capillary tip and the orientation is in random directions. The disintegrated drops develop into irregular fragments of liquids, in terms of sizes and direction [70].

3.2 EHD Modes based on jet behaviour as it disintegrates into droplets

The second grouping includes the cone-jet, oscillating-jet, precession, multi-jet and ramified-jet modes, depending on the jet behaviour as it disintegrates into droplets.

3.2.1 The cone-jet mode

In this mode the liquid discharges from the capillary tip in form of a regular, axisymmetric cone with an emerging thin jet at the cone tip. This jet is in the $<100\mu m$

range of diameter. The underlying cone shape can either be concave, convex or linear in shape; while the jet undergoes two types of instabilities- kink/whipping or varicose [70]. Hohman et al [53] described the varicose mode as one where the jet remains in the axisymmetric but the jet diameter is modulated, while the kink mode has the axis of the jet move irregularly and breaks off into droplets under the influence of EHD forces. It is worthy of note to state that Taylor [75] demonstrated that at any point of the liquid cone, the electrostatic and capillary pressures can be balanced.

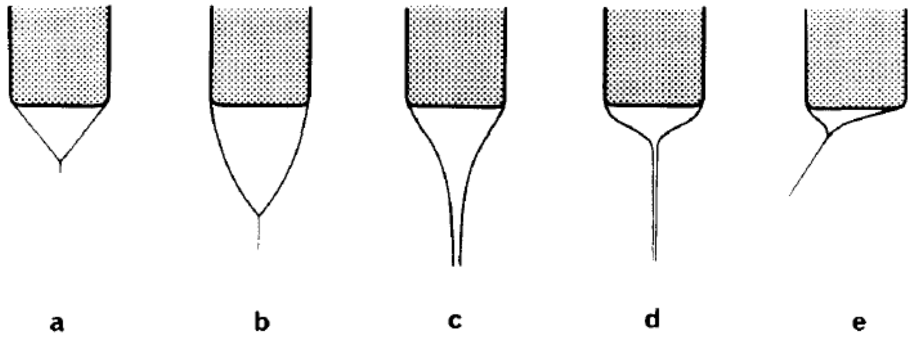

Figure 3.1- Different forms of meniscus in cone-jet mode. (a)The cone-jet moving along a straight path as the shape evolves, (b) The cone-jet taking a curved shape, (c) The cone jet, showing the acceleration zone extending towards the base of the cone, this happens when the conductivity decreases, (d) As the conductivity further decreases, the jet diameter decreases and the acceleration zone further extends towards the base of the cone, (e) This is a case of asymmetrical cone-jet system due to unstable jetting. [68].

3.2.2 The precession mode

The precession mode is marked by the nature of the meniscus- as it assumes a skewed rotating cone at the tip of the capillary, from which a rotating jet emerges in a spiral manner [71]. Cloupeau and Prunet-Foch [74] also observed a similar trend by highlighting instances where “the jet bends just after the outlet of the capillary, it may turn regularly around the axis, so that the emitted droplets form a spiral”

3.2.3 The oscillating-jet mode

In an oscillating-jet mode, a rotating oscillating emerging jet disintegrates into droplets of different sizes due to whipping instability [76]. This phenomenon is also observed with increasing voltage/electric field; in which the swirling of jet front and the strong lashing take place [77]. As the flow rate increases over a critical value, the cone-jet develops into an oscillating-jet mode because of the inability of the electric field to draw the liquid from the capillary or because of the high charge carried by the jet [78].

3.2.4 The multi-jet mode

Noymer and Garel [79] made a remarkable distinction of this mode from the cone-jet mode, noting that the droplet sizes are smaller in the multi-jet mode. From the findings of Jaworek and Krupa [70], this mode develops from the cone-jet mode when the magnitude of the voltage and flow rate increases. The stages of development start with an initial development of a skewed Taylor cone, this jet (which is unstable), then two or more jets develop in a symmetrical form at the rim of the capillary; afterwards, the jet meniscus becomes flat developing short cones. The jet diameter falls in the $10\mu m$ range. The higher the electric potential and flow rate, the more the emission points and faster they get thinner due to shear stresses. This mode is illustrated in Figure 3.2.

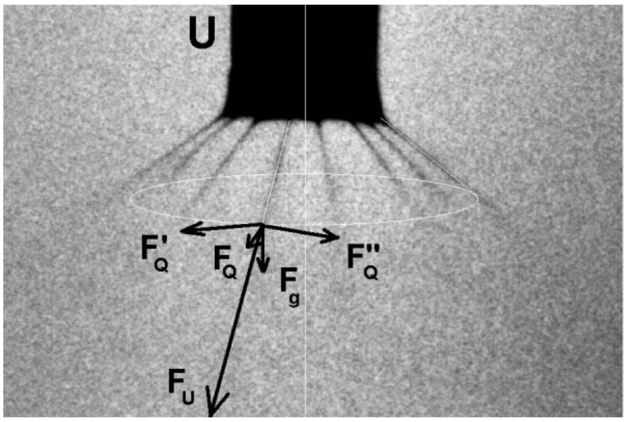

Figure 3.2- Schematic representation of the multi-jet mode [70].

3.2.5 The Ramified-jet mode

This final mode is rarely observed, according to Cloupeau and Prunet-Foch [68]. In this mode, the main jet forms strings of thickened points out of which one or more fine jets emerge. In another case, the fine jets develop shortly after the capillary or just immediate from a capillary tip. These cases are illustrated in Figure 3.3.

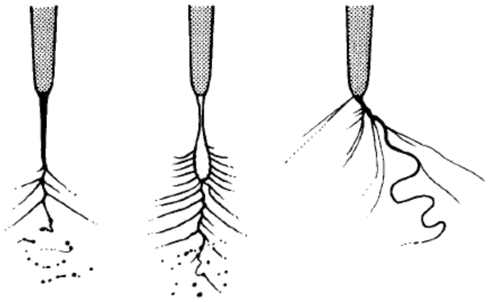

Figure 3.3 Ramified-jet mode [68].

4. REVIEW OF PREVIOUS MODELLING AND SIMULATION OF EHD

Over the years, computational modelling of EHD flows has given access to lots of information on the distribution of the liquid cone, jet and jet break-up, the liquid flow, force distribution, charge distribution and electric field. This session will review 3 important studies around EHD simulation.

4.1 EHD ATOMIZATION

The physics, theory and approaches of atomization and Taylor cone formation are discussed in this session. The works of Lastow and Balachandran [57] and Najjaran et.al. [7] provide very deep insight into this. They modelled this phenomenon with the use of ANSYS CFX 4.4 and ANSYS FLUENT 12.1 respectively, both Finite Volume, pressure correction-based solvers (similar to the approach used in this study). The solver used in by Lastow and Balanchandran does not contain a module to handle the electrostatic field equations, and the heat conduction equation/solver was ingeniously modified to address this. In the work of Najjaran et. al., the solver has both the flow and the electric module solver. In solving the equations, the electric body forces are determined from the electrostatic field equations and included in the Navier-Stokes equations.

The approach adopted was to solve the coupled Hydrodynamic and Electrostatic EHD equations simultaneously which is also adopted in this current work. They identified that the key fluid property for the coupling is the permittivity (ε). Also, a notable assumption they didn’t follow, unlike previous models (where an initial cone shape is assumed for the liquid or where an initial charge distribution was assumed), their works presume a flat initial shape for the liquid and with no charge present, the resultant shape and distributions were then developed due to effect of the applied electric field.

4.1.1 Numerical Approach

The combined Navier- Stokes equation is given as:

$$\rho \frac{\partial \vec{u}}{\partial t} = -\nabla P + \mu \nabla^2 \vec{u} + \rho g + f_e \;\ldots\ldots\ldots\ldots\ldots\ldots\ldots\ldots\ldots\ldots\ldots\ldots\ldots\ldots\ldots\ldots (6)$$

Where, f_e is given as the Coulombic force = QE.

The solution procedure is based on the pressure correction approach and more specifically the SIMPLEC (Semi-Implicit Method for Pressure Linked Equations-Consistent) algorithm, an implicit solver which provides for enhanced pressure-velocity coupling with an advantage of faster convergence than the SIMPLE (Semi-Implicit Method for Pressure Linked Equations) algorithm [80], [81].

The momentum equation was solved by a hybrid differencing scheme, which is basically a second order central differencing scheme mildly blended with a first-order upwind differencing scheme for added stability. Due to the need for high accuracy, a very fine mesh and short time step were employed in the model. The mesh size was in the order of $10^{-6} m$ and the time step was between $10^{-9} - 10^{-5} s$.

4.1.2 The Model and Boundary Condition

The models deployed in these studies were axisymmetric ones, therefore the need to increase mesh density towards the symmetry axis, as can be seen in Figure 4.1. The simulations require a very precise knowledge of the capillary and the liquid geometry and contact angles; this information which were based on assumptions

[82]. The two models only account for the axisymmetric mode of the process and not able to handle the whipping modes.

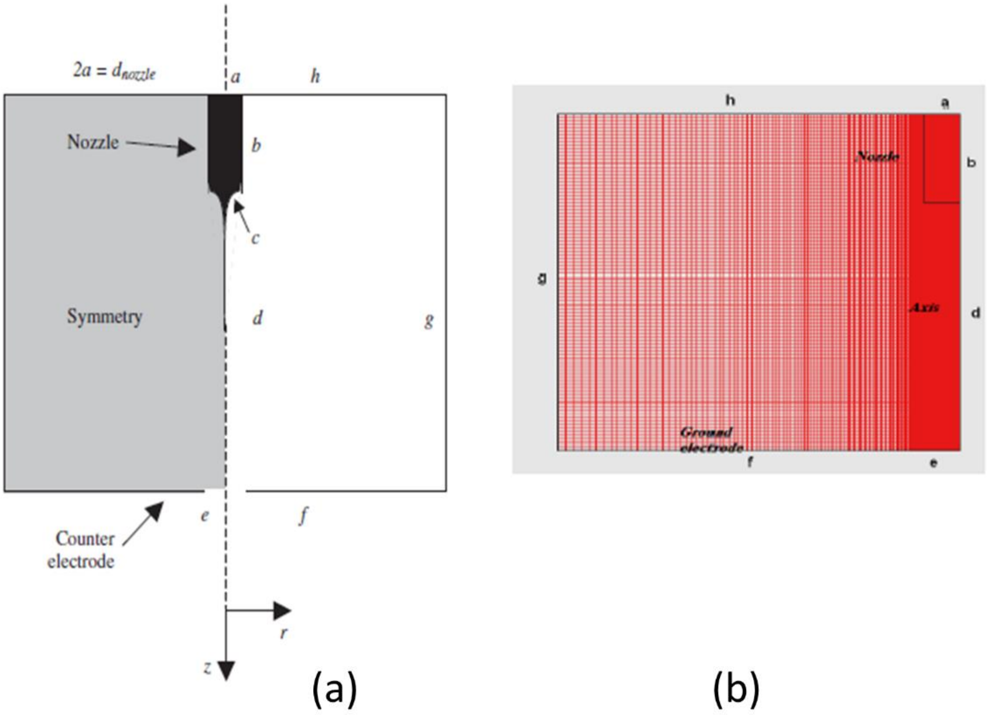

Figure 4.1- Computational Domain (a) Lastow and Balachandran [82] and (b) Najjaran [7]

To describe the model used, the capillary wall was modelled as an infinitely thin cylindrical wall (they argued that as the cone-jet is formed, the cone retracts between the capillary walls, as it can be seen in Figure 4.1. For the boundary condition, they were broadly divided into electrostatic and hydrodynamic conditions. Neumann conditions were used on the symmetry and Dirichlet conditions on the remaining boundaries

4.1.3 Results

One of the drawbacks of existing models, as described in chapter 2, is that they do not include the droplet break-up model, as such they only handle the axisymmetric region of the process. Also, the length of the jet was longer than the experimental comparison, meaning that the tensile stress obtained in the simulation differs from what obtains in the reality. Stable cone-jet modes were observed between the voltage range of 3875-4125V, below which there is not jetting and above which the atomisation becomes unstable as shown in Figure 4.2. Note that the liquids used for these simulations was heptane and ethanol

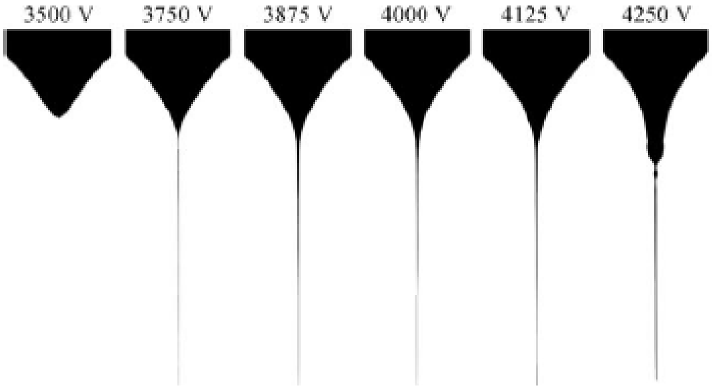

Figure 4.2- Jet formation of heptane at different applied voltage [82]

Also, the predicted droplet sizes compared well with the experimental results as seen in Figure 4.3, except for the lowest flow rate which gives a 0.5µm difference in the droplet size.

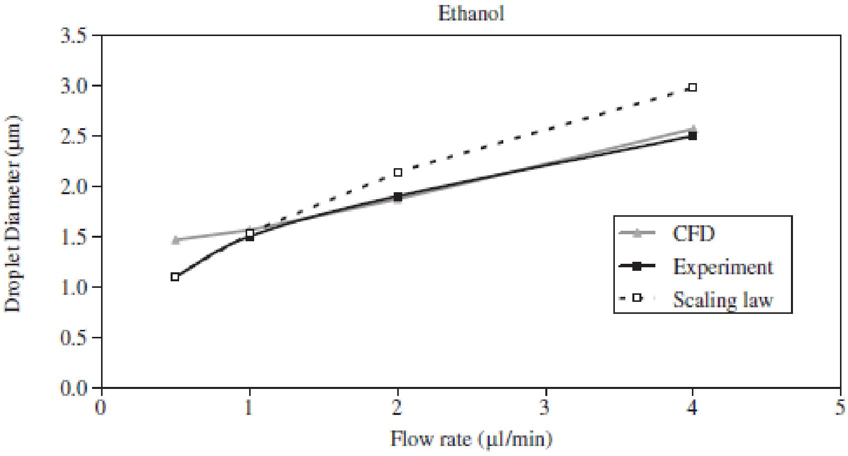

Figure 4.3- Droplet size vs Flow rate for CFD simulation of Ethanol and the Flow rate [82]

4.2 FORMATION AND DISTORTION OF TAYLOR CONES

Taylor cone is a critical stage in the process of most EHD applications and lots of studies (experimental and theoretical) have been carried out to study this process. Of a notable one is the study by Sarkar et al [83], the team studied this process the FLOW-3D code (Flow Science Inc., Santa Fe, New Mexico). The Taylor cone is the resultant conical shape of a dielectric fluid drop under the influence of an electric field. In their work, they pointed out that it is very pertinent to understand the mechanism of coupling between the electrical and hydrodynamic forces in the Taylor cone formation; the coupling which depends highly on both the electrical and hydrodynamic properties of the fluid. The flow rate, fluid properties and applied voltage are the three factors that shape and size of the Taylor cone depends on [84]. Polyethylene oxide (PEO) solution was used to for the study at various applied electric fields and flow rates.

4.2.1 Numerical Approach

The algorithms used for this work were capable of handling the coupled EHD, transient, free surface problem. The FLOW-3D platform which simulated the multiphase fluid flow was embedded into the CoventorWare (Coventor, Inc., Cambridge, Massachusetts) to solve the hydrodynamic problem. It used the VOF technique to track the free surface flow in the simulation.

The problem was simplified and solved as an axisymmetric problem by assuming symmetry for both liquid and electric field. The Navier- Stokes equation equation (7) describe the flow of the fluid and the Laplace equation (equation (8)) governs the electrostatic equation in both the air and the solution. No body forces were assumed for the Navier-Stokes expression

$$\rho_i\left(\frac{\partial \nu_i}{\partial t}+\nu_i.\nabla\nu_i\right)=-\nabla p_i+\nabla^2\nu_i \quad \ldots\ldots\ldots\ldots\ldots\ldots\ldots\ldots\ldots\ldots(7)$$

$$\nabla^2\phi=0 \ldots\ldots\ldots\ldots\ldots\ldots\ldots\ldots\ldots\ldots\ldots\ldots\ldots\ldots\ldots\ldots\ldots\ldots\ldots$$

…. (8)

For a leaky dielectric liquid, the charge accumulation is at the surface in the presence of electrostatic field. The expression for charge conservation is given as:

$$\frac{dG}{dt}=-n.\sigma\nabla\phi_s$$

……………………………………………………….......(9)

Where G is the interfacial charge density, σ the conductivity of the solution, d/dt is the Lagrangian derivative and n is the normal unit in the direction of the air.

The Electrohydrodynamics force exerted by the by the electric field, E was adopted from Melcher [60] and it was given by:

$$F=qE-0.5E^2\nabla\varepsilon+\nabla\left[0.5\left(\varepsilon-\varepsilon_0\right)E^2\right] \quad \ldots\ldots\ldots\ldots\ldots\ldots\ldots\ldots(10)$$

Where q is the net free charge density and the electric field $E=-\nabla\phi$. The first two terms in the expression are jointly popularly known as Korteweg-Helmholtz electromechanical force density, with the first due to the free net charge and the second due to polarization.

4.2.2 The Model and Boundary Condition

The model was based on a near field electrospinning set-up similar to the experimental setup by Sun et al. [85], where the experiment is scaled in µm. Just like the normal-scaled electrospinning, the Taylor cone and nanofibers were common features, i.e. the decrease in geometric scale does not affect the behaviour of the physics [83]. Based on these arguments, Sarkar et. al. [83] carried out the simulation on the micron scale, which helped to reduce computational time and resources.

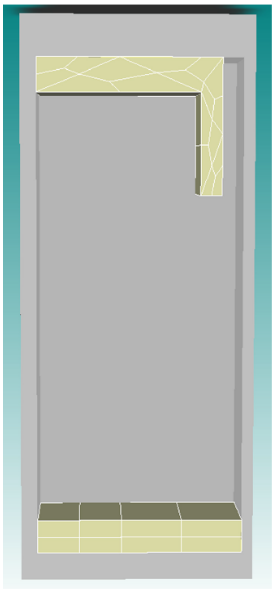

Figure 4.4- Axisymmetric model for the formation and distortion of Taylor Cone [58]

The model was an axisymmetric model (as shown Figure 4.4) with both a circular collector and jet opening. An equal but opposite electric potential was applied at the nozzle and the collector while the fluid flow was defined by a uniform velocity at the inlet of the nozzle. The solution zone was a $12\mu m \times 25\mu m$, with the nozzle diameter and nozzle to collector distance were $5.0\mu m$ and $20\mu m$. The typical cell was $270nm \times 100nm$. To aid convergence, the minimum and maximum time steps used were $0.1ps$ and $1.0\mu s$, total simulation time was set at $1.0ms$ and the electrostatic residual tolerance at 1.0×10^{-6}.

4.2.3 Results

In their work, the formation of Taylor cones was limited under the voltage range of $10kV - 30kV$ only and it was observed that the cone started forming within a few microseconds as shown in Figure 4.5. The interaction of the electric field on the flow is also shown in Figure 4.6, showing that the field zero in the bulk of the liquid, which is typical with leaky dielectrics.

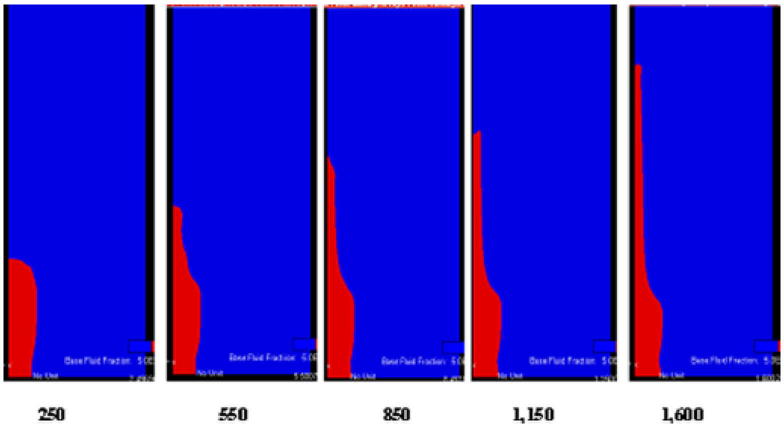

Figure 4.5- VOF at various time Steps (ns)[58]

The electric field distribution corresponds to the VOF showing a very tightly coupled relationship between the applied field and the dielectric liquid under its effect. This infers that the electrical property of the liquid can be manipulated to adjust the fluid front and hence the resultant jet. With the highest magnitude of the electric field at the tip of the jet.

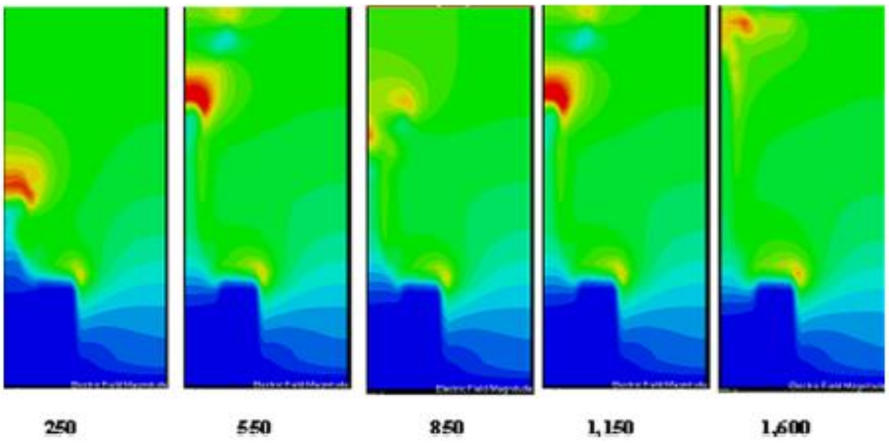

Figure 4.6- Electric field at various time steps (ns) [58]

Another critical observation deduced from the simulations was the jump in velocity within $1.6\mu s$ from $0.5 m/s$ to $24 m/s$ (about 50 times).

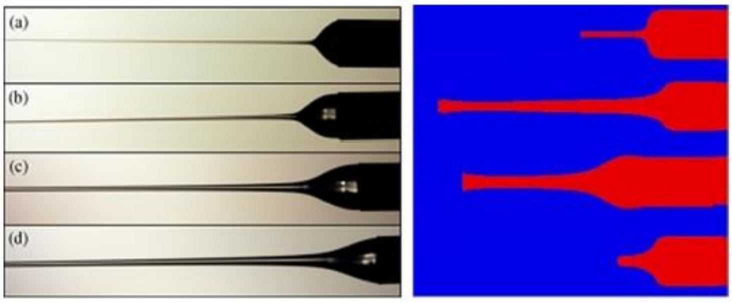

Figure 4.7- Comparison of Experimental and Simulation Results[58]

Again the analysis was limited to the onset of the jet and does not account for the whipping and the jet break-up mode of the electrospinning process. But a good approach to note was the scaling down of the geometry to a micron scale in other to save comuputational time and resources.

4.3 EFFECT OF EMITTERS AND WETTABILITY ON EHD IONIZATION

The nozzle configuration and the maginitude of the contact angle plays a critical role in the formation of both the Taylor cone and the resulting fibre and in fact the total flow front of the fluid. In their work, Wu et. al [86] investigated the effects of the flow rate, emitter tapper angle, applied voltage, contact angle (wettability/hydrophobicity) and solution conductivity on electrosprayed fluid. As shown in Figure 4.8, two types of emitters where inspected, one with a tapered angle of $45°$ and the other with a flat tip.

Figure 4.8- Emitter configuration [86]

Summarily, the Numerical approach used was the same with the generic EHD formulation and the VOF technique was also used for the liquid-gas interface tracking. Once more, *FLOW 3D* was the software suite used in the simulation.

Some of the critical observations in the work are worthy of note. The nozzle tip-collector distance was shorter than in the experiment, but was sufficient for the convergence and flow development, but this led to higher concentration of the electric field when the voltage is applied. To adjust this compromise, the flow rate was adjusted to be higher than that of the experiment; this also expedited the computation.

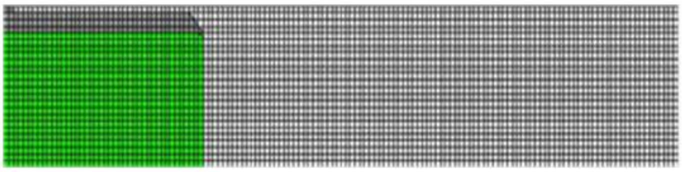

Figure 4.9- The Cartesian mesh used for the Tapered emitter [86]

The mesh sizes for the simulations were carefully set, such that the mesh across the free surface is as uniform as possible to improve convergence. A minimum mesh size of $5 \times 10^{-7} m$ was used, below this, there was no jet formation. The automatic time step was avoided and instead the time step was strictly limited to a minimum of $3 ns$, otherwise the computation was found to fail. At the right boundary, a zero-voltage plane was imposed.

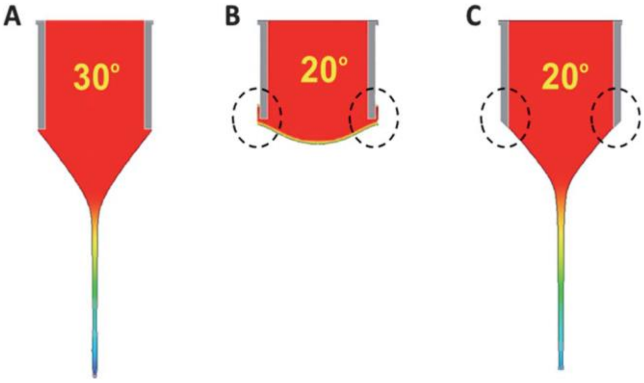

Figure 4.10- Simulated spray under (A) contact angle of 30° and flat emitter tip; (B) contact angle of 20° and flat emitter tip & (C) contact angle of 20° and tapered emitter [86]

Figure 4.10 describes the various configurations, with different contact angle (wettability) and emitter taper angle. Comparing Figure 4.10 (A and B), with the flat taper edge but different contact angles, shows that at stronger wettability, the liquid wets the emitter tip and no jet is formed. Also, comparatively, Figure 4.10 (B and C), with a tapered emitter at the same wetting condition, a stable cone-jet is supported without wetting the emitter tip. Therefore, a careful choice of both the taper angle and wettability is needed to support the required jetting in the EHD process.

It is informative to highlight, from this review, that certainly, the use of fine mesh size, logical selection of contact angle and taper angle will improve the formation of the cone-jet flow.

5. GOVERNING EQUATIONS, MATHEMATICAL FORMULATION AND NUMERICAL METHODS

In the system, two different phases exist - the liquid phase (leaky dielectric) and the gaseous phase (air). The third important medium is the capillary wall; which is made of a conductive solid material.

To fully understand the interplay of the forces, the interaction will be split into zones and interfaces, and taking a microscopic look into what happens in each case, with respect to the hydrodynamic and the electric stresses.

a. Interfaces

The Solid-Liquid Interface- Wall- The phenomenon that accounts for this interaction is referred to as electroosmosis. At the interfacial surface of the capillary wall and the liquid, the *zeta potential*[1] induces an electric double layer inside where free charges exist [54]. These free charges furthermore undergo *polarization*[2]*.* The free charges under the electric field move and result in a significant pumping force for the liquid after the induced electric field overcomes the surface tension of the liquid.

The Liquid-Gas Interface- The liquid, being a leaky dielectric, allows free charge to exist at the interface. Since the two fluids possess different electrical properties (permittivity), the electric field injects energy into the interface and causes a reduction in the contact angle. The presence of these charges generates interfacial

---

[1] Zeta potential is the charge that develops at the interface between a solid surface and the liquid medium. This potential, which is measured in milliVolts, may arise by any of several mechanisms. [117]

[2] Polarization: slight relative shift of positive and negative electric charge in opposite directions within an insulator, or dielectric, induced by an external electric field [118].

charges- the normal and tangential electrical stress. These stresses modify the fluid dynamics, especially the tangential stress which accelerates the fluid.

b. Zones

There are three zones of interest in the hydrodynamic flow with respect to the electric field: The zone within polymer, the air and the interface. But the first two experiences similar physics.

1. Polymer and Air Zones- There are little/no electric fields in the media, because the ions repel themselves and migrate towards the interface of the media. The important area of interest in the process is the interface. The free charges in these zones are negligible since, coupling only occurs at the interface/boundaries [3].
2. Interface- The free charges are confined only to the interface of the two fluids. Also, Coulomb force and polarization stress acts at the interface of the fluids. Here, the surface tension is balanced by the normal electric stress and the tangential electric stress balances the viscous force of the flow. The shear force on the interfacial charges acts as the main driving force for the jet formation. Viscous flow develops to provide stress to balance the action of the shear stress components resulting in the tangential electric field acting on the interfacial charge which accelerates the fluid.

5.1 Interfacial Stresses

At the interface of the two phases, there is an accumulation of electrodynamic charge and a coupling between the hydrodynamic forces between the two fluids [58]. At the interface, the viscous flow balances the tangential electric stress and the normal component of the electric stress is counterbalanced by the surface tension of the solution. The normal stress maintains the cone shape and the tangential electrical stress accelerates the liquid along the direction of the electric field.

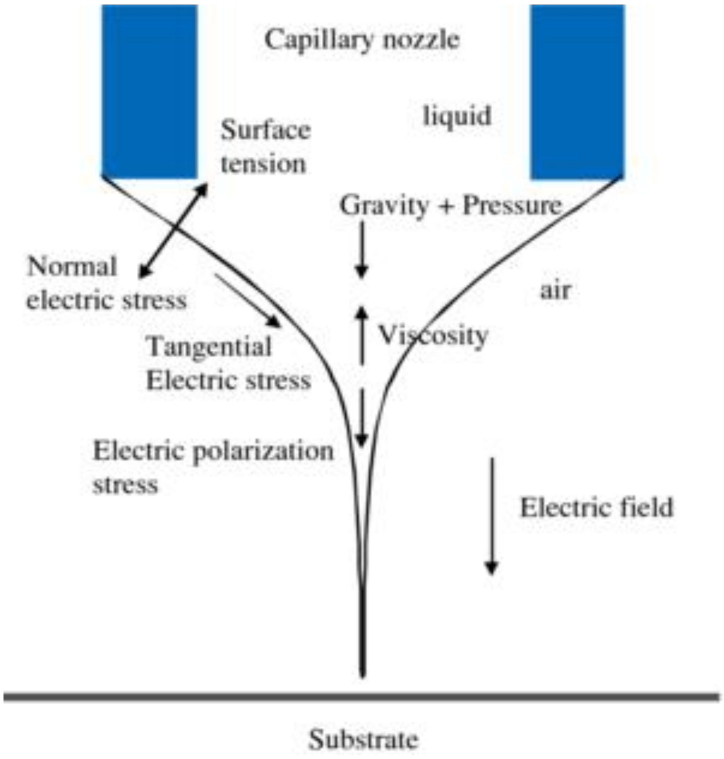

Figure 5.1- Forces acting on a liquid jet [87]. *The polarization stress comes from the permittivity gradient at the air/liquid interface and resists the local constriction of the electric field, the tangential electrical stress originates from the free surface charges on the liquid and it provides the longitudinal stretching by accelerating the jet flow, it also promotes electrical whipping mode. The Normal electrical stress arises from the self-repulsion of the free-surface charges and it balances/reduces the effect of surface tension as well as promotes whipping instability.*

Components of the Interfacial Electric Forces for a Leaky Dielectric

To understand the role of the electrical field in the EHD flow, this section will discuss the three additional stresses acting at the interface of the jet; analysing their sources and the effects of the components. Table 5.1 shows a summary of the electrostatic forces on an electric jet, highlighting the sources, effects and the mathematical expressions describing these forces in terms of the applied electric field, electric charge and permittivity of the medium.

Table 5.1- Summary Electric forces on electrified jets

COMPONENT	SOURCE	EFFECT	EXPRESSION
Polarization force	Permittivity gradient at the liquid-gas interface	Resist the local constriction of the electric field	$\frac{1}{2}E^2\nabla\varepsilon$
Tangential electric forces	Free surface charge	• Provides longitudinal stretching by accelerating the jet flow • Promotes electrical whipping mode	
Coulombic/Normal electric forces	Self-repulsion of the free-surface charges.	• Balances and reduces the effect of surface tension • Promotes electrical whipping mode	qE

There is a large jump in electric field across the interface (free surface) of the jet profile. This jump is responsible for both the tangential and normal electric stresses. The normal stress is attributed to maintain the conical shape of the liquid, while the tangential component accelerates the liquid in the direction of the resulting jet [88].

For leaky-dielectrics, the coupling of the hydrodynamics and electric fields occurs only at the liquid-air boundaries/interface- where electric stresses that are different from those of perfect conductors and dielectrics are developed by charges carried to the surface by conduction [3].

BISECT RULE

To further understand the role and direction of action of the forces, Chen [89] describes the bisect rule which will allows us to graphically identify the direction of the electric stresses given that the direction of applied electric field is known.

According to Panofsky and Philips [90], from Figure 5.2 the Bisect Rule states that: “For a surface dS, in a dielectric medium with permittivity of ε, the electric field (E)

bisects the angle between the normal to the surface (n) and the resultant force (F^e) whose magnitude is $T^e dS = \frac{1}{2}\varepsilon E^2 dS$. ”

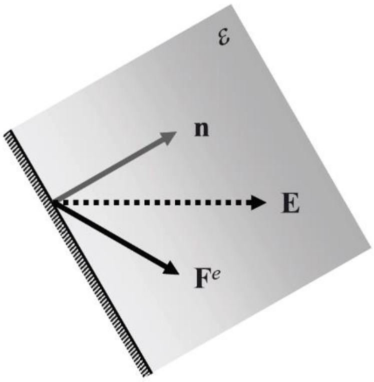

Figure 5.2- The Bisect Rule [90]

Figure 5.3 shows the different applications of this rule for various liquids under the action of an electric field.

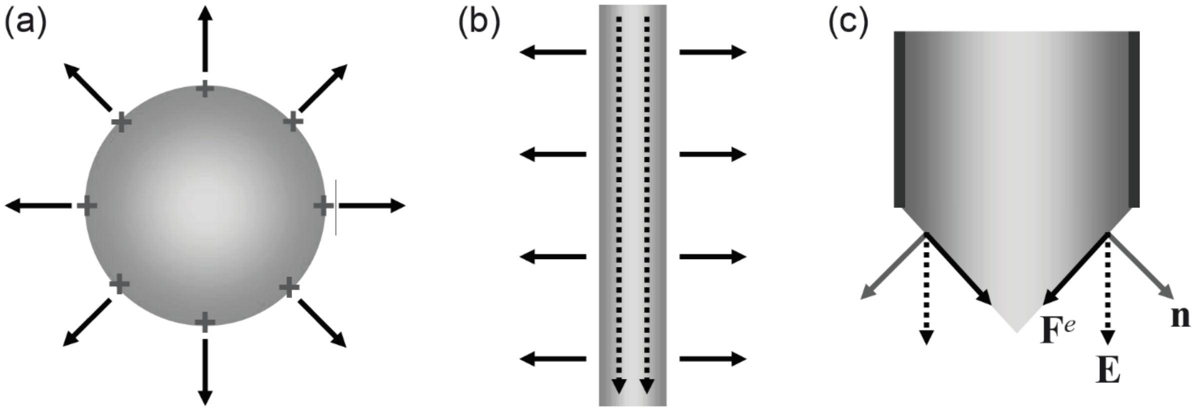

Figure 5.3- Applications of Bisect Rule- (A) Perfect conductor; (B) Perfect Dielectric; (C) Leaky-Dielectric [90]

For a perfect conductor (with zero permittivity), as shown in Figure 5.3 (A), the coulombic force which is due to free charges acts along the electric field which is perpendicular to the free surface. Figure 5.3 (B) depicts a perfect dielectric (insulator, with zero conductivity), where the polarization force acts along the electric field and is perpendicular to the interface. The third scenario is the case of a leaky-dielectric (i.e. non zero permittivity and conductivity), a tangential stress develops on the cone interface, where the electric field is at 45° to the normal, as shown in Figure 5.3 (C) [89], [90].

Similarly, the electric stress is normal to and changes with the interface profile alongside the surface tension (which balances the electric stress) in the case of perfect conductors and perfect dielectrics. Whereas for leaky-dielectrics, the interfacial charges alter the electric field, thereby giving rise to the development of a viscous flow to balance the resultant force due to the tangential components at the interface [88].

Summarily, the electric stress acts perpendicularly to the interface for both the perfect conductor and dielectric. But for the leaky-dielectric, the accumulated free charges on the interface totally modifies the field. A resultant viscous flow (which is stretched and accelerated) then develops to provide forces that counter-balances the action of the tangential component of the field.

5.2 General momentum balance equation of a leaky dielectric fluid

The differential equations describing EHD arise from combination of equations describing the conservation of mass and momentum for a continuum phase (or multiple continuum phases), and Maxwell's equations [3]. The Maxwell stress tensor is what couples the electrostatic and hydrodynamics equations, hence it is essential in the formulation of EHD problems [89]. The interaction of the electric and hydrodynamic stress causes either an oblate or prolate deformation in the drop. The forces acting on the system account for the liquid deformation and charge distribution [48]. The leaky dielectric model assumes the fluid medium acts as an ohmic conductor i.e. the conductivity is constant. This assumption is valid for fluids with more or less constant properties (for example constant density, i.e., an immiscible phase and incompressible flow). Therefore, it is the combination of a Charge Transport Model and the Navier-Stokes equation that forms the leaky dielectric model [91].

The two important models in the formulation of the EHD problems are the Ohmic model and the Maxwell stress tensor- which plays the critical part of coupling the electrostatics and hydrodynamics.

5.2.1 THE OHMIC MODEL

The Ohmic model provides an approximation for the EHD phenomena [55], [89]. In this model, the EHD is approximated as being electroquasistatic and the effect of the magnetic field is negligible and can be ignored and it is thus solenoidal and described by:

$$\nabla \times E = 0 \tag{11}$$

The electric field, E follows the Gauss's law, which is approximated as

$$\nabla \cdot \varepsilon E = q \tag{12}$$

where ε is the permittivity of the medium and q is the free charge density of the applied electric field.

In a leaky-dielectric model, an Ohmic constitutive law of current is assumed [55], with the diffusive current ignored.

$$i = i_c + i_o = qv + \sigma E \tag{13}$$

where i_c is the convective current and i_o is the ohmic current.

The charge conservation equation relates the free charge density is related to current, (i) by:

$$\frac{\partial q}{\partial t} + \nabla \cdot i = 0 \tag{14}$$

Therefore,

$$\frac{\partial q}{\partial t} + \nabla \cdot qv + \nabla \cdot \sigma E = 0 \tag{15}$$

The expression in (15) describes the charge conservation in the ohmic region, where the electric field, $E = -\nabla \phi$

The Ohmic model includes both the conductivity and free density charge conservation equation. The two most important assumptions in this model are that the diffusive current and the instantaneous charge relaxation are negligible. These assumptions are relevant for an EHD process driven by a direct current (DC) field, where the time scale and length scale of interest are typically larger than $1ms$ and $1\mu m$ respectively. Generally, the ohmic law is not applicable in the case of an electric double layer where the length of interest of the charged layer is less than $1\mu m$.

5.2.2 THE MAXWELL STRESS TENSOR

The electric force density, f^e can be derived either by the Kelvin (K) approach or the Korteweg-Helmhotz (KH) approach. The former is useful for appreciating the underlying microscopic electromechanics, while the latter is useful for estimating the effect of electromechanical coupling [92]. The KH model will be adopted in this work.

The Kelvin force density f_k^e is a sum of Coulombic forces exerted on the free charges and the polarization force in the dipole [92]. It is given as:

$$f_k^e = qE + P_r \cdot \nabla E$$

$$= \left(\nabla \cdot \varepsilon E\right) E + \left(\varepsilon - \varepsilon_0\right) E \cdot \nabla E$$

$$f_k^e = \nabla \cdot \left(\varepsilon EE - \frac{1}{2} \varepsilon_0 E^2 I \right) = \nabla \cdot T_k^e \tag{16}$$

where P_r is the polarization density, I is the identity matrix and T_k^e is the Maxwell stress tensor corresponding to the Kelvin force density.

The Korteweg-Helmhotz force density for the medium with mass density (ρ) and temperature (T) can be shown to be

$$f_{KH}^e = qE - \frac{1}{2} E^2 \nabla \varepsilon + \nabla \left[\frac{1}{2} \rho \left(\frac{\partial \varepsilon}{\partial \rho} \right)_T E^2 \right]$$

$$= \nabla . \left[\varepsilon EE - \frac{1}{2} \varepsilon E^2 I + \frac{1}{2} \rho \left(\frac{\partial \varepsilon}{\partial \rho} \right)_T E^2 I \right] = \nabla \cdot T_{KH}^e \tag{17}$$

where T_{KH}^e is the Maxwell stress tensor corresponding to Korteweg-Helmhotz force density and the last term in equation (17) describes the electrostriction force density associated with the volumetric change in the medium, which is usually neglected since the medium we are dealing with incompressible medium and the permittivity is constant.

Generally, for an electrically linear and incompressible dielectric medium, adopting the KH approach, the electric force density is given as:

$$f^e = qE - \frac{1}{2}E^2\nabla\varepsilon = \nabla \cdot T^e \qquad (18)$$

The electrical force also known as Maxwell Stress Tensor, is given as the sum of Coulombic Force and Polarization Stress. Both of these act at the interface, since the electric charges are located at the air-liquid interface. The first term in equation (18) describes the Coulombic force while the Polarization force (also known as the dielectric force) is represented by the second term.

The Coulombic force is the force per unit volume on the medium containing the free electric charge and it is the strongest EHD force, while the Polarization force, otherwise known as the dielectrophoretic force is due to the exerted force by an electric field on a non-homogeneous dielectric fluid region [64].

The solver computes the electric field distribution from the applied electric potential on the wall of the emitter/needle. The solver allows the Poisson's equation to be solved either by Boundary Element Method (BEM) or Finite Volume Method (FVM) and whichever method accounts for the relative permittivity, space charge, and electrical conductivity of the system. The FVM method in the CFD-ACE+ solver has the capacity to effectively solve complex multiphysics and nonlinear problems as in the case of this work, therefore it is favoured above the BEM technique. The range of applied potential for this work is a direct current of magnitudes $4-25kV$.

Dielectrics and Electrostatic Fields

The combination of stationary charges and applied potentials results in the generation of electrostatic fields. This field is governed by the Gauss' Law, which states that "the net electric flux passing through a closed surface is equal to the net charge enclosed by the surface" [5]. For an electric flux density $\left(C/m^2\right)$, D and a volume charge density $\left(C/m^3\right)$, q , the Gauss' law is expressed as:

$$q = \nabla \bullet D \tag{19}$$

The flux density and the electric field, E are related by:

$$D = \varepsilon E \tag{20}$$

Where,

$$\varepsilon = \varepsilon_m \varepsilon_o \tag{21}$$

ε , ε_m , ε_o denotes the permittivity of the medium, dielectric constant of the medium and permittivity of the free space respectively.

The vector electric field is considered to be irrotational (i.e. the curl of the electric field is zero) [6]:

$$\nabla \times E = 0 \tag{22}$$

Therefore, the scalar electric potential ϕ is expressed as:

$$E = -\nabla \phi \tag{23}$$

The Poisson's equation for the electric potential, which CFD-ACE+ solves is obtained by combining equations (20), (21) and (22) into the Gauss' law as given in equation (19). The equation is given as:

$$\nabla \cdot \left(\varepsilon_m \varepsilon_o \nabla \phi\right) \tag{24}$$

This expression is used to solve the electric potential, once computed the value of ϕ is used to evaluates other quantities like surface charge, electric field distribution, etc. [69]. The magnitudes of E is evaluated in the dielectric medium and in the free space surrounding it.

For the interface between two dielectric media, a and b with the normal electric field E_n on either side of the interface, the displacement of the electric flux density is kept at equilibrium; this is expressed mathematically as follow:

$$\varepsilon_a E_{n_a} = \varepsilon_b E_{n_b}$$

Summary of the Governing equations for the flow

The first three equations that follow govern the processes involving the electric charge, whereas the fourth equation is conservation of mass and the fifth one conservation of momentum, in the presence of electrical loading:

$$\nabla \times E = 0 \qquad (25)$$

$$\nabla.\varepsilon E = q \qquad (26)$$

$$f_e = qE - \frac{1}{2}E^2 \nabla \varepsilon \qquad (27)$$

$$\nabla.\vec{u} = 0 \qquad (28)$$

$$\rho \frac{\partial \vec{u}}{\partial t} + \rho \vec{u}.\nabla \vec{u} = -\nabla p + \mu \nabla^2 \vec{u} + \rho g + f_e \qquad (29)$$

where, the electric charge, $q = \nabla.\varepsilon E$, the electric field, $E = -\nabla\emptyset$, the Mechanical Stress $= -\nabla p$ and the Viscous Stress $= \mu \nabla^2 \vec{u}$

Summary of Governing equations for the electric field

In the bulk (solution and air), where the conductivity and permittivity are uniform, the net free charge decays with relaxation time (i.e. the electric field and the charge densities approach zero) [55]; here the charges align themselves and migrate to the interface to cancel out the field effect.

$$q = q_0 e^{-t/\tau} \tag{30}$$

where the bulk relaxation time, $\tau \equiv \varepsilon/\sigma$ and σ represent the electrical conductivity of the liquid.

Also, the Laplace equation governs what happens in the bulk and the interface is given as:

$$\begin{aligned} \nabla^2 \phi &= 0 \\ \nabla . \mathrm{E} &= 0 \end{aligned} \tag{31}$$

The tangential components of the electric field, $E = -\nabla\phi$ is continuous, but on the contrary, in the normal direction, there is a jump in the electric field which is proportional to the magnitude of the surface charge, q , this expression is given as:

$$\vec{n} . \left(\varepsilon_l \nabla \phi_l - \varepsilon_m \nabla \phi_m \right) = q \tag{32}$$

$$\vec{t_i} . \left(\varepsilon_l \nabla \phi_l - \varepsilon_m \nabla \phi_m \right) = 0$$

where t_i depicts either of two orthogonal tangent vectors embedded in the surface.

At the Fluid-Fluid Interface, where the free charges accumulate to produce a shear stress, the charge conservation equation represents the charge density and it is given as:

$$\frac{dq}{dt} = -\vec{n}.\sigma\left(\nabla\phi_l\right) \tag{33}$$

where d/dt is the Lagrangian derivative. The normal $\left(T_n\right)$ and tangential $\left(T_t\right)$ electrical stresses induced due to the electric field, acting normal to the interface are given by equations (34) and (35) respectively by:

$$T_n = \frac{1}{2}\left[\varepsilon_l\left(\vec{n}.\nabla\phi_l\right)^2 - \varepsilon_m\left(\vec{n}.\nabla\phi_m\right)^2\right] \tag{34}$$

$$T_t = -q\left(\vec{t}_i.\nabla\phi\right) \tag{35}$$

CFD-ACE+ (ESI Group, Paris, France) is used to cast the model described for the modelling of the Electrohydrodynamics (EHD) phenomenon for generating fibres through electrospinning process. The approach embraced is to simultaneously solve the coupled electrostatic and EHD equations. The model developed has the capability of handling the trio of flow, free surface and electric components of the process in a fully coupled manner. The solution sequence is such that the electric body forces are determined from the electrostatic field and then included in the Navier-Stokes equations. The permittivity of the liquid is the key property in coupling the equations.

5.2.3 Discretization

The Finite Volume Method is adopted to discretize the differential equations into algebraic equations, due to its conservation properties [93]. The domain is divided into number of control volume (cells) and the governing equations are integrated over the individual cells. By applying the Gauss Divergence theorem, this integration results in converting the volume integrals (applicable to every control volume) into surface integrals (which apply to the boundaries – faces – of each control volume. On the same note, the derivatives become projections of the function on the direction normal to the face [94].

The values of all variables are needed at control-volume faces and the resulting set of algebraic equations is solved iteratively to convergence. The Gauss Divergence Theorem relates the source of a field in a volume V with the flux of that field through the boundary surface S of that volume

$$\int_V \left(div\vec{F} \right) dV = \int_S \left(\vec{n}.\vec{F} \right) dS \quad (36)$$

The physical interpretation of $\vec{n}.\vec{F}$ is the component of $\vec{F}$ in the direction of the vector $\vec{n}$ normal to surface element dS .

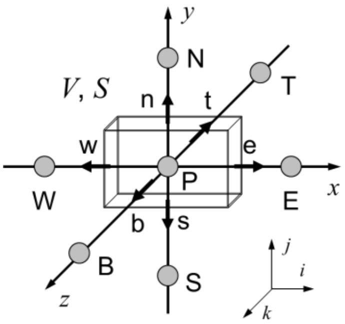

Figure 5.4 Description of the Gauss' Divergence Theorem for a source field in a volume. [93]

The integral of $div\vec{F}$ is equal to the component of $\vec{F}$ in the direction normal to the surface which bounds the volume integrated (i.e. summed) over the entire surface S.

$$\int_{S}\left(\vec{n}.\vec{F}\right)dS = \sum_{i=1}^{6}\int_{S_i}\left(\vec{n}.\vec{F}\right)dS \qquad (37)$$

Figure 5.5 shows examples of a typical cells/control volumes. Both structured or unstructured cells were used. This approach allows for the solution of the general transport equation, taking the generic form of equation (38) for a certain quantity ϕ.

$$\frac{\partial\rho\phi}{\partial\mathrm{T}} + \nabla\cdot\left(\rho\vec{\mathrm{V}}\phi\right) = \nabla\cdot\left(\Gamma\nabla\phi\right) + S_{\phi} \qquad (38)$$

The first term in the equation represent the transient term. The second on the left-hand side is the convective term and the first term to the right-hand side is the diffusive term and the last term is the source, which in this case is the electrostatic field, or the pressure gradient.

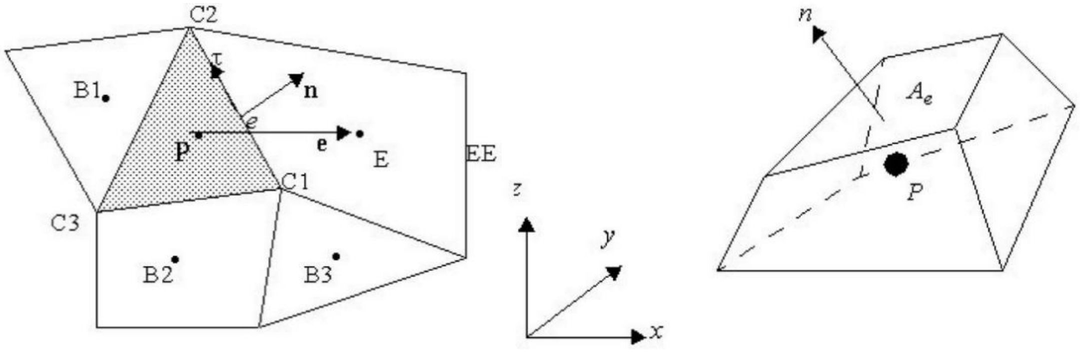

Figure 5.5: Axisymmetric & 3D Computational cell / control volume[69]

Terms in the momentum equation (38) are discretized in algebraic form by integrating each term of the equation over each cell. In CFD-ACE+, various interpolation schemes with varying levels of numerical accuracy, stability and compromise are available and it allows to choose whichever is suitable for the case in question. For this problem, both the First-Order Upwind scheme and Central Differencing scheme have been tested.

For the First-order upwind scheme, the value of the property, ϕ at a cell face e, given as ϕ_e is taken to be the value of the property at the grid point upstream and depending on the direction of flow, it is equal either cell centres, ϕ_P or ϕ_E as shown in the axisymmetric computational cell volume in Figure 5.5. This is represented mathematically in equation (39). The scheme is reported to have a first-order accuracy and is very stable yet quite dissipative [69].

$$\phi_e^{UP} = \begin{cases} \phi_P \text{ if } \mathrm{V}_e^n > 0 \\ \phi_E \text{ if } \mathrm{V}_e^n < 0 \end{cases} \tag{39}$$

Meanwhile, in the Central differencing scheme ϕ_e is evaluated arithmetically by averaging the values at the cell centres P and E, assuming a linear variation of ϕ between the cell centres. Mathematically, the average value is expressed thus:

$$\phi_e^{CD} = \Upsilon_e \phi_P + \left(1 - \Upsilon_e\right)\phi_E \tag{40}$$

Where Υ_e describes the geometrical weighting function at face e.

To correct possible stability problems associated with the central differencing scheme, a scheme with damping was constructed with a blending factor, α that combines both the central scheme and first-order accurate upwind scheme to produce a more stable scheme. Hence the expression for the modified scheme was given as:

$$\phi_e = \alpha \phi_e^{UP} + \left(1 - \alpha\right)\phi_e^{CD} \tag{41}$$

The accuracy of this scheme is between 1st and 2nd order, and it can be observed that when $\alpha = 0$, it yields the conventional second-order accurate difference scheme, while at $\alpha = 1$, it yields the first-order accurate upwind scheme.

For this work, a blending factor of 0.1 was used making the expression (41) to become:

$$\phi_e = 0.1\phi_e^{UP} + 0.9\phi_e^{CD} \tag{42}$$

This takes the blend of the convergence trait of the upwind scheme and the accuracy of the second-order accurate difference scheme.

5.2.4 Algebraic Form of Finite Volume Method

If numerically integrated, all the terms in equation (38) and assembled together, a linear equation is formed thus:

$$(a_p - S_p)\phi_p = \sum\nolimits_{nb} a_{nb}\phi_{nb} + S_u \tag{43}$$

This equation gives the discrete and matrix equivalent of the transport equation (38). Where the subscripts nb denotes the neighbouring cells, a_{nb} and a_p are the link coefficients. When computed for each cell, it results in a set of coupled non-linear algebraic equations which no direct matrix inversion method can solve. Hence, an iterative procedure is needed and adopted for each time step. In effect, a linear system of equations is formed by evaluating the link coefficients with the values of ϕ available at the end of previous iterations.

5.2.5 Velocity-Pressure Coupling

The continuity equation cannot be written in the form of the general transport equation, and as such its solution procedure is different.

The mass conservation is written as:

$$\frac{\partial \rho}{\partial t} + \nabla \bullet \left(\rho \vec{V} \right) = \dot{m} \tag{44}$$

When integrated over the cell and over a time step, the mass conservation equation becomes:

$$\frac{\rho \upsilon - \rho^0 \upsilon^0}{\Delta t} + \sum_e \rho_e V_e^n A_e = \dot{m} \upsilon \tag{45}$$

where V_e^n is the face-normal component for the velocity at the face e, obtained by the inner product of the velocity and the face-normal nit vector, given as:

$$V_e^n = u_e n_x + v_e n_y + w_e n_z \tag{46}$$

The fluid density and velocities are only at the cell centres; hence their faces values needs to be interpolated from the centres. The process of linear interpolation de-couples the velocity and pressure giving rise to checkerboard instability [90]. This problem is circumvented by evaluating the cell-face mass flux by averaging the momentum equation to the cell faces and then relating the cell face velocity to the local pressure gradient. With the face values of both velocity and density obtained, the mass flux evaluation is then completed.

5.2.6 Pressure Correction and SIMPLEC Algorithm

There is no governing PDE for pressure even though it is an important flow variable. Pressure-based methods use continuity equation to formulate an equation for *pressure correction*. The SIMPLEC (Semi-Implicit Method for Pressure-Linked Equations Consistent) scheme is adapted for pressure-correction in this work. It is characteristically an iterative method.

A finite volume form of the momentum equation is written as:

$$a_P u_P = \left(\sum\nolimits_{nb} a_{nb} u_{nb} + S_u\right)_P - \left(\sum\nolimits_e P_e A_e n_{xe}\right)_P \tag{47}$$

To solve the velocity field, u the pressure field should be provided but however, the pressure field is not known. The expression (47) is thus solved by guessing a pressure, P^*, which invariably yields velocity u^*, which satisfies the expression:

$$a_P u_P^* = \left(\sum\nolimits_{nb} a_{nb} u_{nb}^* + S_u\right)_P - \left(\sum\nolimits_e P_e^* A_e n_{xe}\right)_P \tag{48}$$

Both u^* and P^* do not satisfy continuity and so we need to find corrections to them so as to obtain a solution with the corrected value of u and P, taking u' and P' as the corrections.

$$u = u^* + u' \tag{49}$$

$$P = P^* + P' \tag{50}$$

Summarily, expressions for correction to the face-normal velocity and pressure are obtained, as in equation (51) and (52)

$$V_e^{n'} = u_e' n_x + v_e' n_y + w_e' n_z \tag{51}$$

$$a_p P_p' = \sum_{nb} a_{nb} P_{nb}' + s_m \tag{52}$$

5.3 The Volume of Fluid (VOF) Approach for Free Surface Flows

Free surfaces connote the interface/boundary of fluid-fluid flow, the fluids usually with large density difference, approximately 1000:1 (liquid-gas). This difference usually occurs in a gas-liquid interface. It is from this variation in density magnitude that the term ‘free’ comes in Hirt [95] pointed out that the pressure exerted by the gas is the only influence it has on the liquid. The solution of a free surface flow problem involves finding the free surface location and the flow field bounded by it [96].

Free-surface problems can be categorised into two groups: first are problems in which the solution depends only weakly on the shape of the free surface e.g. most problems involving fluids with negligible surface tension; the second are those problems in which surface tension is a dominant influence [96]. This thesis falls into the second category.

Various methods have been used to solve free surface problems depending on the scheme used to form the discretisation of the spatial domain and the surface boundary including Boundary-element methods, finite-difference methods (like Marker-and-cell, Volume of fluid and phase field) and the finite element methods (e.g. fixed-connectivity meshes and unstructured meshes) [96]. The VOF method is the technique adopted in this work.

The basic idea of the VOF, developed by Hirt [95] was to introduce a fraction F assigned to each cell. This fraction represents the portion that is occupied by the liquid phase. Descriptively,

$$F(\mathrm{x,y,z,t}) = \begin{cases} 0 \; \textit{the gas cell} \\ 1 \; \textit{the liquid cell} \\ 0 < F < 1 \; \textit{two phase cell / free surface} \; \mathrm{int}\textit{erface} \end{cases} \tag{53}$$

The VOF technique plays a critical role in tracking the transient flow of the immiscible fluids, of all the various methods of interfacial tracking, CFD-ACE+ uses the VOF technique taking account the effect of surface tension. The solver handles VOF problems based on the work of Hirt and Nichols [68]. The volume fraction, F, of the second fluid (Fluid 2) is used to track the relative mixture of the two fluids within the domain, expressed as:

$$F = \frac{F_2}{F_{1-2} = F_1 + F_2} \qquad (54)$$

The subscripts represent the volume of fluid 1 and fluid 2. The value of $0 \geq F \geq 1$. CFD-ACE+ treats the denser fluid as the secondary fluid and the other as the primary fluid, in this work, water is the fluid 2 and air is taken as the fluid 1. The interface shape is reconstructed by interpolation to determine the isosurface corresponding to a value of $F = 0.5$. The VOF module in CFD-ACE+ accommodates density ratio, r_ρ of fluid 2 to fluid 1 between $1:1000 \leq r_\rho \leq 1000:1$. CFD-ACE+ also account for the effects of surface tension and the PLIC surface reconstruction technique is used to determine the shape of the interface of the two fluids. CFD-ACE+ only allows running the VOF problems as transient once activated.

Volume Fractions

The transport equation given in equation (55) is used to determine the distribution of F in the flow field. The unique feature of the VOF technique for interface tracking is that the distribution of the Fluid 2 is accounted for in the computational domain using the scalar field variable, F, that specifies the fraction of the cell in the domain occupied by fluid 2.

$$\frac{\partial F}{\partial t} + \nabla \bullet \vec{u} F = 0 \qquad (55)$$

where F is the liquid fraction, t is the time, ∇ is the spatial operator and $\vec{u}$ is the velocity vector. The expression (55) is solved simultaneously with the mass and momentum conservation in the solver to achieve the required computational coupling between the liquid distribution and velocity field solution.

The nature of the distribution is such that F takes a value of 1 in cells containing fluid 2 and a value of 0 reflects that the cell contains only fluid 1. Other cells coincident with the interface takes values between 0 and 1. Other aspects of the VOF module include the computation of mixture properties, reconstruction of the liquid-air interface and the determination of the resultant contribution of the secondary flux to the mass conservation, momentum conservation, electric and volume fraction.

Mixture Properties

The average value of any fluid property, χ (including density, viscosity etc.) in any computational cell is determined by the proportions of the two fluids in the mixture, it is calculated using:

$$\chi = F\chi_2 + \left(1 - F\right)\chi_1 \tag{56}$$

Where subscript (1) represent the gaseous phase and the subscript (2) represents the liquid phase.

Likewise, for a mass-specific flow property, the effect of density must be included, and the intended fluid property is computed thus:

$$\chi = \left[F\rho_2\chi_2 + \left(1 - F\right)\rho_1\chi_1\right]\rho_{mix} \tag{57}$$

Surface Reconstruction

The VOF is a volume-tracking technique, since a single scalar variable is used to describe the fluid 2 distribution and solve the liquid volume front evolution. This directly implies that in the phase distribution, there is no unique definition of the interface between the phases. To adjust this drawback, there must be a dynamic reconstruction of the F distribution, thereby enabling the modelling, computation and visualization of the interface location.

In CFD ACE+, the reconstruction is an important step in determining the surface curvature (when the surface tension effect is accounted for) and the flux of F from one cell to another. There are three methods to implement surface reconstruction in the solver:

a. An upwind scheme with the Piecewise Linear Interface Construction (PLIC),
b. An upwind scheme with the Single Linear Interface Construction (SLIC), and
c. A 0th order upwind scheme (FOAM).

For this work, second-order PLIC is used for surface reconstruction, it is the most accurate of the three. Here, the liquid-gas interface is assumed to take a planar surface and subsequently allowed to take any orientation with the cell, this interface hence will generally take the shape of the arbitrary polygonal face.

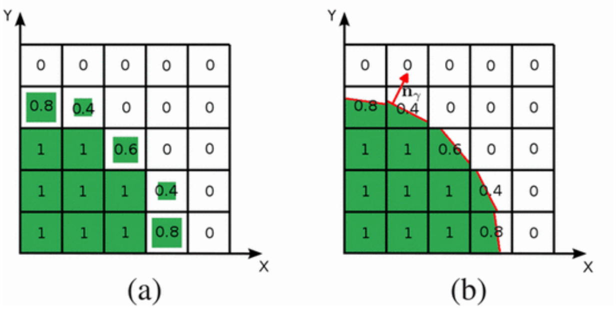

Figure 5.6- VOF method with PLIC. (a) Distribution of Fluid 2. (b) PLIC reconstruction of the interface [71].

Figure 5.6 illustrates the PLIC technique for VOF, which tracks the multiphase flow of the advection of the material distribution. The fluid is represented by the volume fraction for each cell, and the interface is bounded by a sharp interface due to numerical diffusion caused by repeated interpolation [97]. Note that higher-order PLIC supports the inclusion of surface tension in the solver, therefore it is preferred.

Secondary Fluid Flux Calculations

Using back projection technique from the cell face, the flux for the secondary fluid can be determined once the interface shape and orientation in the upwind cell is determined from the second-order PLIC reconstruction method. Figure 5.7 shows the concept for the calculation.

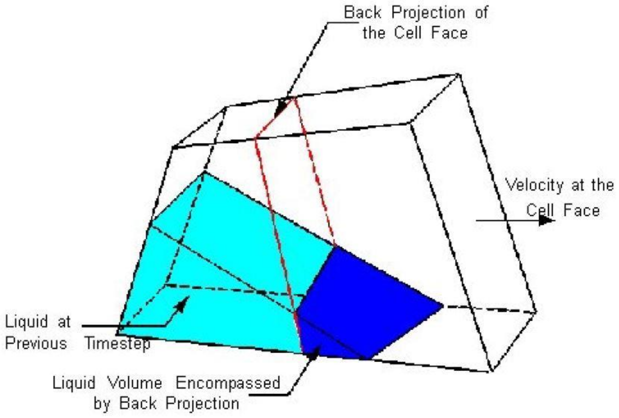

Figure 5.7- Computation of secondary fluid flux in the PLIC technique by back-projection from a cell face [93]

The back-projection technique leaves two major implications:

a. The secondary fluid flux is computed explicitly based on old liquid surface orientation.
b. It works based on the information from the upwind cell only.

This means that the surface advection computation is explicit and there is an intrinsic stability limit imposed on the timestep magnitude within the grid, this limit is given by the Courant Condition, expressed thus:

$$\Delta t_c = \frac{d_c}{|\bar{\upsilon}_c|} \tag{58}$$

Δt_c is the maximum allowable time step in a cell, c , $\bar{\upsilon}_c$ is the local velocity and d_c is the local cell dimension. The Courant–Friedrichs–Lewy (CFL) number is defined by:

$$\frac{\Delta t_c |\bar{\upsilon}_c|}{d_c} \tag{59}$$

The CFL defines the distance covered by any phenomenon at the local velocity defined in equation (58) as a fraction of the local cell dimension. This number is kept at a condition of $CFL < 1$ for stability of the algorithm used to integrate equation (59)

In CFD-ACE+, CFL can be activated when the option of the automatic time step is used. Practically, this option means that the time step size for the mixed cells (for both primary and secondary cells) must be restricted such that the free surface crosses less than a cell at within a time step. For this work, a CFL of 0.1 has been used, which is the default as advised by CFD-ACE+.

Surface tension

Since the higher-order PLIC is used for the surface reconstruction, the surface tension force effect is included in the solver for free surface module. In CFD-ACE+, surface forces are computed based on the equilibrium of a curved surface under surface tension. The magnitude of the net normal force acting on the curved surface is equal to total resultant tangential forces T, due to the surface tension γ between the two fluids. The tangential force is expressed by:

$$\mathrm{T} = \gamma \vec{n} \times \frac{d\vec{x}}{|d\vec{x}|} \tag{60}$$

Consequently, this leads to:

$$\int \Delta p ds = \int \gamma \vec{n} \times d\vec{x} \qquad (61)$$
$$\vec{n} = \nabla F$$

The surface tension formulation in CFD-ACE+ does not require information on the global interface shape but the local geometry of the interface edges within each computational cell. The surface tension model is implemented in CFD-ACE+, in the following sequence:

i. Determination of the fluid-fluid interface at each face.
ii. Evaluation of the unit normal at the interface.
iii. The integral in equation (61) is applied to determine effective cell volume force.

Contact Angle

The contact angle for a multiphase system is said to be determined by the thermodynamic free energies of the phases involved, and it is usually taken constant in the system [98], even though practically, the magnitude of the contact angle is a function of free energies, surface roughness, velocity of liquid (near the contact line), ambient flow, temperature field etc. To account for these variables, CFD-ACE+ solver allows the module to be implemented such that instantaneous contact angle either by writing a user *‘ubound user-subroutine’* or specifying the contact angle at the various boundary condition. For this work the contact angle is specified for each boundary condition.

At the walls, the contact angle boundary condition can be specified between 0-180 degrees, with 0 degree meaning a full wetting and 180 degrees relating to a condition of no wetting, other values of $0 < \text{contact angle} < 180$ shows different amount of partial wetting. Once this angle is evaluated at a certain contact point, it is then enforced through the boundary condition within the surface tension model in CFD-ACE+ solver. After the associated momentum source terms and curvature has been determined in the fluid-fluid interface cells, this treatment is applied using the interior scheme.

The source term vector in the contact-point/contact-line cell only accounts for the presence of other cells before the application of the contact angle boundary condition and not the presence of the boundary, but after the application, the momentum source term is rotated in the contact-point/contact-line cell so that the vector becomes directed along the interface normal. Figure 5.8 shows the geometry and angle of a contact-point x_w on a wall. This normal, $\hat{n}$ is hereby determined as a function of the computed contact angle according to equation (62):

$$\hat{n} = \hat{n}_w \cos\theta + \hat{t}_w \sin\theta \qquad (62)$$

θ is the computed contact angle between the fluid-fluid interface and the wall, $\hat{n}_w$ is the unit normal directed into the wall and $\hat{t}_w$ is the unit tangent to the wall directed into the liquid phase.

Specifically, for this work, a partial wetting is assumed at the wall of the emitter/needle with a contact angle of 30° and a full wetting on the collector/target, assigning a contact angle of $0°$

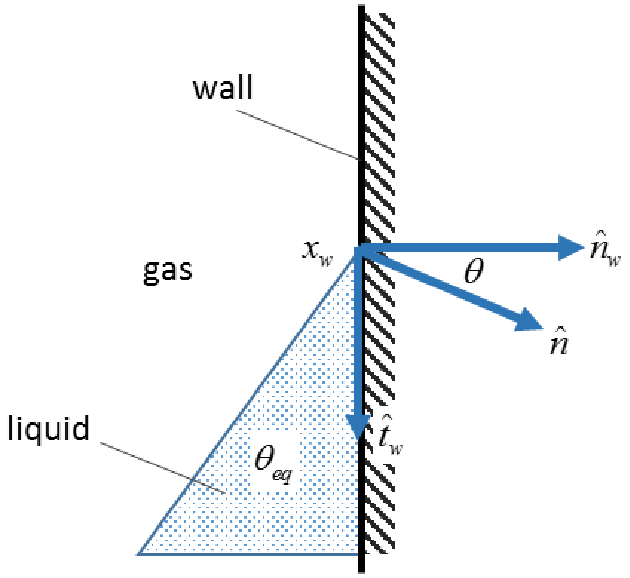

Figure 5.8- Contact Point Geometry and Angles [93].

Finally, for the free surface (VOF) module, the virtual electrostatic (dielectric) force is activated to account for the electromagnetic body force due to an inhomogeneous permittivity distribution in the system due to the two-phase flow. The explicit time-integration scheme is used to specify how the secondary fluid fraction, F evolves. It corresponds to a Forward-Euler scheme, where the fluxes are evaluated from the fluid fraction at the previous time-level. This scheme is more stable and converges faster, even though it is less accurate than the implicit scheme. These effects of stability and convergence become more pronounced when the flow parameters that drive the system is dependent on the distribution of the secondary fluid.

5.3.1 Solution Techniques

A segregated solution method is employed, where the sets of equations for each variable are solved sequentially and repeatedly until convergence is achieved. The procedure adopted for this work is presented in Figure 5.9.

The overall residual determines the number of iterations performed. For each iteration, the residual for each variable is computed which is an equivalent of the sum of the absolute value of the difference between the right and the left had side of the equation for the variable at each control volume. The solution is taken to have converged when a reduction of five orders of magnitude is observed in the residual. For this work, on average, 50 iterations were needed for a residual reduction to 1×10^{-6} .

5.3.2 Under-Relaxation

This is used to constrain the change in the variables (both dependent and auxiliary variables) from iteration to iteration, so as to prevent divergence of the solution. This is achieved by modifying Equation (43):

$$a_p(1+I)\phi_p = \sum\nolimits_{nb} a_{nb}\phi_{nb} + S_u + a_p I\phi_p^* \qquad (63)$$

where ϕ_P^* is the current value of ϕ_P. At the point of convergence, where no changes occur to ϕ_P over the iterations, the equation is not modified by the new terms. Just before convergence, there is a link between the new value ϕ_P and the current iteration value ϕ_P^*. The value of I gets stronger the larger this is. The term I is expressed as:

$$I = \frac{\rho\upsilon}{\Delta t_f a_P} \qquad (64)$$

where Δt_f is a false time step, if I is equal to 1.0, then Δt_f is analogous to the maximum time step suitable in an explicit time-marching solution scheme. CFD-ACE+ implements solution with an implicit solution, it is impossible to use larger Δt_f , generally, a range of $0.2 \le \Delta t_f \le 0.8$ is used. Auxiliary variables can be under-relaxed by specifying a linear under-relaxation factor, λ , applied thus:

$$\Theta^{new} = \lambda\Theta + \left(1+\lambda\right)\Theta^{*} \tag{65}$$

where Θ^{new} is the updated value of the variable, Θ is the value of the variable as calculated with no under-relaxation and Θ^{*} is the current iteration value of the auxiliary variable.

For this work being an implicit problem (with coupled set of equations), an inertial relaxation factor of 0.2 was used for the velocity and 0.0001 for the electric potential. The density, pressure and viscosity were kept with a linear relaxation factor of 1 and the solution converges under these sets of parameters.

5.3.3 Linear Equation Solvers

For each unknown variable, a set of linear equations is generated during the discretization process. Each of these discrete values corresponds to the value assigned to the centroid of a cell in the grid of a FVM computational cell. Thus each cell gives a set of linear equation in the form of Equation (63) that relates its discrete value to that of the neighbouring cells and that of both the sink and source terms for the cell.

The assembly of n (total number of cells in the grid) linear simultaneous equations is expressed in form of standard matrix equation:

$$A\phi = K \tag{66}$$

where A is the matrix of coefficients, ϕ is the vector of the unknown discrete value (i.e. the unknown cell-centred values), and K represents the vector forcing-function elements. These three elements can be inferred from equation (63) and the subsequently assembled linear system is solved or inverted to obtain the values of discrete unknowns at the said centres.

The overall solution quality and time are dependent on the choice of method used to solve the assembled system of equations. The system of equations from (66) can either be solved using a **direct** or an **iterative** type of solver. The latter are favoured for large sparse systems because they are faster and are less memory expensive than direct solvers. CFD-ACE+ provides six options to choose from either Algebraic Multigrid (AMG), Aggregation AMG, Smoothed Aggregation AMG, Conjugate Gradient Squared (CGS), Generalized Minimum Residual (GMRES) or Generalized Bi-Conjugate Gradient Stabilized (BI-CGSTAB(L)) solvers

By default, CFD-ACE+ uses Aggregation AMG solver for pressure correction and uses CGS solver preconditioned with incomplete LU factorization for other variables. The preconditioner helps in speeding up the solution of the equation system. The goal is to find the least expensive solver and a preconditioner that can improve solution within the least number of iterations.

For this work, the AMG has been used as the linear solver for all the variables. The AMG does not require a preconditioner. It has the advantage of speeding up a solution of iterative technique by reducing the number of iteration necessary for convergence.

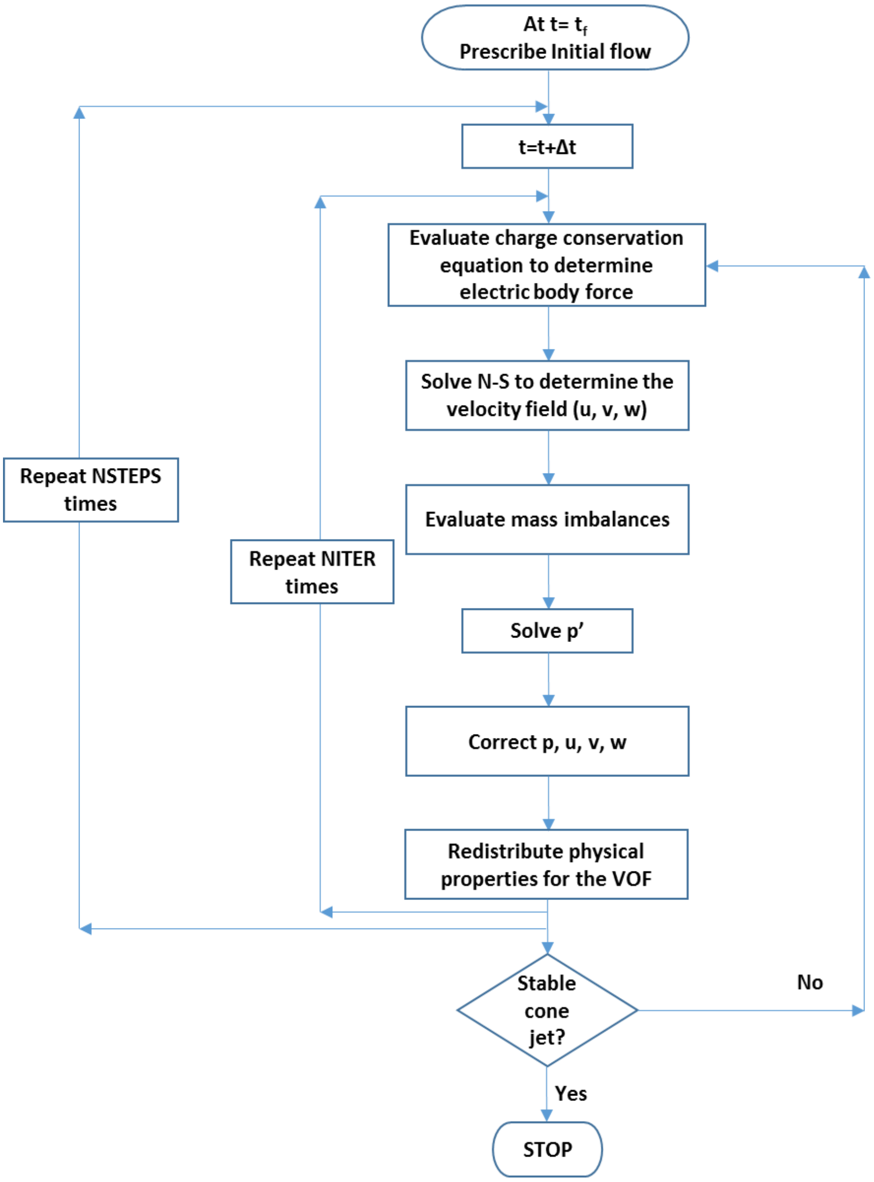

Figure 5.9- Solution Flowchart (adapted from [93]*)*

5.4 Time Stepping

An automatic time stepping approach has been used for the computation, with the minimum time step for the axisymmetric simulation set at $1.0\times10^{-9}s$ while the maximum time step was kept at $0.01s$. In total the simulation runs for $0.2s$, starting at an initial time step of $1.0\times10^{-7}s$ and to enhance convergence and stability the target CFL was taken as 0.1.

6. MODEL SET UP, INITIAL CONDITIONS AND BOUNDARY CONDITIONS.

6.1 Model Setup

This section discusses the technique employed in the simulation of the electrospinning process. To solve the multiphase problem, a finite volume based CFD package, CFD-ACE+ (ESI Group, Paris, France) was used for the investigation. The axisymmetric geometry was built with CFD-GEOM, the EHD equations were solved with CFD-ACE+ and the post-processing was done on the CFD-VIEW platform.

Water, being the liquid phase for the model is described by the following properties: density of 1000kgm^{-3}, the dynamic viscosity of 8.9 x 10^{-4} m^{2}s^{-1}, the surface tension of 0.075Nm^{-1}, dielectric constant of 78, electrical conductivity of 5.5 x 10^{-7} Sm^{-1}. While air is the gaseous state with a density of 1.1614kgm^{-3}, kinematic viscosity of 1.589 x 10^{-5} m^{2}s^{-1}, dielectric constant of 1, electrical conductivity of 5.0 x 10^{-15} Sm^{-1}.

6.2 Model Geometry

The emitter, in reality, is a needle with flat tip, set at a distance to the target/collector. The setup is not enclosed into a chamber but free to the atmosphere. The horizontal arrangement is preferred for this modelling. The jetting is produced by infusing the leaky-dielectric liquid at a constant volumetric flow rate and applying a voltage (from a DC source) at on the wall of the needle while the target is kept at zero. For this case, the leaky-dielectric fluid used is water.

6.2.1 Geometry

An axisymmetric geometry was generated based on the set up in Figure 6.1. The configuration has been adequately modelled with the zone of interest represented as seen in Figure 6.2. Showing the Needle/emitter containing the liquid phase and the bounded space representing the atmospheric air as the gaseous phase. The wall of the emitter is modelled as a solid to enable the application of electric voltage on the emitter. A constant voltage in a range of $4-25KV$ is applied on the emitter wall. The collector is modelled as a wall with zero voltage.

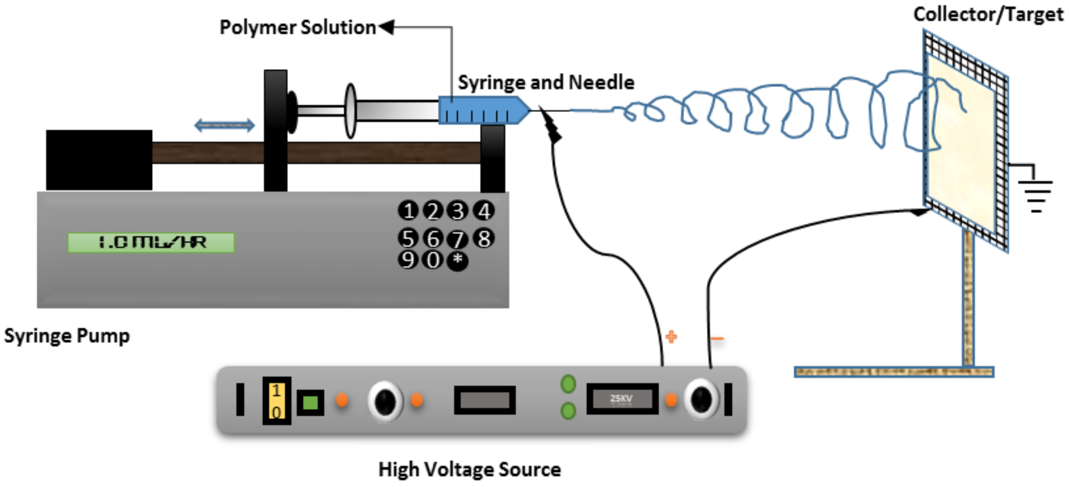

Figure 6.1: Diagrammatic Representation of EHD set up as modelled in the current work.

Figure 6.2- Axisymmetric CFD Computational Domain

The axisymmetric model is subdivided into three zones as seen in Figure 6.2, each zone representing the liquid phase, gaseous phase and solid phase (thickness of the needle/capillary) and it is also split into six different volumes (with the liquid zone divided into four volumes), to enhance mesh refinement and optimization around the region of interest.

6.2.2 Boundary Conditions and Initial Conditions

Table 6.1 shows a summary of the boundary conditions (BC) implemented for the simulation. The BCs are divided into electrostatic and hydrodynamic conditions. Neumann conditions were used on the symmetry boundaries and Dirichlet conditions (fixed boundary condition) were used on the remaining boundaries. The computational domain for the simulation can be seen in Figure 6.2. The BCs are needed to solve the EHD equations, these conditions are imposed at the outer limits of the computational domain and at the solid (needle) interface.

Table 6.1- Summary of Boundary Conditions for the computation.

	Boundary Condition	**Electrostatic (V)**	**Hydrodynamics**	**VOF (Fraction)**	**Distance (mm)**
AB	Inlet	Φ=0	$V = 0.01$m/s	Fluid 2= 1	0.25
BD	Wall	$\Phi=\Phi_O$= 25,000	$P = 0;\ V = 0$	Partial Wetting	2.00
DC	Interface	-	-	-	0.20
AE	Symmetry	Dirichlet conditions			10.0
GH	Outlet	Φ=0	$P = 0$	Fluid 1= 0	2.20
GF	Outlet	Φ=0	$P = 0$	Fluid 1= 0	9.00
EF	Wall	Φ=0	$P = 0;\ V = 0$	Fluid 1= 0	2.50

Inlet Boundary Conditions

At the inlet, a fixed velocity condition is set in the x-direction. A reference to an atmospheric pressure of $100 KN/m$ is made, which however does not affect the computation, since all pressures are referred to the fixed outlet pressure (see next section). The fractions of the primary and secondary fluid are set at the inlet is set at 0 and 1 respectively and a zero voltage is applied at the inlet.

Outlet Boundary Conditions

The fixed pressure boundary condition is selected at the outlets of the geometry, this allows to set the pressure and other variables are calculated by the solver**.** Here the electric potential and the pressure are set at 0. The backflow temperature is kept constant at $300K$.

Wall Boundary Conditions

This condition allows the specification of the velocities on the wall. For this work, no-slip, no-flux conditions are imposed (i.e. zero velocity on the wall). The imposed BC is expressed thus:

$$\vec{V}_f = \vec{V}_w \tag{67}$$

where $\vec{V}_f$ and $\vec{V}_w$ are the velocity vector of the fluid and the wall. For a stationary wall like in the work, $U = V = 0$. This means the fluid in contact with the wall has a zero velocity.

The needle thickness (BD) and substrate target (EF) as shown in Figure 6.2 are modelled as walls and the no-slip boundary condition applied. An electric potential is applied on the needle wall, while a zero potential is applied on the target substrate. A partial wetting of magnitude $20°$ contact angle is set on the needle wall, while full wetting (i.e. a contact angel of $0°$) is set on the target.

Interface and Symmetry Boundary Conditions

At the symmetry, a zero-gradient condition is set, there is no flow allowed across the symmetry. Just like the symmetry, for the interface boundary condition, there is no value for the hydrodynamic, volume of fluid and electrostatic parameters. At the interface between the gas (air) and liquid (solution), there exists a coupling between the hydrodynamic and electrodynamic charge accumulation on the transient interface. This interface is continually changing to stabilize under the influences of the fluid properties, pressure and accumulation of the charges at the dynamic surface of the liquid.

Initial Conditions

The initial liquid geometry is a flat surface at the rim of the needle. Subsequently, during the computational iterations, the shape is gradually transformed into a conical shape, which eventually leads to a jet break-up.

For this work, the gaseous zone, bounded by *CEFGHD* as shown in Figure 6.2 is assumed to be initially filled with the primary fluid 1, with a fluid fraction of 1 and all the parameters (velocities, pressure, electric potential) are assumed to be at zero value. The liquid zone, bounded by *ABCD* in Figure 6.2 is assumed to be filled with the secondary fluid 2, at the fluid fraction of 1. Likewise, all the parameters are set at zero.

The results of the simulations conducted and the observed flow patterns are reported here. The cases give an insight into the effect of the electric field on the fluid flow and consequently the distortion. More generally, the model provides an understanding of factors that cannot be observed or measured experimentally. Also, reported here are the results obtained until now on the various cases, including the current model which accounts for the axisymmetric jetting and dripping mode, but not the 3D behaviour which explains the whipping and multiple jetting modes. These would be accounted for in the next phase of the project.

6.3 MODELS

To investigate the process, different models/configuration were used, until a final one was deemed appropriate. This section will take a quick review on the models, highlighting the geometry, observation and reasons for modification.

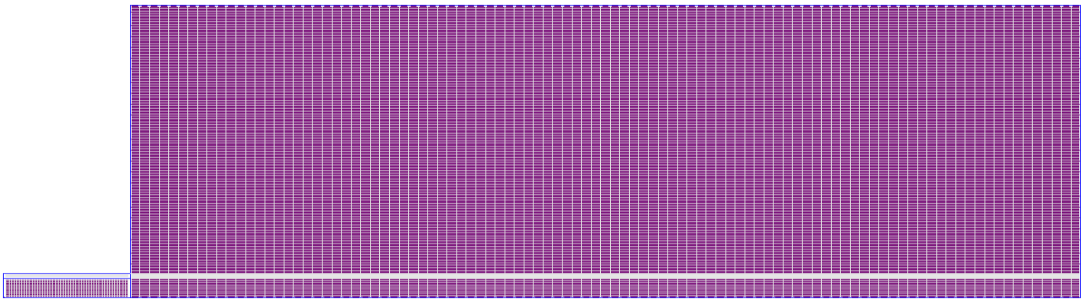

Figure 6.3- Model A

Model A: Figure 6.3 shows a geometry with the boundary of the fluid 1 terminating at the edge of the fluid 2 volume and the needle thickness included as well. A structured mesh was used with a total of 12,465 cells. The simulation could not capture the effect of the applied voltage on the flow, therefore there was a need to extend the left boundary for fluid 1 to the wall.

Model B: Here, the left boundary of the fluid 1 is extended throughout the whole length of the needle (i.e. to the beginning of the fluid 2 zone) as seen in Figure 6.4 Also, the needle thickness was not included in the geometry, the boundary was merely defined as a wall. Unstructured mesh was used and with a total of 50,992 cells. Overall, the effect of the applied voltage was observed in the simulation (as shown in Figure 6.5) but the VOF interface tracking was poorly captured by the unstructured mesh (a well-known deficiency of such grids).

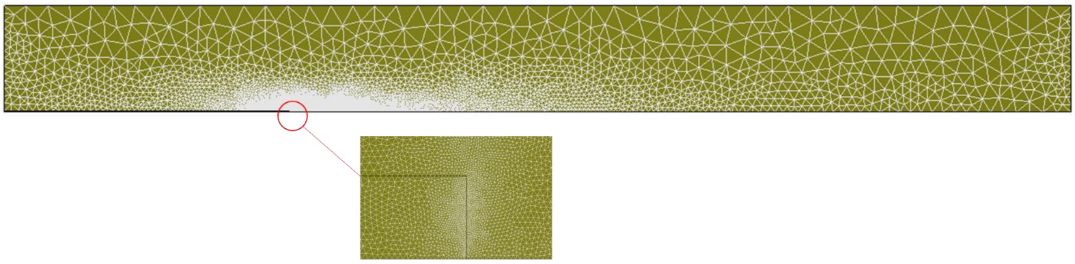

Figure 6.4- Model B

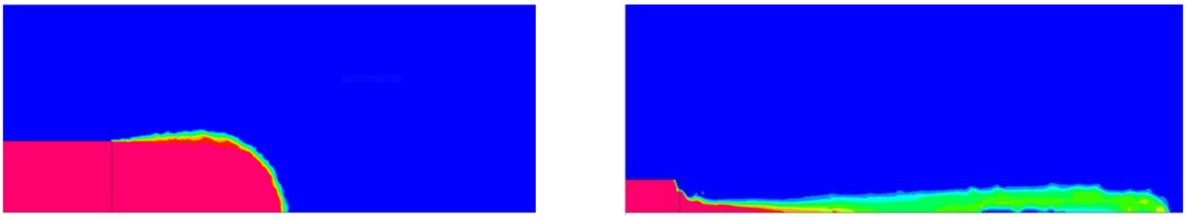

Figure 6.5- Model B without and with the influence of an electric field.

Model C and D: These utilize structured meshes and the only difference lies in that for model C, the zone containing fluid 1 extends for the whole length of the needle, whereas for model D, the zone only extends to halfway- this saves some computation time for the simulation by excluding a zone that is practically inactive. This report is based on simulations ran with model D. They are shown in Figure 6.6.

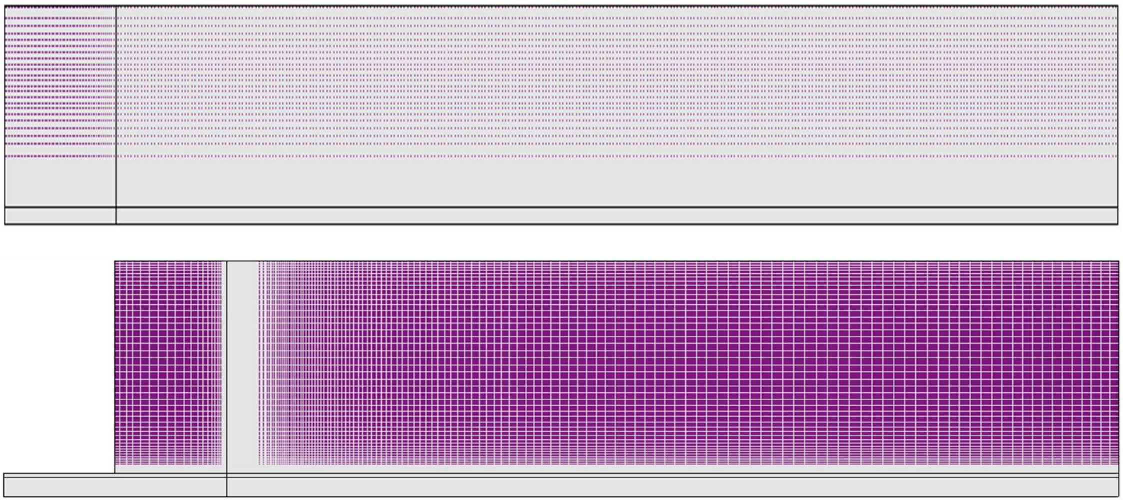

Figure 6.6- Mesh and Configuration of Model C (top model) and D (bottom model)

6.4 Model Description and Computational Domain Parameters

The model was modelled and meshed on CFD GEOM, with 24 boundaries, 6 volumes and 3 zones (representing the two phases and the block-needle thickness). For the axisymmetric model, approximately 75k cells- all with structured cells- were used. Computational dimensions were within X (0,10) mm and Y (0,2.5) mm.

The method is capable of handling 2D, axisymmetric and 3D geometries if appropriate meshing can be constructed. As an example, for an axisymmetric model with a charged needle, generating fibres, approximately 50-300K cells - all with structured conforming cells were used. An illustration of this mesh topology is shown as an example in Figure 6.7. Three-dimensional computations necessitate meshes of approximate 3-7M elements to obtain solutions of similar resolution and mesh independence characteristics.

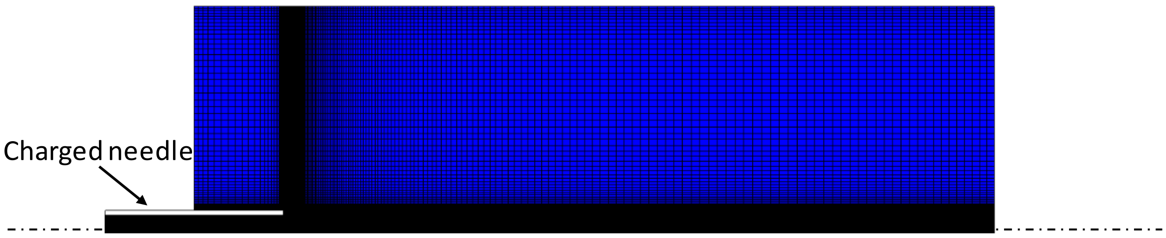

Figure 6.7- Axisymmetric Finite Volume Mesh Model

The mesh across the expected region for the flow development/free surface VOF tracking has been made as uniform and as refined as possible; this is to ensure accurate tracking and enhance the jet definition.

No initial assumption was made for the charge distribution or liquid shape. The effects of the electric field on the VOF distribution, velocity magnitude, charge distribution and electric potential distribution are discussed among many other evaluations. Several simulation runs were carried out at various combinations of flow rate and electric voltage. The coming chapters highlight these effects.

6.5 Grid Independence Study

The flow characteristics were found to keep changing as the mesh sizes change, hence the need to optimize the grid structure. As earlier stated, the structured grid system has been adopted (but in non-uniform discretization in the domain), so that the finest mesh is near the capillary. Six mesh sizes were used, with minimum cell sizes of 2, 4, 5, 8,10 and 12 µm. All the test simulations were carried out at flow rate of 5 millilitres/seconds and voltage of 4KV magnitude on the capillary walls. The plot of the maximum magnitude of electric filed strength against the minimum cell size in the computational domain has been used to represent this trend, as shown in Figure 6.8. To save computational cost, a mesh structure with 8 µm was used for subsequent simulations. For this selected mesh, a total of approximately 75,000 grids were used.

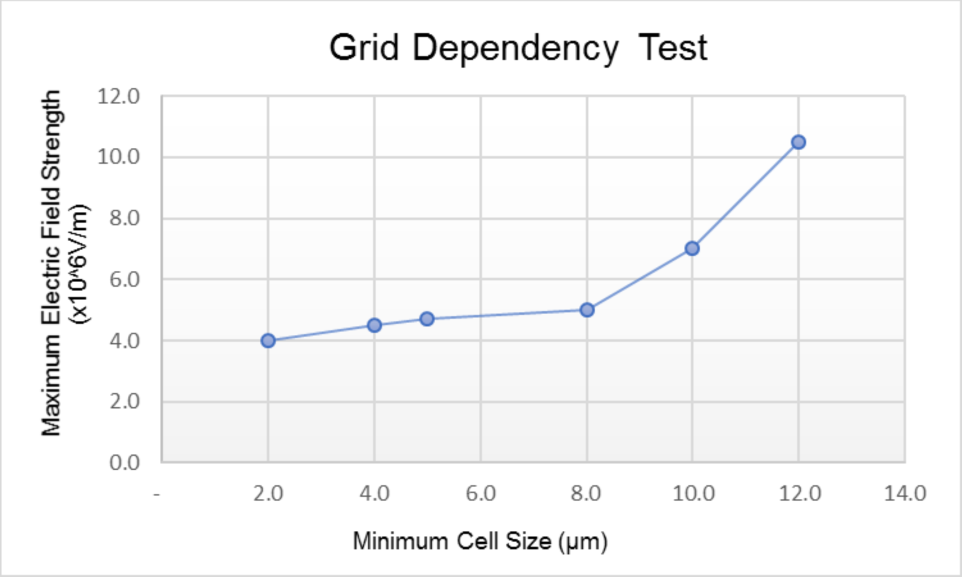

Figure 6.8- Grid dependency test, showing a plot of the maximum magnitude of electric filed strength against the minimum cell size in the computational domain.

6.6 Model Validation

To check the accuracy of this model the mean diameter obtained at flow rates of magnitudes $1.67, 3.33, 5.00$ and $6.67\,\mu l/s$ has been measured and compared with experimental results from Noymer and Garel [79]. As seen in Figure 6.9, the same trend was observed but with a slight difference in the magnitude of the mean diameter, this might be because the inner capillary diameter for this work is $500\mu m$ and for the experimental work by Noymer and Garel, the nozzle diameter was $890\mu m$ at an applied voltage of $8.1kV$. This further proves that the nozzle diameter affects the emerging droplets. There is a geometric similarity in the deformation of the meniscus as well.

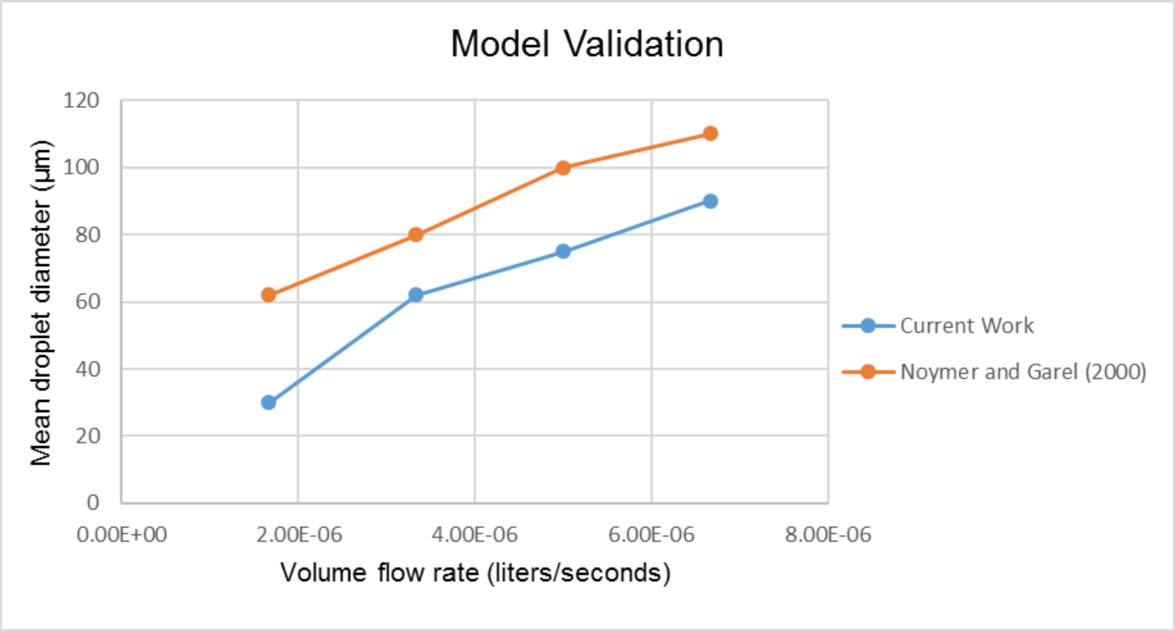

Figure 6.9- Comparison of mean droplet diameter at various flow rates of 1.67E-06, 3.33E-06, 5.00E-06 and 6.67E-06 litres/seconds when an applied potential of 8.1kV imposed on the capillary wall; obtained from the current work and experimental work by Noymer and Garel [79].

7. TAYLOR CONE-JET FORMATION

This is a base case that forms a common platform for comparisons and for establishing that the balance of viscous, surface tension, inertial, pressure and electrostatic forces indeed accounts for all phenomena in a realistic manner.

7.1 Fluid Flow Characteristics

Under the influence of an applied voltage of magnitude 10kV, the liquid experiences a 4-staged transformation from the initial liquid deformation to the Taylor cone formation to the jetting mode and finally a droplet breakup phase. Initially, the liquid-air interface is flat and as the flow advances, it is deformed due to the interaction of the hydrodynamic and electric forces. The surface tension in the fluid is gradually being overcome by the dielectric force.

After the electric field is applied, the drop liquid deforms into a spherical shape due to EHD liquid flows induced by the charge build-up on the drop surface. Right after the electric field polarity is inverted, the drop rapidly deforms and becomes conical and the first jet was seen to emerge after 0.86 milliseconds (as seen in Figure 7.1).

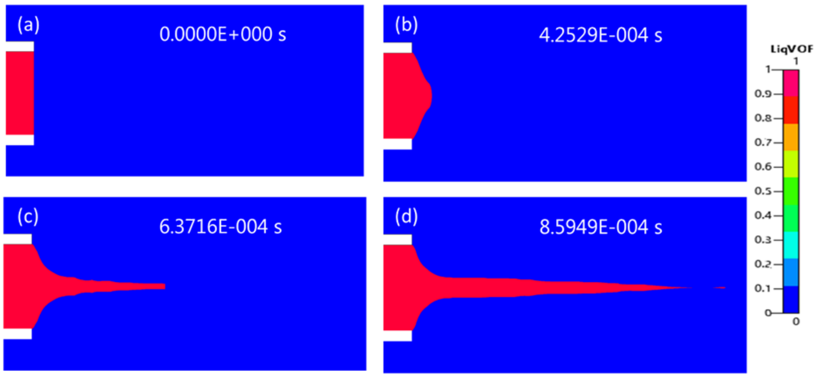

Figure 7.1- VoF flow distribution at 10kV and inlet flow rate of 7.1ml/hr. (a) t = 0s, (b) t = 0.43ms, (c) 0.64ms and (d) 0.86ms

7.2 Charge distribution and electric potential distribution

Under the influence of an applied electric field, free charges accumulate at the interface, which induces droplet deformation and EHD flows inside and outside the needle. As expected for a dielectric fluid, the electric charges were mainly localized at the surface of the secondary fluid and very low charge/zero charge density was observed in the bulk of the fluid and of low magnitude in the air. Figure 7.2 shows the electric field distribution after 0.48 milliseconds when an electric potential of 10kV is applied to the walls of the needle. The Electric field and Electric Potential distribution were shown to evolve, as expected, as the fluid flow advances.

The electric field accounts for both the tangential and normal electric stresses. While the former maintains the conical shape, the latter accelerates the liquid in the direction of the jet.

The applied electric potential induces surface charges on the periphery and not inside the bulk of the fluid jet, and this phenomenon can be seen in the electric field distribution, Figure 7.2.

Taylor and Melcher [19], [55] argued that the surface charges were adequately balanced by the surface tension of the bulk so that a dynamically stable condition is achieved. They noted that the consequence of this interaction is an elongated shape of the fluid volume. This distortion results in the formation of the well-established Taylor cone. The size of this cone is affected by parameters including fluid properties, electric potential and flow rate of the fluid [6], [52], [84].

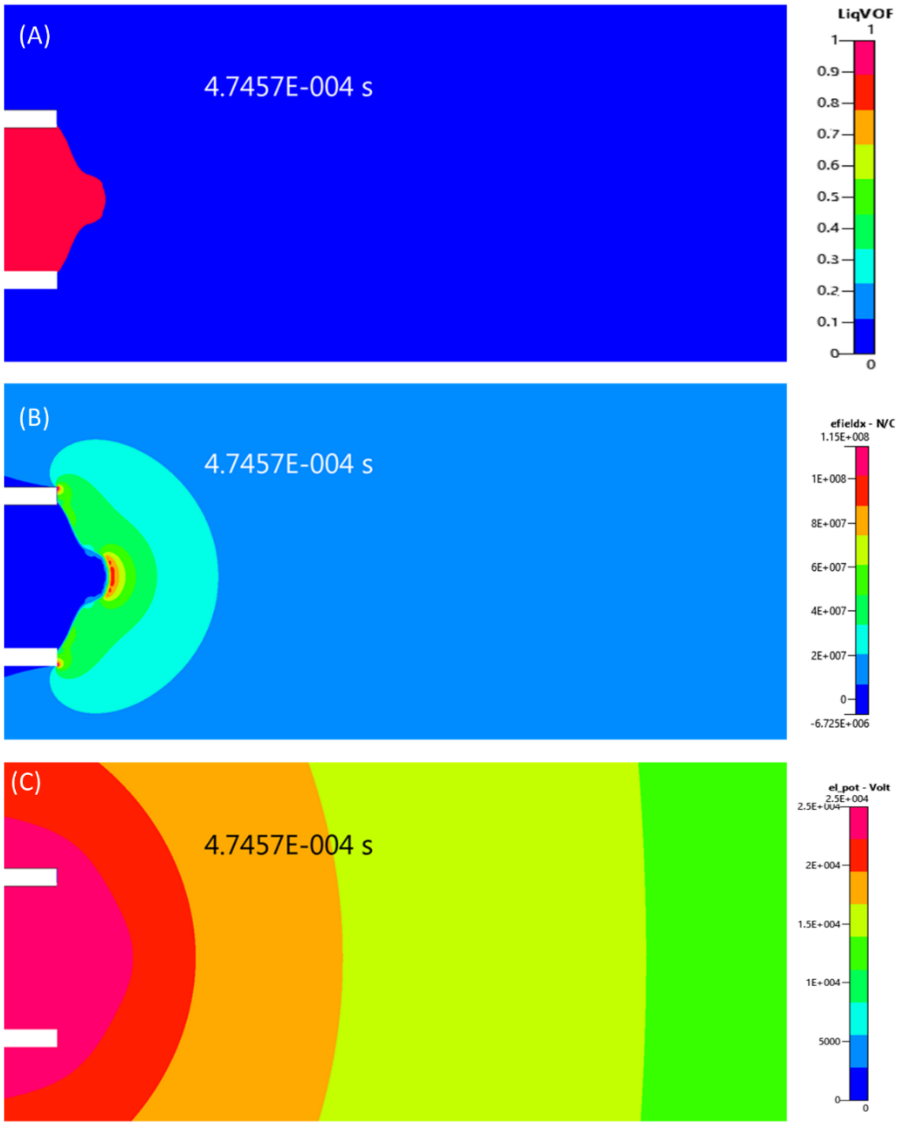

Figure 7.2- (A) VoF distribution, (B) Electric Field distribution and (C) Electric Potential distribution, at 0.48 milliseconds.

The results obtained to investigate the fluid front interaction with the dynamic electric field also showed good agreement with the work of Sarkar et al [83]. This is a feature that is extremely difficult to visualise experimentally. Figure 7.3 shows a sample of such results from the present study.

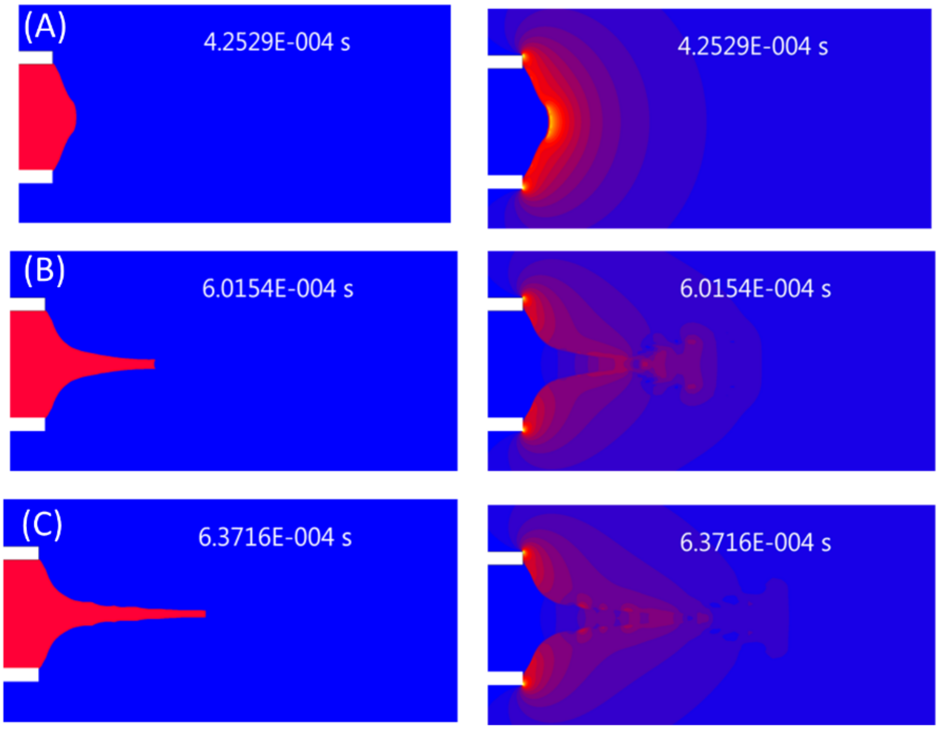

Figure 7.3- Fluid fronts (left pane) and electric field magnitudes (right pane) at equivalent time steps, showing the interaction of the two flow characteristics. (A) t = 0.42ms, (B) t = 0.60ms and (C) t= 0.64ms

This result implies that the electromagnetic properties (like fluid permittivity, permeability and conductivity) of the fluid can be used to control the fluid front and flow patterns and therefore the EHD cone-jetting mode and other EHD features. The effects of how the permittivity and solution conductivity alter the EHD flow is reported in a later chapter of this report.

7.3 Velocity Magnitude

The velocity field, as shown in Figure 7.4c, gives a consistent pattern of toroidally-shaped vortex as reported in [82]. The liquid moving in the direction of the main flow is divided by this vortex. This phenomenon of division causes the majority of the liquid to be drawn back into the centre vortex, recirculated and mixed with the main flow, while the remaining liquid is drawn into the jet [82], [100]. To predict the effects that are likely to influence the production and features of jets, the knowledge of flow patterns inside liquid menisci will be useful. Predominantly, it is important to know the role of charge convection to predict characteristics like charge and droplet size [100].

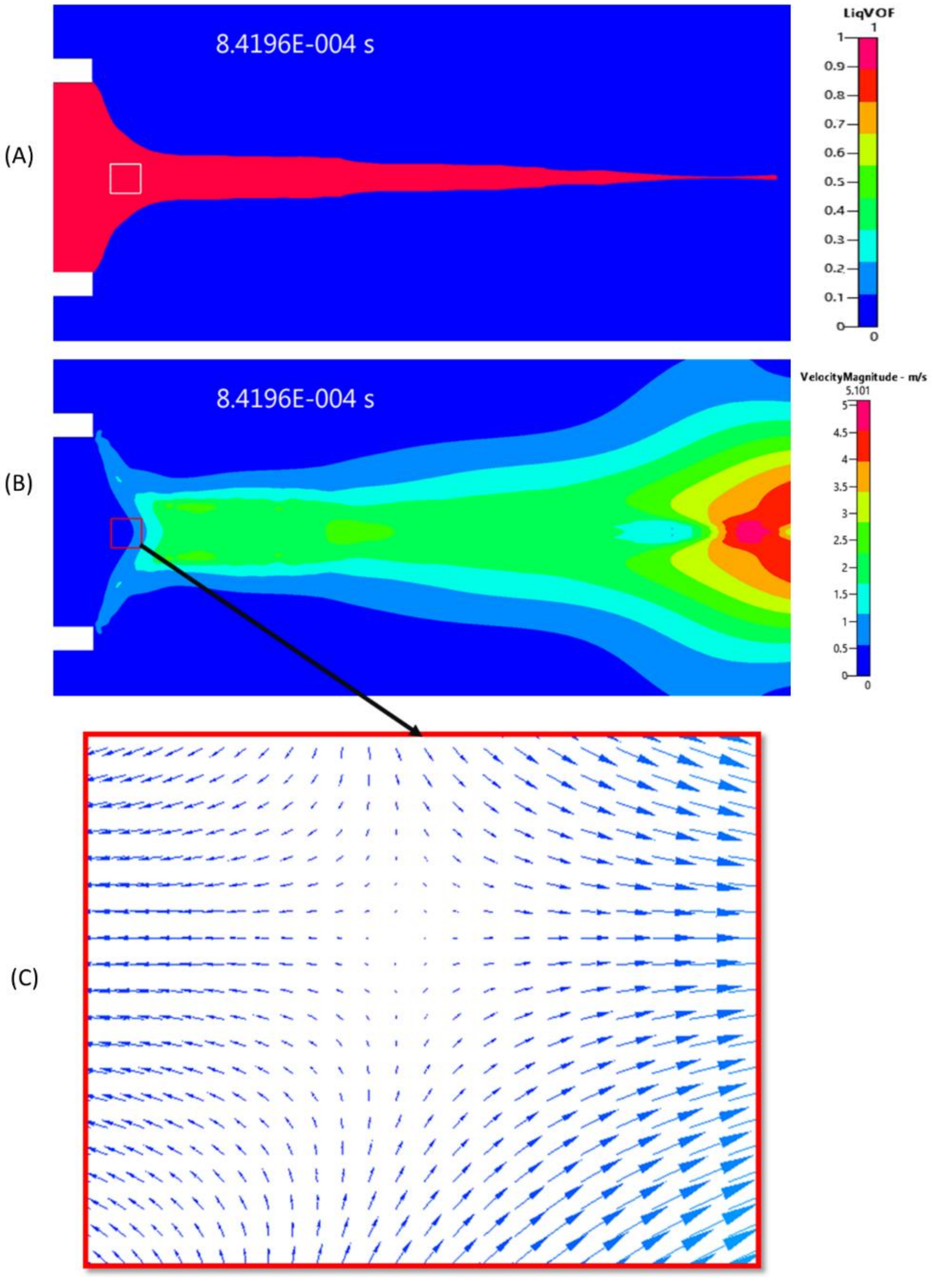

Figure 7.4- (a)VoF, (b) Velocity magnitude distribution and (c) Velocity field (corresponding to inset square) at 0.84ms

7.4 Development of Taylor Cone, Jet and Droplet

The droplet development stages are as shown from Figure 7.5 to Figure 7.9 with the droplet emerging at about 0.86milliseconds when an electric potential of $10kV$ is applied on the wall of the needle at an initial inlet velocity of $0.01ms^{-1}$ (flow rate corresponding to $1.8 ml/hr$). The corresponding electric field, electric potential and velocity field along the flow direction are shown alongside with the VOF distribution. The electric field accounts for both the tangential and normal electric stresses. While the former maintains the conical shape, the latter accelerates the liquid in the direction of the jet.

From Figure 7.5, no initial deformation was assumed. The capillary was initiated to be filled with the liquid and there is no initial charging of the space. As the electric field develops and overcomes the surface tension at the air/liquid interface, the interface begins to deform into a hemispherical shape and there is a fast jump in the fluid velocity to about $4 m/s$ after about 0.14 milliseconds. The electric field was found to be maximum at the tip of the fluid interface and with a magnitude of $26.5 MV/m$.

At approximately 0.37 milliseconds, the deformation of the drop meniscus takes a proper hemispherical shape (with the apex cone angle of $123°$) as the flow advances and after 0.43 milliseconds, it begins to transform into a convex conical shape, signalling the onset of the Taylor cone, at this stage, the cone angle is about $135°$ (as seen in Figure 7.6). At this stage the electrical stresses are fast overcoming the viscous stresses in the solution, hence stretching it in the direction of the field.

From Figure 7.7, it can be seen than the Taylor cone is now fully developed after 0.60ms, with the apex cone angle of $83°$, hence the half-angle (which relates to the Taylor cone angle) is given as $48.5°$, this angle is well in agreement with that of Taylor [19], [75], who places this angle at $49.3°$. As quoted by Saville, “The balance between electrical stress and interfacial tension determines the cone angle, and the normal component of the viscous stress is zero. As required, the tangential electric stress along the periphery of the cone is balanced by viscous stress”. This explains the interrelationship in the electrohydrodynamic stresses as the Taylor cone is formed. Likewise, in Figure 7.7, after 0.64ms, the jet elongation is seen to continue and the jet thins out; just within 0.04 milliseconds, the jet increase by an extra 1.5 times more.

Furthermore, as the jet advances, at 0.84ms (Figure 7.8), the emerging jet reaches the pinch point- where the jet stream develops a “necking”, nearing the onset of the first jet detachment or break-up. After an extra 0.02 milliseconds, the first jet breakup occurs, and the jet pulsates to make the next discharge. From the right pane of Figure 7.9, the jet begins to retract into the capillary.

The applied electric potential induces surface charges on the periphery and not inside the bulk of the fluid jet, and this phenomenon can be seen in the electric field distributions of Figure 7.5 to Figure 7.9, also a typical plot of this distribution at a distance of 0.0015m beyond the needle tip is shown in Figure 7.10. Barrero et al [100] also noted that at the air/liquid interface, free charges are usually confined to a very thin layer.

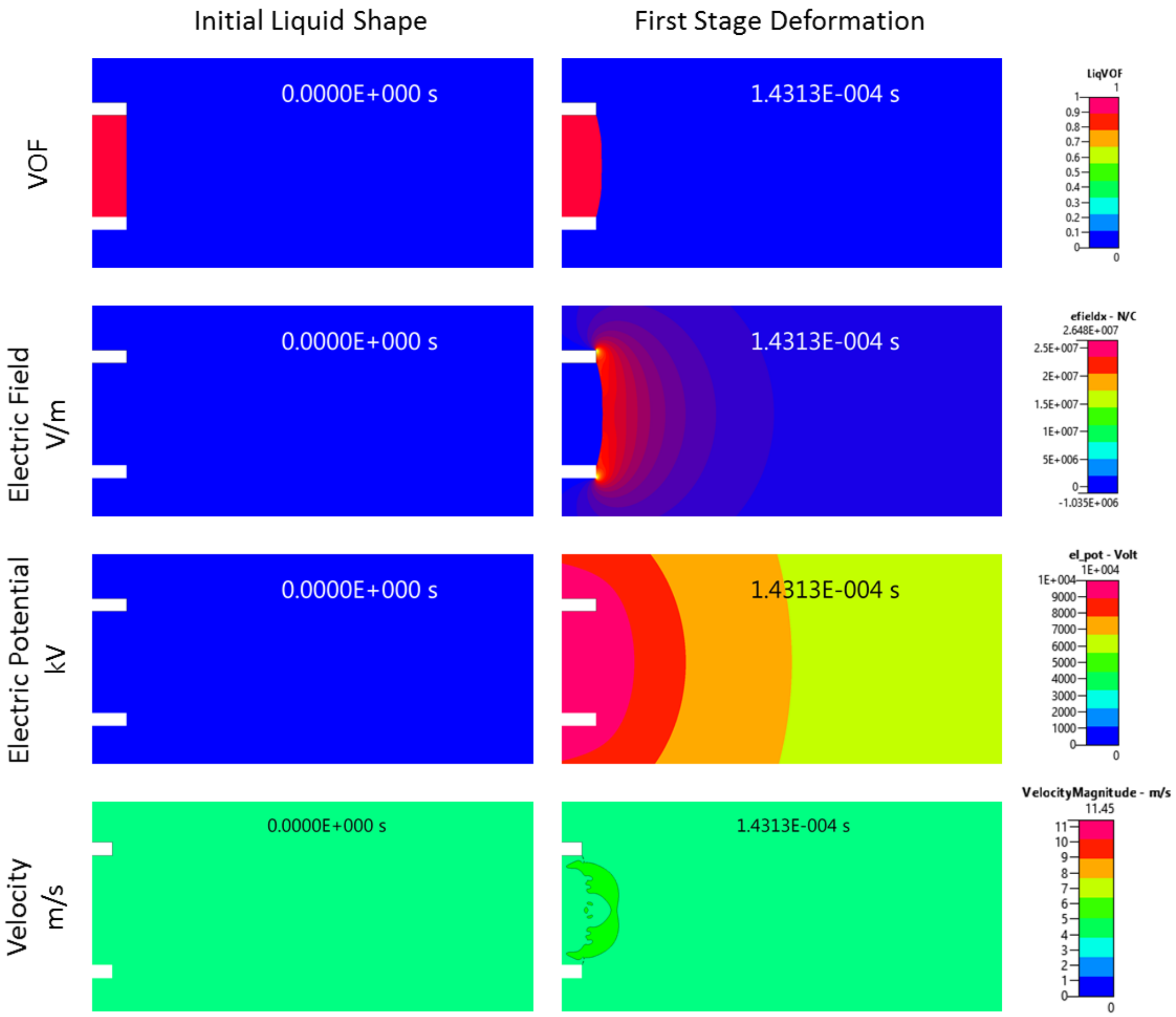

Figure 7.5 Plot of VoF, Electric Field, Electric Potential and Velocity distribution showing the flow characteristics at the initial stage and the first stage of flow deformation, occurring at 0s and 0.14ms

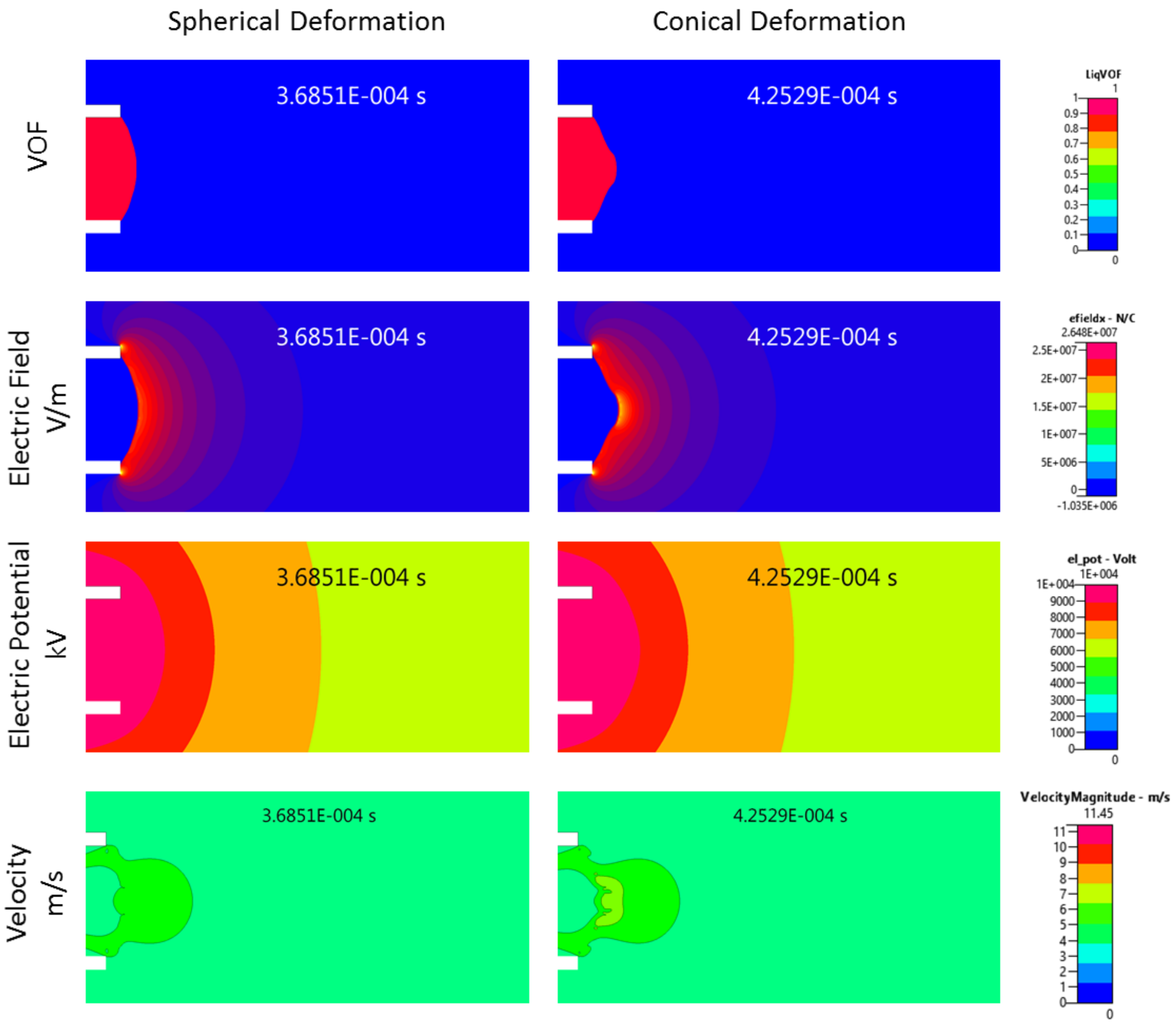

Figure 7.6- Plot of VoF, Electric Field, Electric Potential and Velocity distribution showing the flow characteristics reflecting the spherical and conical deformation stages, occurring at 0.37ms and 0.43ms

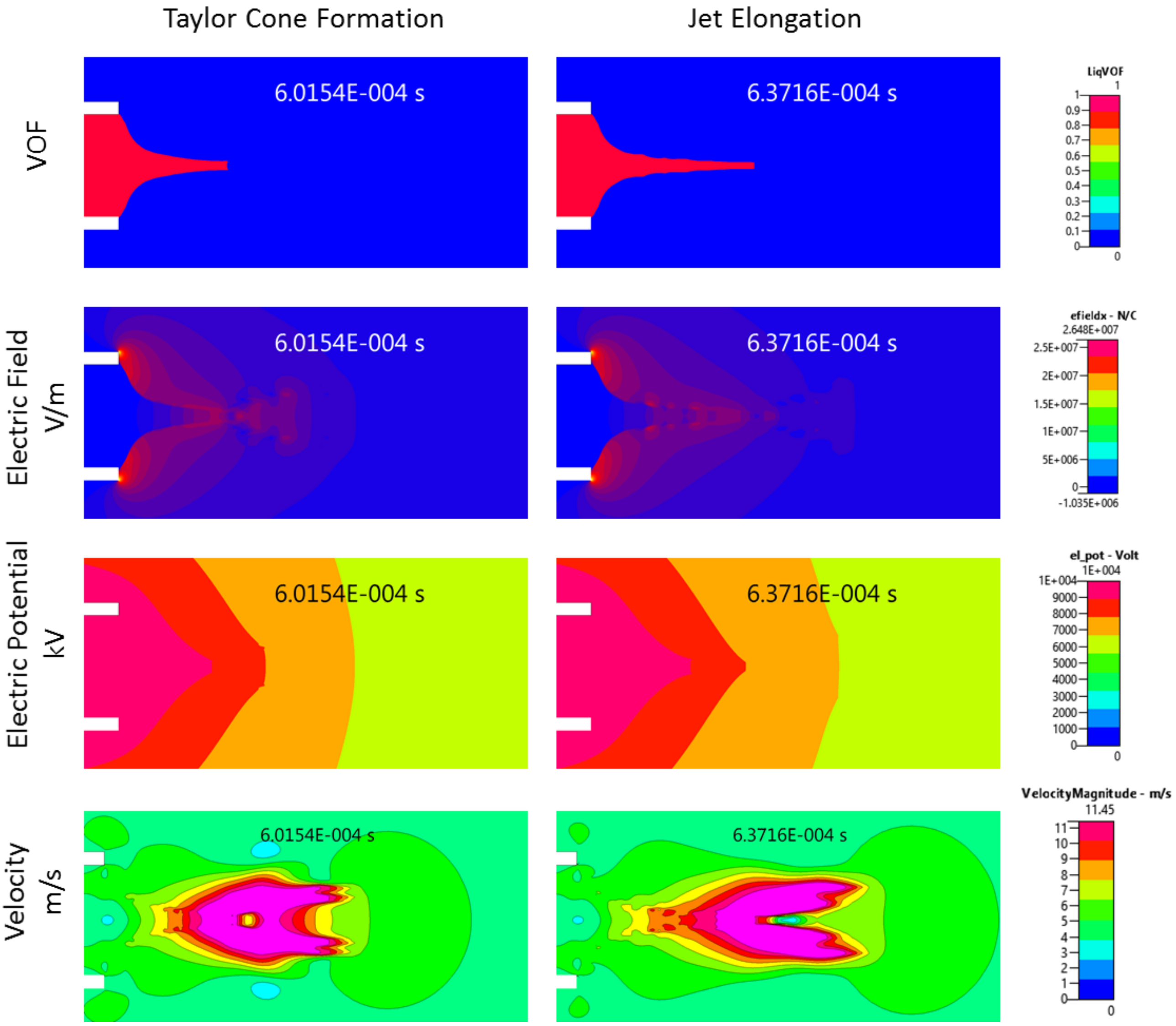

Figure 7.7- Plot of VoF, Electric Field, Electric Potential and Velocity distribution showing the flow characteristics depicting the Taylor cone formation and jet elongation, occurring at 0.60ms and 0.64ms

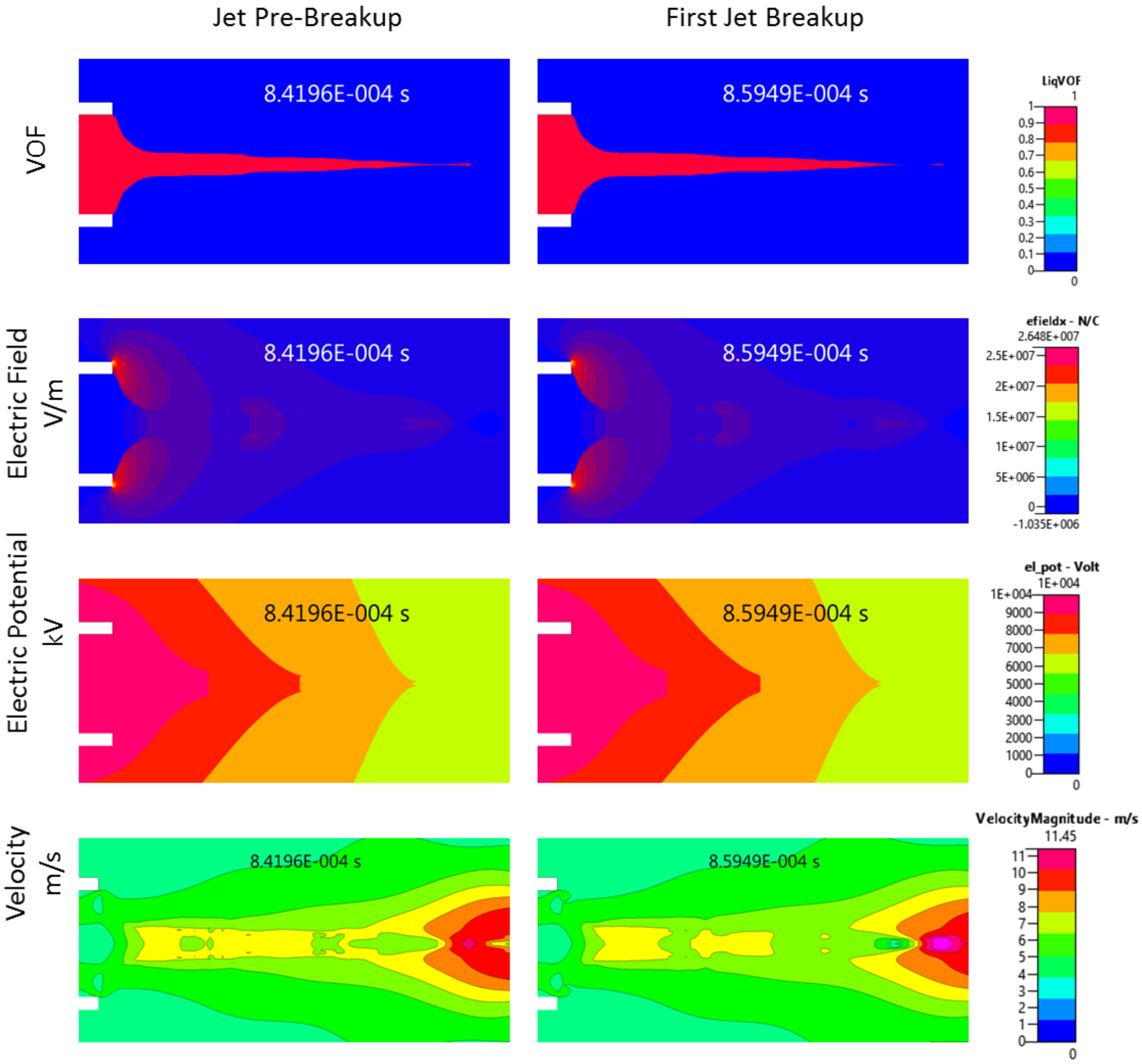

Figure 7.8- Plot of VoF, Electric Field, Electric Potential and Velocity distribution showing the flow characteristics just before the jet breaks up and after the first jet breakup, occurring at 0.84ms and 0.86ms

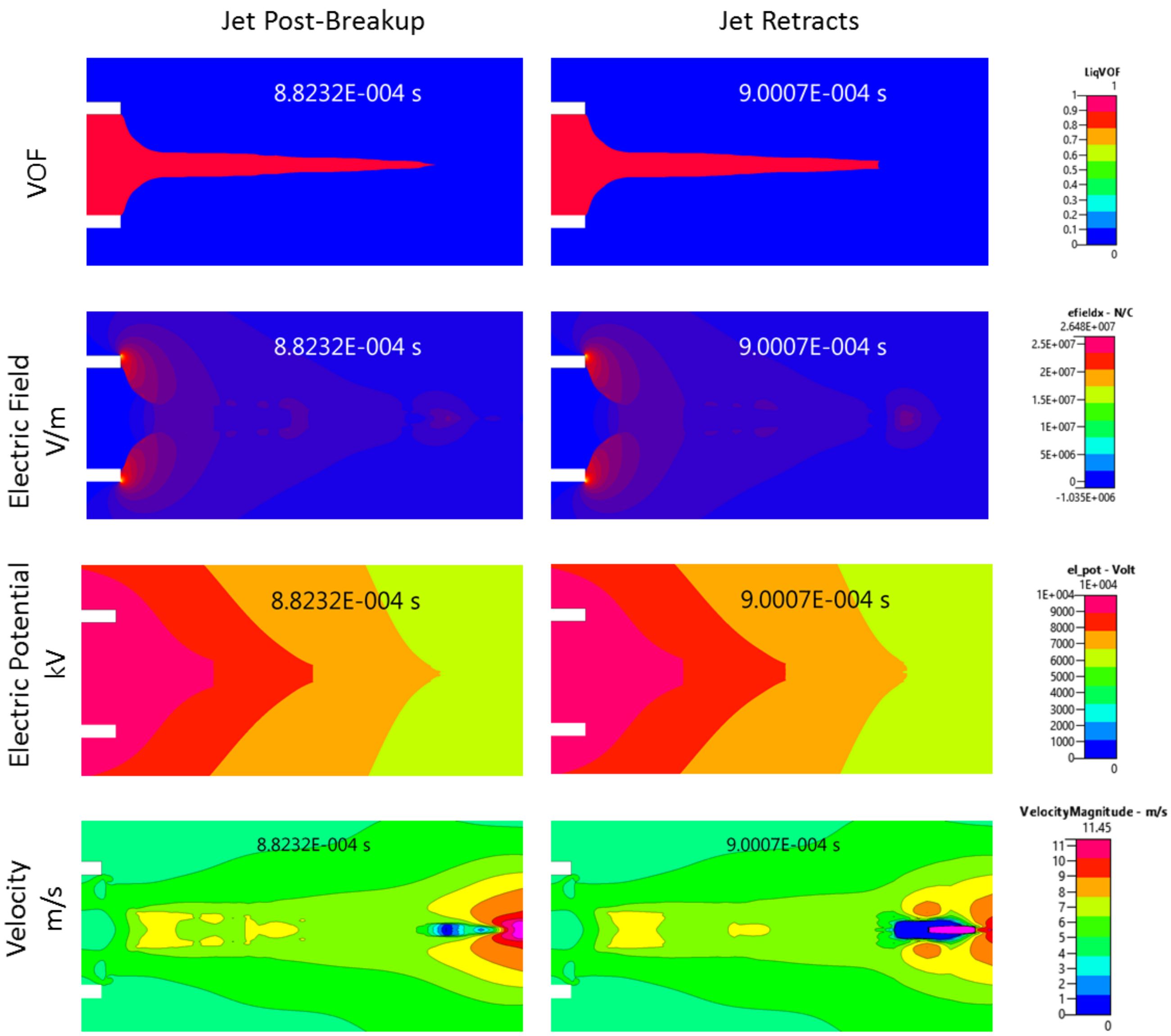

Figure 7.9- Plot of VoF, Electric Field, Electric Potential and Velocity distribution showing the flow characteristics after the jet breaks up and when it begins to retract back into the capillary, occurring at 0.88ms and 0.90ms

Taylor and Melcher [19], [55] argued that the surface charges were adequately balanced by the surface tension of the bulk which results in a dynamically stable condition. They noted that the consequence of this interaction is an elongated shape of the fluid droplet. This distortion results in the formation of the popular Taylor cone. The size of this cone is affected by parameters including fluid properties, electric potential and flow rate of the fluid [6], [52], [84] the effects of which will be measured quantitatively in the next phase of this work. Ultimately, this Taylor cone is developed from the application of electric field to a free-flowing dielectric liquid.

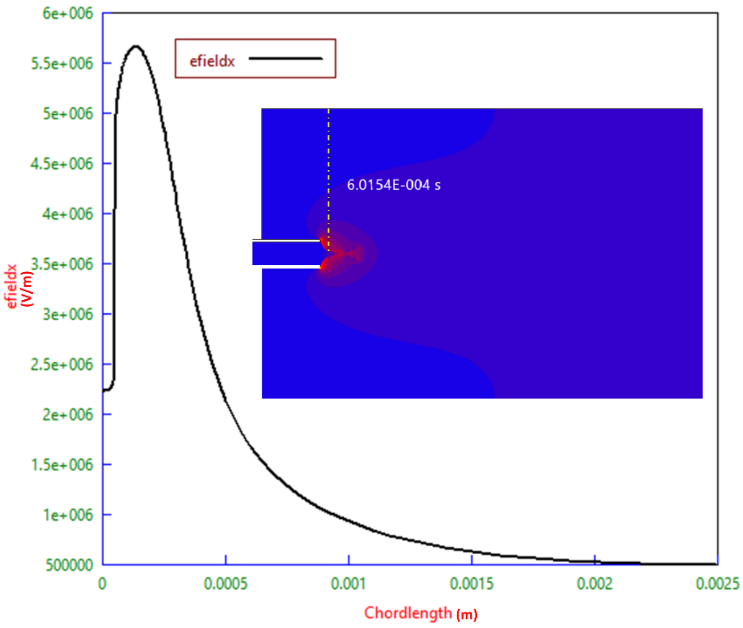

Figure 7.10 Electric Field distribution through the liquid bulk and interface at a distance of 0.0015m beyond the needle tip, showing that the applied electric potential induces surface charges on the periphery and not inside the bulk of the fluid jet.

Also, as seen in Figure 7.5 to Figure 7.9, the air-liquid interface (where the coupling between the electric and hydrodynamic forces takes place) was observed to be continuously changing to stabilize under the effects of pressure, fluid flow characteristics, and charge accumulation of the dynamic liquid surface.

The simulation allowed the development of the Taylor cone in a few milliseconds (about 0.60ms) and the droplet was also observed to emerge and detach from the main jet at about 0.84ms while the jet retracts back into the fluid flow (after 0.88ms), for the next cycle of droplet pulse. A typical process should involve a stable Taylor cone followed quickly by a stable jet.

It was observed that electric field moved along with the moving fluid, a phenomenon that is not observed experimentally, the consequence of this is that there is a strong interaction between the charged dielectric fluid and applied electric potential on the wall. Therefore, altering the electric field has the potential to control the fluid front and hence the jetting.

A similar trend was observed in the work of Wu et al [86] as shown Figure 7.11 is where a dripping mode was predicted at a lower voltage of 900V and a jet break-up mode was predicted at a higher voltage of 1400V. This further strengthens the assertion that the flow transition obtained in an EHD process is dependent on the selected operational map. This implies the model is capable of predicting the flow characteristics from a set of flow parameters.

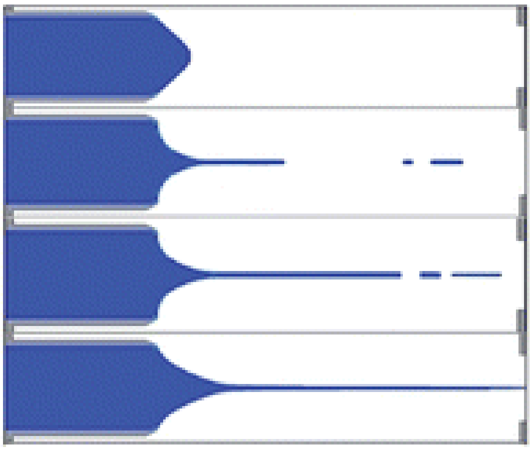

Figure 7.11- Jet-Breakup mode at various time steps [86].

8. JETTING MODE OF THE EHD PROCESS (EHDJ)

This chapter summarises one of the electrohydrodynamic modes at occurs when there is a superimposing of a weak electric field on a fluid flowing at a higher rate or velocity (in this case, the velocity is of 1m/s magnitude). This mode corresponds to a zone where there is a combination of high flow rate and low applied voltage mode in Figure 8.1. For this research, *EHD Jetting* (EHDJ) at a flow rate of $0.07 l/hr$ and applied voltage of $2.5kV$ was evaluated. This mode (EHDJ) is also referred to as electrospray, with several applications in physical and life sciences [101].

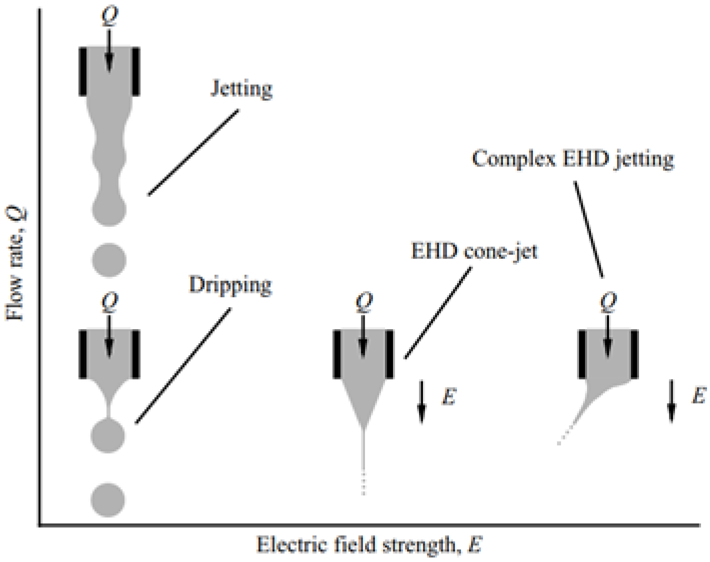

Figure 8.1- Phase diagram depicting flow transitions that occur as flow rate and/or electric field vary [102].

8.1 Droplet Development

It was observed that at lower electric field strengths and higher flow rates, the liquid exhibits a mix of jetting and dripping mode- result consistent to reports from Wu et al [86]. There is an absence of a strong electric force to overcome the surface tension of the fluid, the cone, therefore, adopts a round shape and deforms outside the capillary. The jets erupt at intervals to lower the surface energy of the developing cone. As the electric field overcomes the surface tension of the fluid, the droplet deforms from an oblate shape into a prolate shape. The flow profile at certain instances has been plotted in Figure 8.2 (a)-(l).

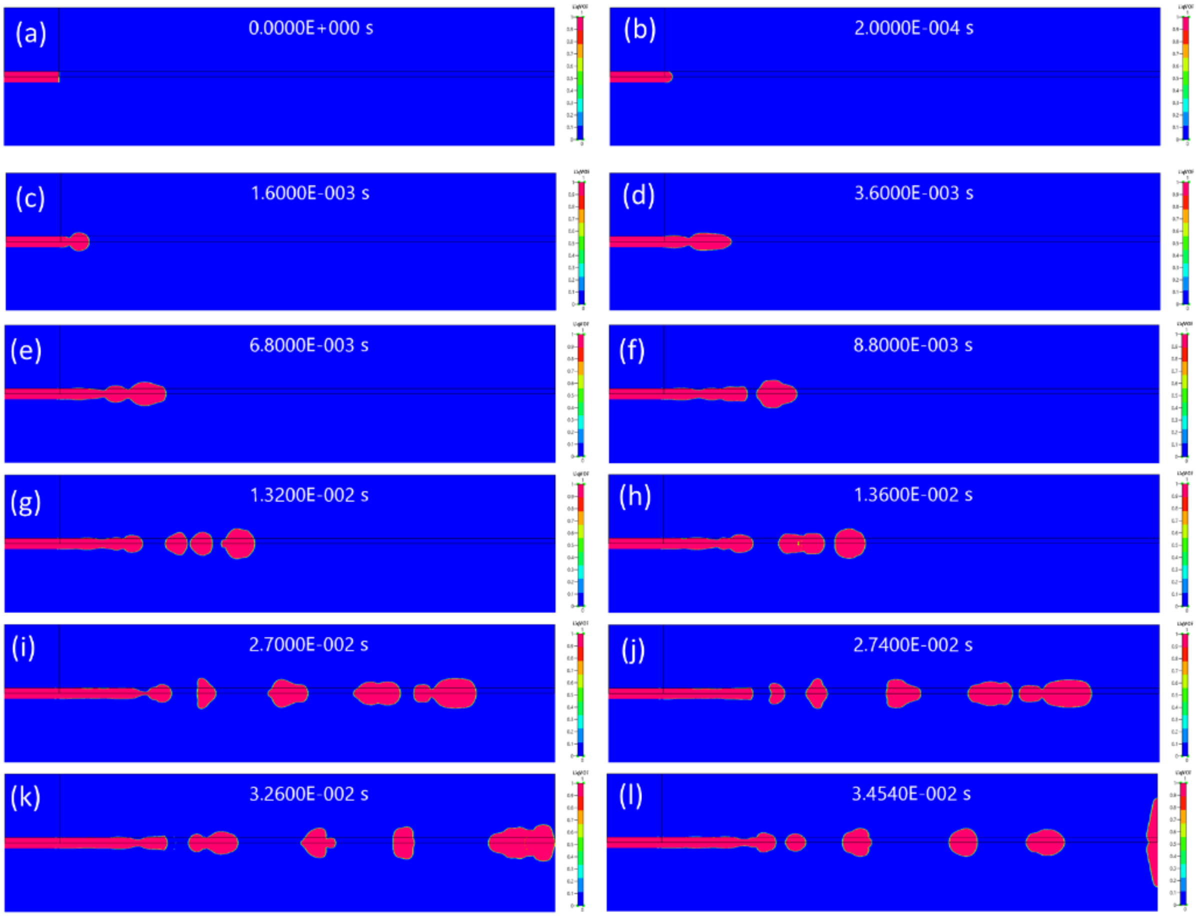

Figure 8.2- EHD Jetting at a flow rate of 0.07liters/hr and applied a voltage of 4KV. (a) t= 0s, (b) t=0.2ms deformation begins , (c) t = 1.6s, droplet deforms into oblate shape (d) t = 3.6ms, droplet deforms into prolate shape (e) t=6.8ms, pinch point before droplet detachment, (f) 8.8ms, first droplet detaches (g) 13.20ms, multiple droplet develops, (h) t=13.6ms, droplet coalesce and the jet advances, (i) 27ms, multiple droplets and pinch point before jets detaches, (j) t= 27.4ms, (k) t=32.6ms and (l) t=34.5ms when jet wets the collector plate.

The droplet development stages are as shown in Figure 8.2 with the droplet detachment occurring at about 8.8 milliseconds when an electric potential of 4kV is applied on the wall of the needle. After 0.2 milliseconds, meniscus deforms into a hemispherical shape, signalling the onset of jetting process, then the jet gradually develops into an oblate shape after 1.6 milliseconds and into a prolate shape after 3.6millisecond as the surface tension is overcome by the pull of the electric field. Lopez-Herrera and his colleagues [103] also concluded in their work that the shape a deformed droplet assumes (either oblate or prolate) is dependent on the ratio of the droplet radius to the Debye length[3] (which is a measure of the electrostatic effect on the charged droplet). As the stretching continues, more deformation is observed and at 8.8milliseconds, the first droplet detaches from the jet, after a shrink in the necking, thinning and pinching-off of the ejected droplet. Multiple droplets were observed after 13.2 milliseconds and some of the droplets coalesce at about 13.6 milliseconds as the jet advances in the direction of the flow. After 27.0 milliseconds of the flow, a very pronounced necking/pinching phenomenon was observed (as seen in Figure 8.2i) attached to the mainstream of the jet. Jets of varying sizes were observed as the solution and flow advances and just about 33 milliseconds, the first droplet hits the collector plate.

The corresponding electric field distributions along the flow direction are shown alongside with the VOF distribution in Figure 8.3. The electric field accounts for both the tangential and normal electric stresses. While the former maintains the conical shape, the latter accelerates the liquid in the direction of the jet. The tangential component stretches the fluid and the normal component balances and overcomes the surface tension in the air/liquid interface.

---

[3] Debye length: The distance from a particle where the electrostatic force is significantly reduced [119]. It is the distance over which a charge is shielded by the ions in a solution. It is a measure of the electrostatic effect on the charged droplet.

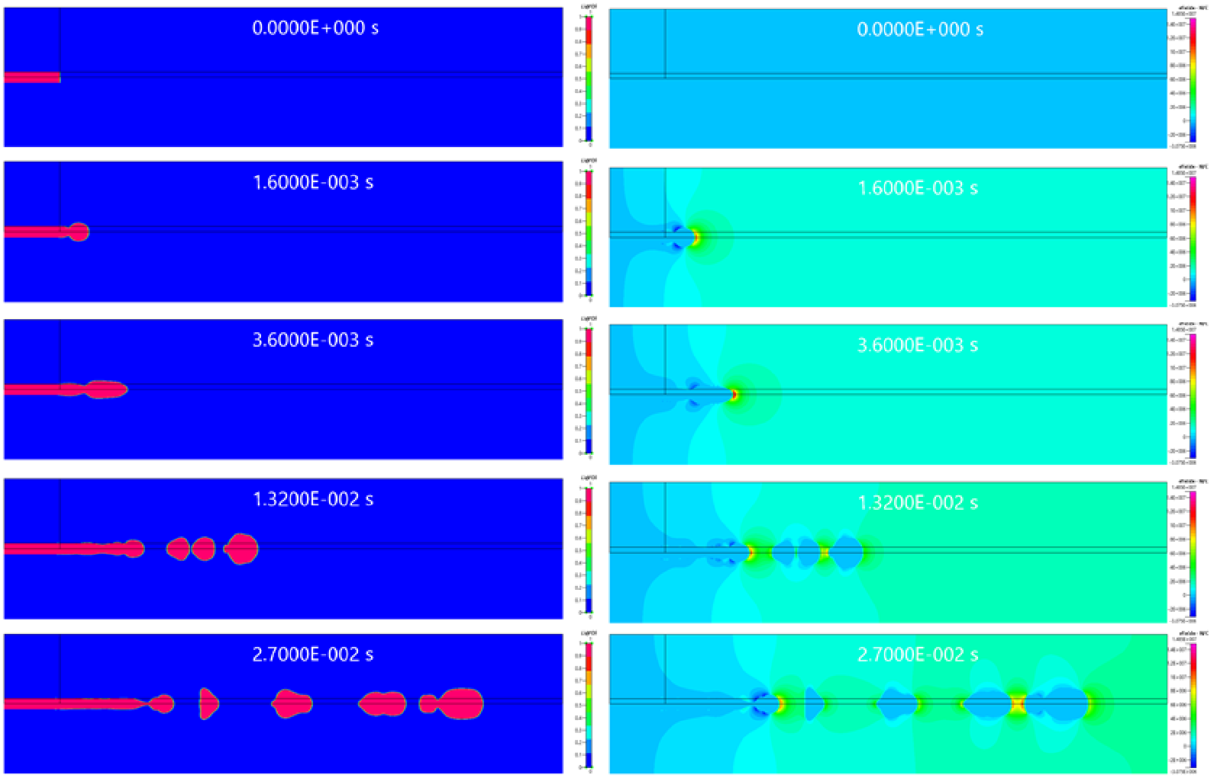

Figure 8.3- Plots showing the electric field changing with change the flow of the fluid at various time steps. The left pane shows the Flow distribution and the right pane shows the electric field distribution at various time steps. The electric field was also seen to be highest at the air/liquid interface.

The applied electric potential induces surface charges on the periphery and not inside the bulk of the fluid jet, and this phenomenon can be seen in the electric field distributions of Figure 8.3. Taylor and Melcher [19], [55] argued that the surface charges were adequately balanced by the surface tension of the bulk which results in a dynamically stable condition. They noted that the consequence of this interaction is an elongated shape of the fluid droplet. This distortion results in the formation of the popular Taylor cone. The size of this cone is affected by parameters including fluid properties, electric potential and flow rate of the fluid [6], [52], [84]. Ultimately, this Taylor cone is developed from the application of electric field to a free-flowing dielectric liquid.

Also, as seen in Figure 8.3, the air-liquid interface (where the coupling between the electric and hydrodynamic forces takes place) was observed to be continuously changing to stabilize under the effects of pressure, fluid flow characteristics, and charge accumulation of the dynamic liquid surface. It was observed that electric field moved along with the moving fluid, a phenomenon that is not observed experimentally, the consequence of this is that there is a strong interaction between the charged dielectric fluid and applied electric potential on the wall. Therefore, altering the electric field has the potential to control the fluid front and hence the jetting.

At various instances, it was observed the jets coalesce and further split. There is an apparent reduction in the surface tension of the liquid because the electric charges on the surface create an electrostatic pressure opposite to the capillary pressure. This electrostatic pressure is at its maximum at the end of the pendent drop, but it is also exerted in the drop detachment zone. In the dripping mode, the emission of drops may occur at regular time intervals, without the creation of satellites, so that all the drops have the same size, but this is not in case in this test case.

8.2 Droplet Diameter

In general, drop diameter remains greater than that of the capillary, thus leading to the emission of large drops at low frequencies. For a given flow rate, the maximum emission frequency may increase (and the minimum drop diameter decrease) significantly if the diameter of the capillary is reduced. Many drops were accompanied by the formation of one or several droplets. The jet diameters also varied in sizes.

8.3 Charge Distribution and Electric Potential Distribution

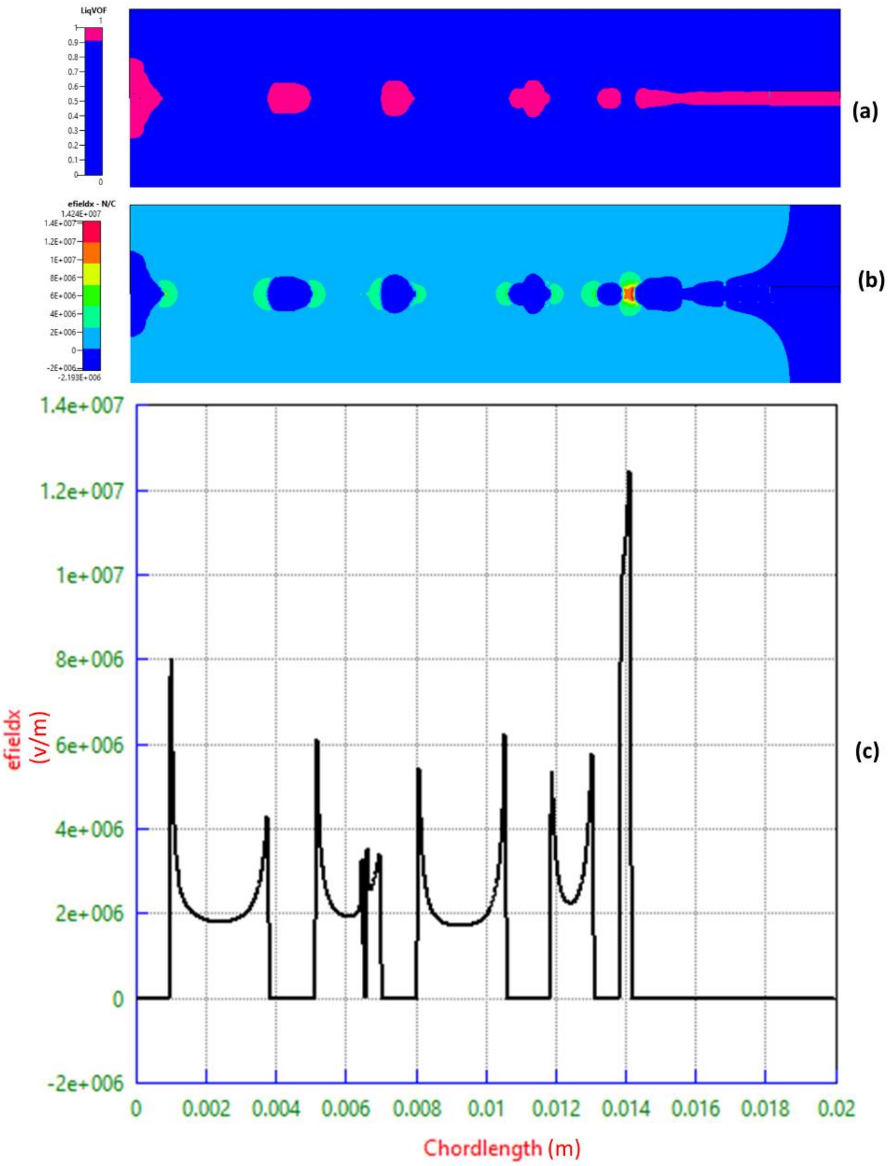

Figure 8.4- Charge accumulation at the fluid interface. (a) The volume of Fluid Distribution and (b) Electric Field Distribution (V/m) after 34 milliseconds. The electric field is strongest the air/liquid interface to a magnitude of 12.5 MV/m The X-axis, labelled Chord length represents the configuration distances along the axis of symmetry, the capillary is of 0.002 meters long and the distance between the tip of the capillary and the collector plate is 0.018 meters.

Under the influence of an applied electric field, free charges accumulate at the interface, which induces droplet deformation and EHD flows inside and outside the droplet. As expected for a dielectric fluid, the electric charges were mainly localized at the surface of the main fluid, very low charge/zero charge density was observed in the bulk of the fluid and of low magnitude in vacuum. The electric field is strongest at the surface of the mainstream jet, to a magnitude of $1.25\times10^{7}\,V/m$ and ranges between $2.5\times10^{6}-8.0\times10^{6}\,V/m$ at the tip of the emerging jets travelling downstream. Figure 8.4 shows the electric field distribution after 34 milliseconds when an electric potential of 4kV is applied to the walls of the needle.

8.4 Velocity Magnitude

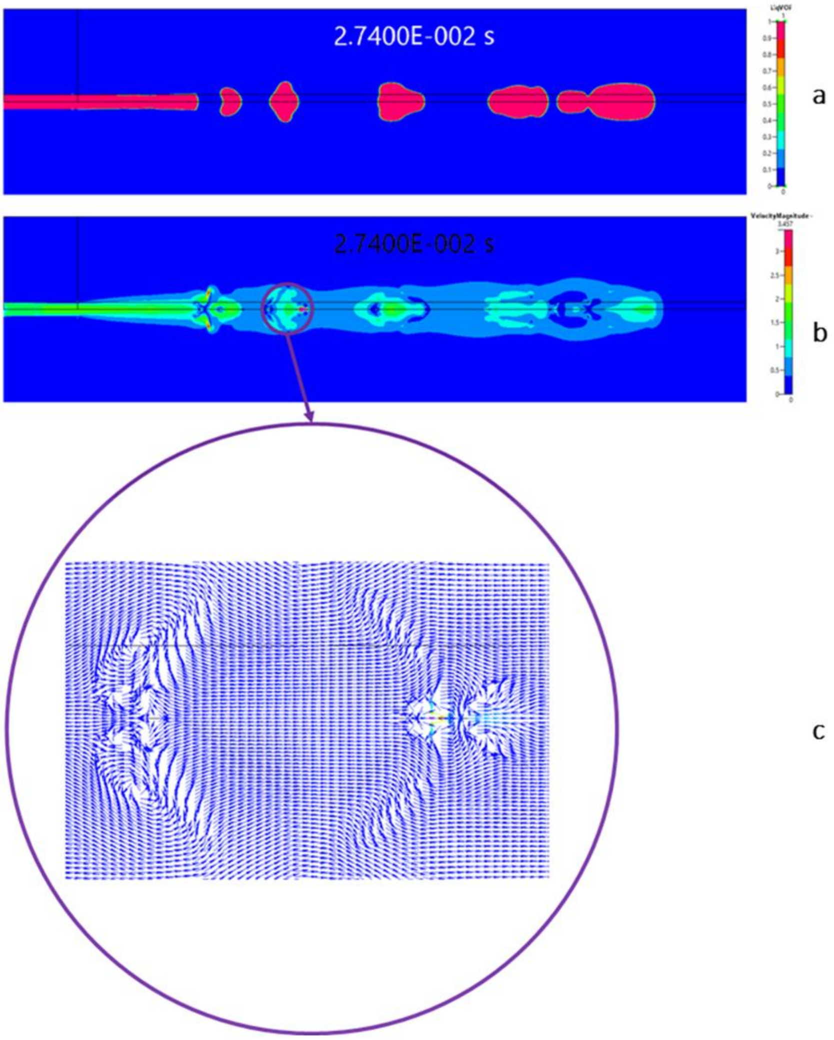

Figure 8.5- (a)VOF, (b) Velocity magnitude and
(c) velocity field (around droplet) at 27.4ms

The velocity field, as shown in Figure 8.5c, gives a consistent pattern of toroid-shaped vortex as reported in [82]. The liquid moving in the direction of the main flow is divided by this vortex. This phenomenon of division causes the majority of the liquid to be drawn back into the centre vortex, recirculated and mixed with the main flow, while the remaining liquid is drawn into the jet [82], [100]. To predict the effects that are likely to influence the production and features of jets, the knowledge of flow patterns inside liquid menisci will be needful.

9. DEPENDENCE OF ELECTROHYDRODYNAMIC JETTING ON THE PROCESS PARAMETERS.

In this section we describe the roles of two major parameters that affect EHD jetting-applied potential and fluid flow rate. The effect of these on the emerging jets, the electric field distribution, velocity field and flow profile has been analysed.

To overcome the surface tension, γ, the magnitude of the charge on a droplet is described by the Rayleigh limiting charge [104]–[106].

$$q_{\max} = \pi\left(8\varepsilon_0\gamma d_d^3\right)^{1/2} \tag{68}$$

where $q_{\max}$ is the maximum magnitude a charge a droplet can carry, d_d is the diameter of the droplet and ε_0 is the permittivity of the vacuum. This equation implies that for dielectric fluids with low surface tension, only a small magnitude of net charge is needed to detach the droplet from the capillary, therefore a reduced applied potential is required to induce jetting, thus lower power requirement for to drive the process.

Also, the feed flow rate (also known as drop deployment rate), which is approximated as the cone formation rate, has been approximated by Chen et al [107] to be:

$$Q_c \sim \frac{\pi d_n^4}{128\mu L_{cp}}\left(\frac{\varepsilon_0 E_0^2}{2} - \frac{2\gamma}{d_n} + \Delta P\right) \tag{69}$$

where μ is the fluid viscosity, d_n and L_{cp} are the geometrical dimensions of the capillary, representing the inner diameter and the length, E_0 is the magnitude of the electric field, γ is the surface tension at the air/liquid interface and ΔP is the hydrostatic pressure. The three expressions in the bracket (in equation (69)), represent the electric pressure, capillary pressure and hydrostatic pressure respectively; these three are the driving forces that draw the flow out of the capillary.

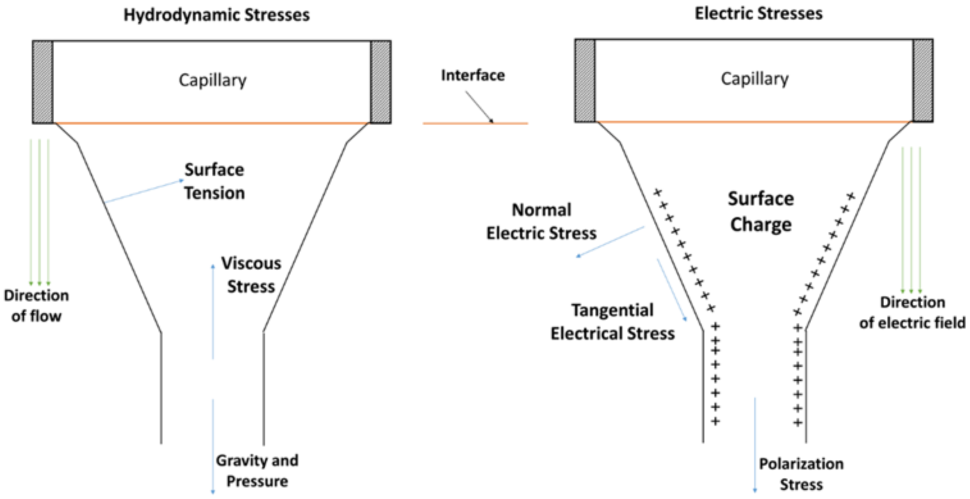

Figure 9.1- Schematic of EHD forces- both hydrodynamic and electric stresses. The three main hydrodynamics forces include; the air/liquid surface tension, viscous forces, gravity and hydrostatic forces. The three main electric forces acting at the interface of the drop are the polarization forces, the tangential and normal electric forces.

From equation (69), it is apparent that an increase in the voltage rate leads to a greater throughput.

9.1 Flow rate/Fluid velocity

A range of fluid flow rates was tested at 4kv. At some instances, the jetting was totally suppressed and at some, it was well pronounced. Fluid velocity of magnitudes 0.004m/s, 0.01m/s and 0.1m/s were used. Also, at a higher potential of 25kv, the flow rate was varied at 0.06m/s and 0.01m/s to observe if there is any significant difference in the meniscus at higher electric field intensity.

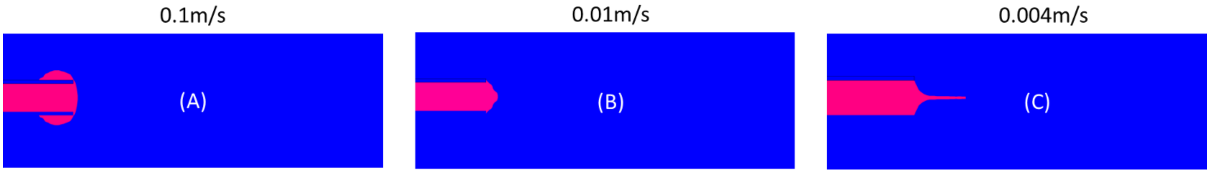

Figure 9.2- Flow development after 11 milliseconds when a voltage of 4kv was applied. (A) at flow rate of 0.1m/s, jetting was suppressed and the jets wet the capillary to clog the nozzle, (B) at a flow rate of 0.01m/s, the meniscus deforms into the conical shape and signals the onset of the micro dripping mode, and (C) at a flow rate of 0.004m/s. the cone-jet mode develops and the emerging jet grows into very thin jets.

The droplet wets the capillary tube and jetting is totally suppressed when a potential of 4kv is applied to a fluid flowing at 0.1m/s. At a flow velocity of 0.01m/s, the Taylor cone is formed, and droplet deforms into a conical meniscus without the development of the cone-jet mode or any jet detachment but signals the onset of the micro dripping mode. When the flow rate is further reduced to 0.004m/s the cone-jet emerges with a perfect conical base, with a very low ratio of capillary diameter to jet diameter, as shown in Figure 9.2. This agrees strongly with the operational map developed by Collins et al [102], where at a moderately strong electric field and low flow rate, the cone-jet mode was predicted. Also, it can be observed at the drop diameter reduces with the flow rate. At a lower voltage, increasing the flow rate will mean there won't be enough electrical field strength to stretch the solution being ejected due to insufficiently charged ions.

The maximum field intensity was obtained at the tip/interface of the air/liquid jet/drops, as $3.4\times10^{6}\,V/m$, $8.1\times10^{6}\,V/m$ and $3.2\times10^{7}\,V/m$ at flow rates of 0.1m/s, 0.01m/s and 0.004m/s respectively; showing a higher field intensity when the flow velocity was set at 0.004m/s, this explains while there is a great pull and stretch on the jet; the electric field strength is least when 0.1m/s hence the reason why the jet wets and clogs the capillary tip. At 0.01m/s there was a pulsating effect on the emerging jet showing a little imbalance in the viscous stress and the tangential electric stress that pulls the jet out of the capillary.

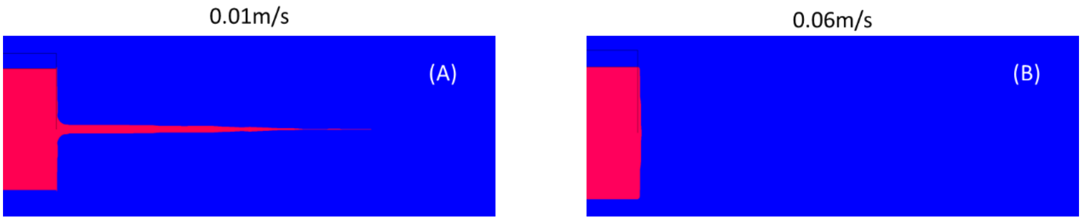

Figure 9.3- Flow development after 0.8 milliseconds when a voltage of 25kv was applied. (A) at a flow velocity of 0.01m/s, the Taylor cone was suppressed, and the onset of jetting was observed at a very early stage. (B) at a flow velocity of 0.06m/s, a lower flow rate takes slightly longer time before jetting occurs, but the Taylor cone was suppressed as well.

When a higher electric field intensity was applied, a slightly different deformation pattern took place. The Taylor cone stage was largely suppressed with the jet occurring just immediately at the tip of the capillary, a phenomenon similar to multi-spindle jet mode. This is as shown in Figure 9.3. At higher flow rates, the jet occurs very fast. The forces exerted by the electric field overcomes the surface tension at the air/liquid interface quite faster. At lower flow rate, only a small amount of solution is pulled out from the capillary thereby leading to smaller droplet diameter/size. At a greater measure, increasing the flow rate suppresses the emergence of cone-jet to form drops and spray solution.

9.2 Applied Voltage

At a flow velocity of 0.06m/s, the applied potential was varied to be 25kv, 20kv, 15kv and 10kv and the resulting flow profile was observed to check the effects of the applied DC voltage of the EHD jetting.

As observed by Baumgarten [108], initially, the jet/drop diameter decreases with increase in applied voltage and then increases with extra increase in the applied voltage. Increasing the electric field intensity yields an increase in the electrostatic stresses, therefore an increase in the volumetric flow rate and consequently pulls out more liquid out of the capillary. Just as mentioned in the previous section, at a lower voltage, there won't be enough electrical field strength to stretch the solution being ejected due to insufficiently charged ions.

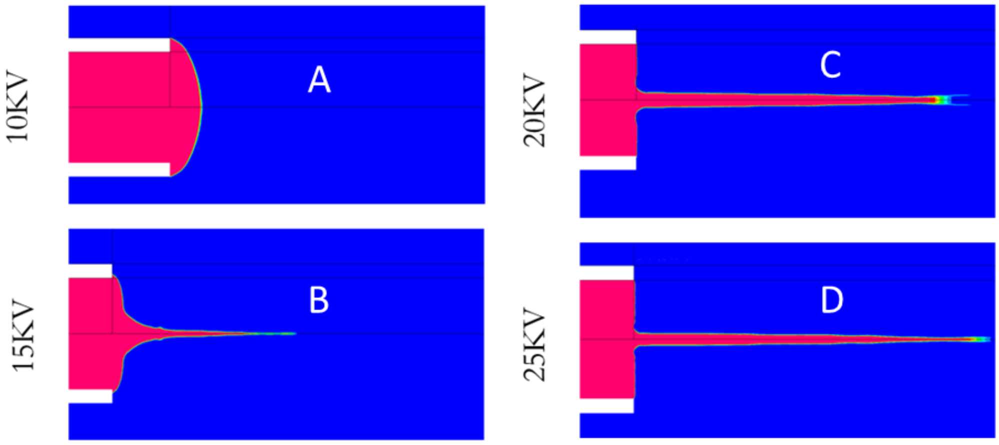

Figure 9.4- Flow distribution after 20ms at 0.06m/s when (A) an electric potential of 10KV is applied, (B) 15KV, (C) 20KV and (D) 25KV

At higher voltage, there is higher jetting frequency, this will, therefore, result in higher throughput. Laudenslager and Sigmund [109], pointed out that as the applied voltage is increased (and consequently, the electric field intensity), there is a transition in the shape of the meniscus from hemispherical shape/drop to a conical shape, and when after a certain magnitude, the cone disappears.

In conclusion, there is a very strong relationship between the flow rate and the EHD jet and between the applied voltage and the emerging jet. For any desired EHD mode (with cone-jet or dripping), the flow rate and voltage must be carefully chosen, this is the assertion of most researches, but we need to have a holistic insight into the role of the fluid viscosity, dielectric constant of the solution and the solution conductivity as these also affect the emerging features in EHD. The coming chapters give insight into their roles.

10. FLUID VISCOSITY AND CORRESPONDING EFFECTS ON FLUID FLOW, VELOCITY MAGNITUDE AND ELECTRIC FIELD DISTRIBUTION IN ELECTROHYDRODYNAMIC JETTING.

There is a strong effect of the viscosity on the jet, but to what extent? This study reveals the unique effect of viscosity on the fluid flow, by investigating the flow characteristic over time. More importantly, is the effect on the interaction of the fluid and the electric field. The results from the chapter were presented at conference organised by the Institute of Physics (Manchester, April 2019) and have been accepted for publication in the Journal of Physics Conference series.

The EHD equation for a dielectric fluid provides insight into the role of viscosity in droplet formation; expressed as:

$$\rho \frac{\partial \vec{u}}{\partial \mathrm{t}} = -\nabla P + \mu \nabla^2 \vec{u} + \rho g + f_e \tag{70}$$

Where ρ is the fluid density, μ is the viscosity of the solution, P is the pressure, u is flow velocity, g is the gravitational constant, and f_e is the electromechanical force.

The left-hand side of the expression describes the fluid acceleration and the right-hand side gives the summation of several forces acting on the system. The second term on the right-hand side is the viscous force caused by the viscosity of the solution, the force opposes jet formation and movement [86], [110].

This section offers insight into how fluid viscosity affects EHD flow, by observing the flow profile, velocity magnitude, electric field and electric potential distribution. For the discussion, three liquids have been defined with viscosities, μ_1, μ_2 and μ_3 in increasing order of magnitude; μ_2 has the same property as water, while μ_1 was assigned a viscosity $0.1\mu_2$ and μ_3 assigned a viscosity of $10\mu_2$. The operating conditions are at 10kV and a flow rate of 0.07 litres/hr.

10.1 Flow Profile

The jet diameter, length and contact angle differ for different viscosities. It was observed that jetting occurs earlier with the fluid with lower viscosity. Also, the liquid wets the needle wall at higher viscosity and after some time, it builds up around the wall. Less viscous fluids do not wet the needle external walls at all. Figure 10.1 shows the VOF distribution of the EHD flows for the 3 different samples. The length of the jet increases with an increase in viscosity. Also, an increase in the viscosity reduces the droplet size/jet diameter just as reported in [110], [111].

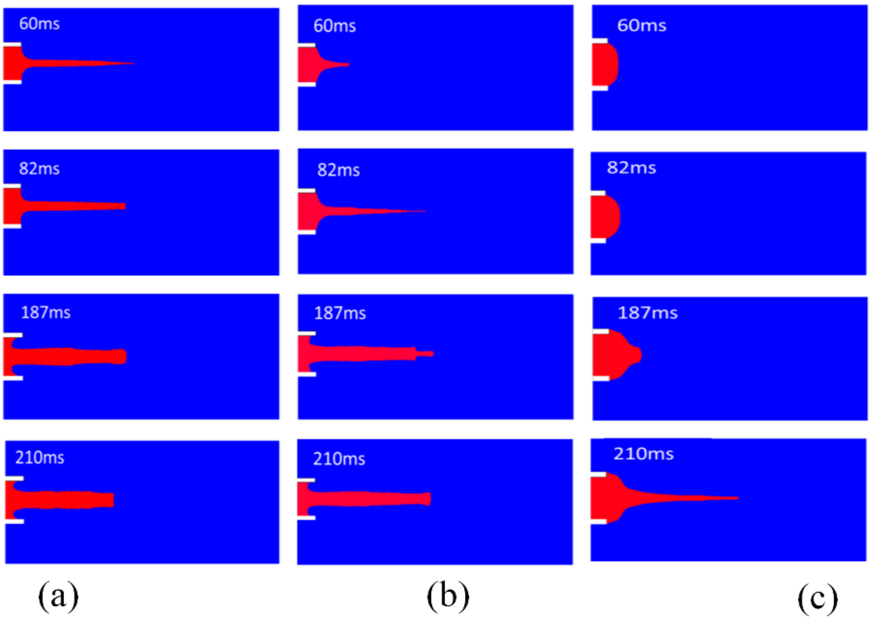

Figure 10.1- VoF distribution for different solutions (a) viscosity, μ_1 (b) viscosity, μ_2 and (c) viscosity, μ_3 when a voltage of 10kV was applied at a flow rate of 0.07 litres/hr.

10.2 Velocity Magnitude

A very significant difference was observed in the velocity magnitudes of the three different solutions. After 11 milliseconds, for the μ_1 solution, the peak velocity was about 130m/s, for μ_2, approximately 33m/s and for the most viscous solution, μ_3, a maximum velocity of 0.8m/s was reached. Also, it took a longer time for these peak velocities to be reached as the viscosity increases.

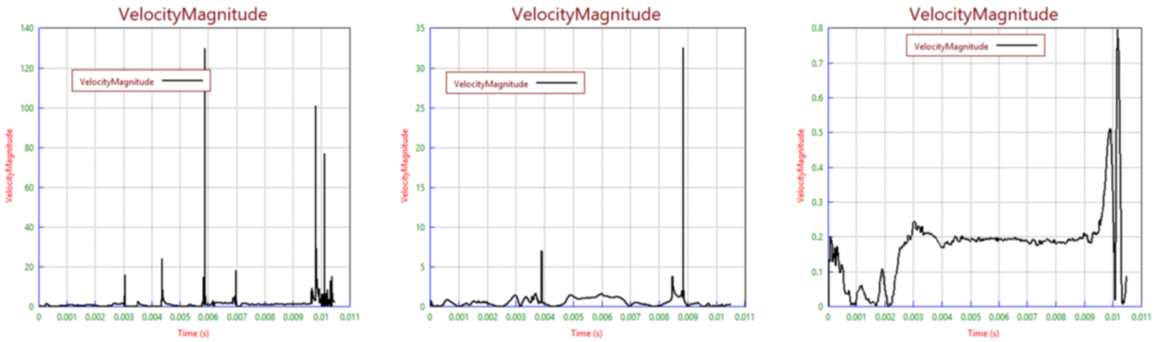

(a) (b) (c)

Figure 10.2- Velocity Magnitude for different solutions (a) viscosity, μ_1 (b) viscosity, μ_2 and (c) viscosity, μ_3

10.3 Electric Field Distribution and Electric Potential

Leaky dielectric fluid accumulates charge on the drop-fluid interface and allows charge relaxation. The fluid also allows ohmic currents to jump from bulk and charge convection through the interfacial fluid flow. For all the solutions, the electric field strengths were in the magnitude of $10^6 V/m$, as seen in Figure 10.3. Higher electric field magnitudes/strength were observed for the fluid of lower viscosity than that of the higher viscosity. This implies that higher field strength is required to produce jetting and overcome the fluid surface tension for highly viscous liquids.

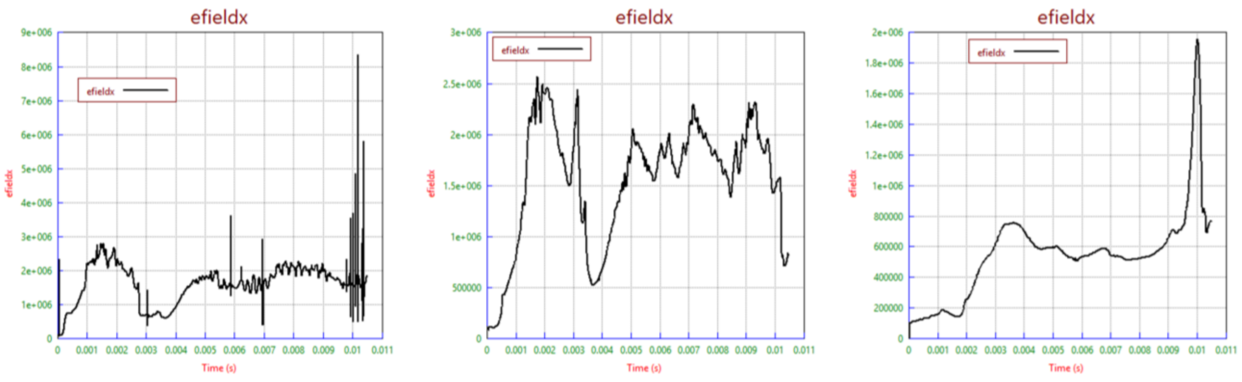

(a) (b) (c)

Figure 10.3- Electric field (V/m) for different solutions (a) viscosity, μ_1 (b) viscosity, μ_2 and (c) viscosity of μ_3.

Higher electric field magnitudes/strength were observed for the fluid of lower viscosity than that of the higher viscosity. This implies that higher field strength is required to produce jetting and overcome the fluid surface tension for highly viscous liquids. The result shows that the distribution of electric potential remained nearly unchanged regardless of the liquid viscosity, as seen in Figure 10.4.

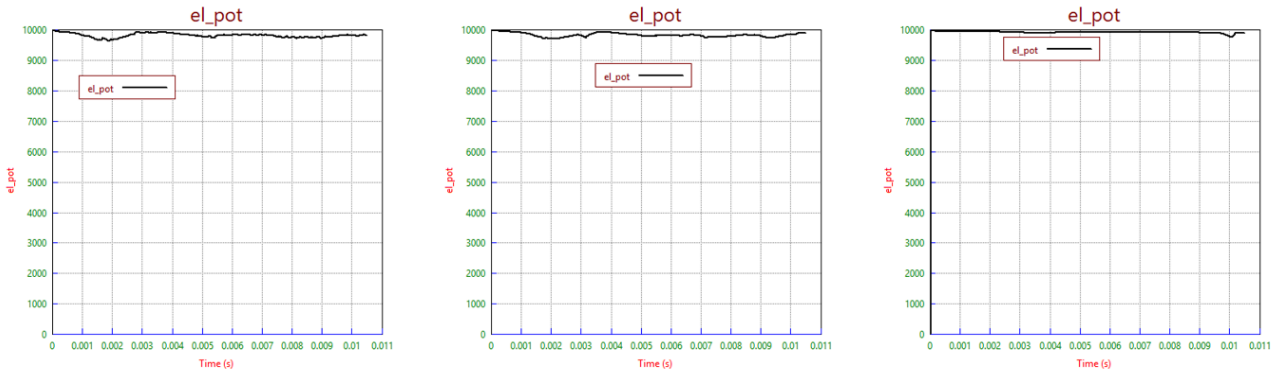

(a) **(b)** **(c)**

Figure 10.4- Electric Potential (V) for different solutions (a) viscosity, μ_1 (b) viscosity, μ_2 and (c) viscosity of μ_3.

In conclusion, the results from this study help to establish the resultant effect of solution viscosity in EHD applications. At higher viscosity, the solution resistance to flow is higher, and at certain magnitudes, the fluid wets the needle wall and droplet build-up to clog the capillary. The diameter of the jet decreases with viscosity. As observed for the velocity distribution, for faster throughput of the jets in EHD, a less viscous solution will be advantageous. Also, jetting occurs earlier in less viscous solutions. This study offers great potential for control of emerging features of EHD flows by manipulating the viscosity.

11. INSIGHT INTO THE ROLES OF CONDUCTIVITY AND DIELECTRIC CONSTANT IN EHD FLOWS

This section takes a view into the role and effect of the two physical properties of the dielectric fluid as they affect the EHD jetting behaviour; they are the liquid conductivity and permittivity. The focus is to look at how they affect the droplet deformation at the meniscus just at the capillary tip and the mode of the emerging jet/droplet.

According to Chen and Pui [112], the diameter of the droplet D_d is given as:

$$D_d = \left(\varepsilon\varepsilon_0 / K\right)^{1/3} Q^{1/3} \qquad (71)$$

where ε is the dielectric constant of the medium, ε_0 is the permittivity of vacuum, K is the conductivity and Q is the flow rate. This expression gives the law relating the drop diameter, the dielectric constant and conductivity. This implies that the droplet diameter increases with an increase in the permittivity of the medium and decreases with an increase in the conductivity of the solution.

During this investigation, varieties of charged jet emerged from the tip of the Taylor cone. Zargham and his colleagues [113] and Haider et al [114] gave a detailed overview of this unique phenomena, and these configurations are shown in Figure 11.1.

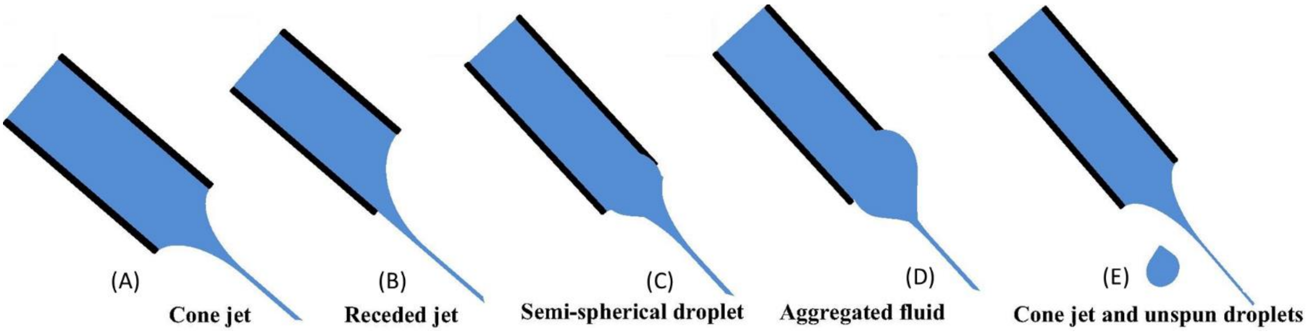

Figure 11.1- Formation of various jets when nylon 6 was electrospun in formic acid. (A) showing a typical cone jet that results into spun jets, (B) receded jet formation, (C) semi-spherical droplet, where the base of the jet takes a spherical shape, (D) aggregated jet and (E) similar to (A) but the emerging cone develops into droplets and not fibres. [113], [114]

11.1 Influence of Solution Conductivity

Two ratios of conductivity have been tested to ascertain the extent to which the liquid conductivity affects the resulting EHD jets. At a flow rate of 7.1ml/hr and applied potential of 10kv, the ratio varied from $0.1k$ and $10k$ (where the latter is the solution with higher conductivity and k is the electrical conductivity of water). There were remarkable observations which will be discussed in this section.

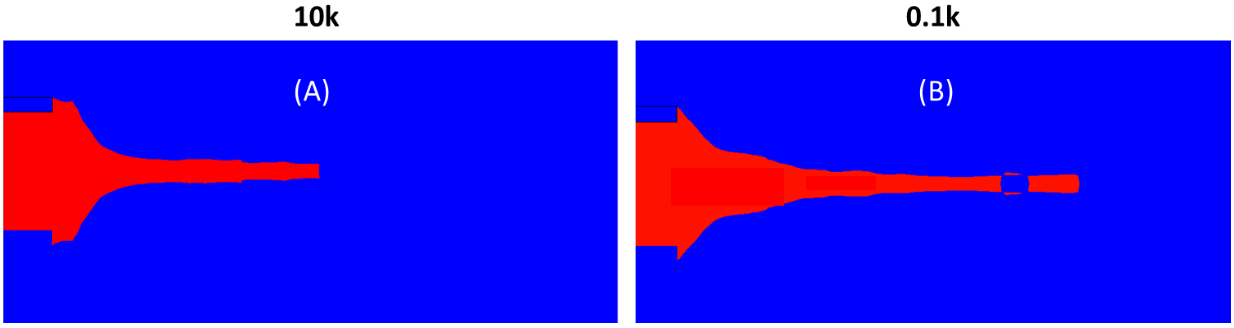

Figure 11.2- Flow development when a 10kv voltage was applied at a flow rate of 7.1ml/hr. (A) a solution of conductivity, 10k, shows a bigger diameter after 3.8 milliseconds (B) a solution of conductivity,0.1k, showing a well-developed cone and a slightly thinner droplet diameter and emergence of jet breakup at an instance.

Table 11.1 shows the maximum magnitude of electric field, pressure and velocity field as measured in the computational domains for the two liquids under consideration. At higher conductivity, there is a slightly stronger electric field- about twice that of the liquid with smaller magnitude of conductivity, this is because it allows more effective charging for the same electrostatic field [115]. After 3.8 milliseconds, Figure 11.2(A), shows that at higher conductivity, the droplet is slightly bigger and shorter and Figure 11.2(B), a well-formed cone-jet mode was developed with smaller jet diameter and a more stable jetting was observed with the emergence of jet breakup at an instance.

Table 11.1- Maximum magnitude of measured physical quantities in the modelled EHD jets to investigate the influence of solution conductivity. These values are maximum values obtained in the computational domain.

Physical Quantity	**Higher Conductive Liquid**	**Less Conductive Liquid**
$\lvert E \rvert (V/m)$	$2.18 \times 10^{7}\, V/m$	$1.59 \times 10^{7}\, V/m$
$P\left(N/m^{2}\right)$	$9.13 \times 10^{4}\, N/m^{2}$	$1\, N/m^{2}$
$\lvert v \rvert \left(m/s^{2}\right)$	$6.247\, m/s^{2}$	$13.35\, m/s^{2}$

The droplet diameter varies when the electrical conductivity changes; this is a very insightful point and was also observed and in agreement with Barrero et al [116] on the influence of conductivity to control the droplet diameter.

According to Barrero et al [116], a decrease in the magnitude of electrical conductivity will result in an increase in the tangential stress at the air/liquid interface and subsequently an increase in the liquid velocity at the interface; this can also be observed in Table 11.1, where the overall magnitude of the liquid velocity is higher for the less conductive liquid.

11.2 Influence of Dielectric Constants

Similar to the investigations of conductivity, two ratios of dielectric constant were modelled to determine the extent to which the EHD is affected. The following ratios were considered: 0.1ε and 10ε. The magnitude of ε is equal to the dielectric constant of water.

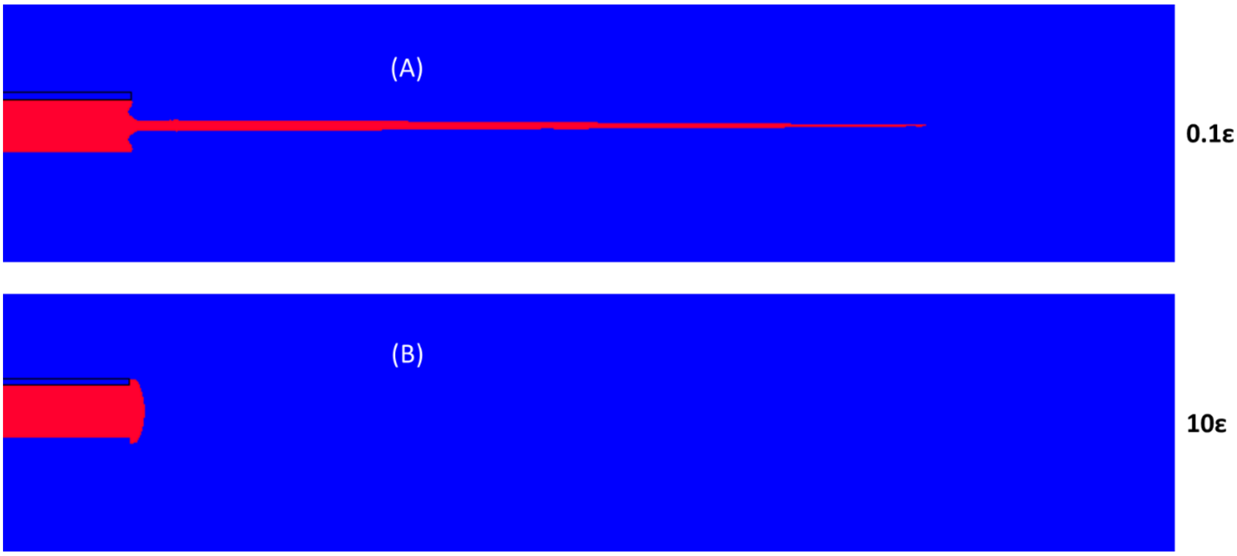

Figure 11.3- Flow profiles after 1.3 milliseconds when 10kv is applied at a flow rate of 7.1ml/hr. (A) a solution with permittivity of 0.1ε permittivity showing a fully developed, long jet but with the cone recessed into the capillary, and (B) a solution of with 10ε permittivity with the meniscus deforming into a hemispherical shape and which later build to wet the capillary tip.

The results show that permittivity has a very remarkable influence on the EHD jetting. As shown in Figure 11.3, jet diameter reduces with a decrease in magnitude of dielectric constant, confirming the relationship given in equation (71). Given an applied voltage 10kv and a flow rate of 7.1ml/hr, the velocity field is weaker with decrease in permittivity of the medium also there is an increase in the magnitude of electric field magnitude with increase in the dielectric constant, as summarised in Table 11.2. At a higher dielectric constant, jetting is almost suppressed in the process.

Table 11.2- Maximum magnitude of measured physical quantities in the modelled EHD jets to investigate the influence of permittivity of the medium. These values are maximum values obtained in the computational domain.

Physical Quantity	**Liquid with Higher ε**	**Liquid with Lower ε**
$\lvert E\rvert(V/m)$	$2.47\times10^{7}\,V/m$	$1.3\times10^{7}\,V/m$
$P\left(N/m^{2}\right)$	$12\times10^{5}\,N/m^{2}$	$8.3\times10^{3}\,N/m^{2}$
$\lvert v\rvert\left(m/s^{2}\right)$	$12.34\,m/s^{2}$	$1.82\,m/s^{2}$

The ideal fluid for this current work will be a poorly conducting fluid (also known as a leaky dielectric fluid). They allow electric charge to accumulate at the drop interface, hereby permitting tangential electric stress to be generated, this stress drags the fluid in motion which by implication generates hydrodynamic stresses at the liquid drop interface [20]. In leaky dielectrics, free charges accumulate on the interface of the fluids and hereby modify the field, particularly producing shear stress.

As seen in Figure 11.3(B), the jetting stage was suppressed, this is a case of perfect dielectrics, also called perfect insulators, they do not have any free charges and hence their conductivity is zero, as opposed to Figure 11.3(A).

In conclusion, both the permittivity and conductivity have shown great effects on the EHD jetting, with slight changes in the magnitude, the mode of jetting varies. And this also affects the shape of the jet- either concave or convex, which results in the droplet profile. In reality, these properties can be varied by changing the solvent concentration, polymer molecular weight and polymer weight concentration.

12. CONCLUSIONS AND FUTURE WORK

12.1 CONCLUSIONS

A thorough review of the literature has been undertaken to understand the mathematical formulation of EHD equations and how each of the terms relates to the process of electrospinning. Also, I have adapted current research findings to the present work and developed a computational model that encompasses all these findings into a tightly coupled solver environment.

The results obtained compared well both with experimental and computational works - both for the flow profiles and distribution of the flow field characteristics. The effect of flow rate, voltage and rheological properties (including viscosity, conductivity, and permittivity) has been accurately captured by the computations made so far.

The axisymmetric model has shown results that compare well with literature. It has been shown that the model developed has the capability to handle the complex multiphase EHD problem very well. We have been able to depict the coupling between the electric field and the flow field- showing that the electric field influences the flow and the flow influences the electric field as well. The use of the VOF technique has proved suitable for capturing the fluid interface, alongside structured meshing; as against unstructured meshing. The main conclusions drawn from this work are expanded further in the sections below.

12.1.1 Model Set up

In this course of setting up the model for the work, a few critical lessons were learnt, both from the numerous models that didn’t work and the few that produced the desired results. We can safely conclude that very fine meshes are needed to track the droplet and jets. Without fine meshes, even when though the emergence of jet was observed for some mesh configurations, there was no breakup. Also, we found that structured meshes gave significantly more accurate results in tracking the interface (using the VoF technique) comparing to triangular element unstructured meshes. A full grid dependency test was carried out and an optimal cell size was adopted. The model was validated with an experimental result and the current work showed great agreement with the work of Noymer and Garel [79]. The methodology presented handle two-dimensional, axisymmetric and full three-dimensional cases allowing for high levels of realism.

The Finite Volume Method (FVM) technique is adopted to discretize the differential equations into algebraic equations: FVM was chosen because of its conservative properties. A segregated solution method is employed where each momentum equation is solved separately, under an assumed pressure field; subsequently, the pressure is updated using a pressure correction algorithm. Each variable, therefore, results in a separate algebraic system, which is solved sequentially and repeatedly until convergence is achieved. All interpolations and finite difference terms within this framework have been computed using a central scheme, yielding, therefore, second-order accuracy spatially. Similarly, a Crank-Nicholson scheme has been used for the temporal discretization, resulting in second-order accuracy in time marching as well.

12.1.2 EHD Modes and Jet Meniscus and Flow Development

A robust model has been developed to capture different mode of the EHD jetting under various flow rates and/or electric field strength. From this work, the dripping mode, micro dripping mode, spindle and cone-jet modes have been modelled from the various combination of the voltage and flow rates. At various instances, the different forms of meniscus developed at the capillary tip, to include a hemispherical, circular, prolate, oblate, receded-concave and the Taylor-cone meniscus. All these various deformations are functions of the operating parameters or the rheological parameters of the solution. Typically, as the liquid flow emerges from the capillary, it assumes a convex conical shape as the flow interacts with the electric field, and the fine jets/droplets are ejected from the tip; but an increase in either the flow rate or the intensity of the electric field stretches out the jets and the convex cone transforms into a concave conical shape.

12.1.3 Effects of Rheological Parameters

Both the permittivity and conductivity have been shown to have substantial effect on the EHD jetting; with slight changes in the magnitude, the mode of jetting varies. And this also affects the shape of the jet- either concave or convex, which results in the droplet profile. In reality, these properties can be varied by changing the solvent concentration, polymer molecular weight and polymer weight concentration.

The results from this study help to establish the resultant effect of solution viscosity in EHD applications. At higher viscosity, the solution resistance to flow is higher, and at certain magnitudes, the fluid wets the needle wall and droplet build-up to clog the capillary. The diameter of the jet decreases with viscosity. As observed for the velocity distribution, for faster throughput of the jets in EHD, a less viscous solution will be advantageous. Also, jetting occurs earlier in less viscous solutions. This study offers great potential for control of emerging features of EHD flows by manipulating the viscosity.

The applied electric potential induced surface charges on the periphery and not inside the bulk of the fluid jet. The results obtained to investigate the fluid front interaction with the dynamic electric field also showed good agreement with the work of Sarkar et al [83]. This is a feature that is extremely difficult to visualise experimentally. This showed the capability of the model to handle strong coupling between the fluid flow and the electric field, meaning that as the electric field changes, it alters the fluid flow and vice versa. We can also conclude that the diameter of the droplet can be controlled by altering the flow rate and/or the electrical conductivity of the solution.

12.1.4 Effects of Process Parameters

Two key process parameters were varied to ascertain the accuracy of the model to predict their effects on the EHD process. The flow rate/flow velocity and the applied voltage. More than one EHD mode was predicted when the voltage and the flow rates were predicted. It was observed that electric field moved along with the moving fluid, a phenomenon that is not observed experimentally, the consequence of this is that there is a strong interaction between the charged dielectric fluid and applied electric potential on the wall. Therefore, altering the electric field has the potential to control the fluid front and hence the jetting.

12.2 FUTURE WORK

1. To further investigate the influences of the process and rheological parameters by expanding the test cases to a wider range of magnitudes and more specific liquids or polymers.

2. To include the process of solvent evaporation in the modelling so as to move a step closer to obtaining a perfect representation of the process.
3. Explore the 3D model computationally in a detailed manner, in order to investigate the emergence of 3D flow features. Importantly, to visualize the droplet formation and whipping instability phases for the process. Figure 12.1 shows a sample of 3D mesh.

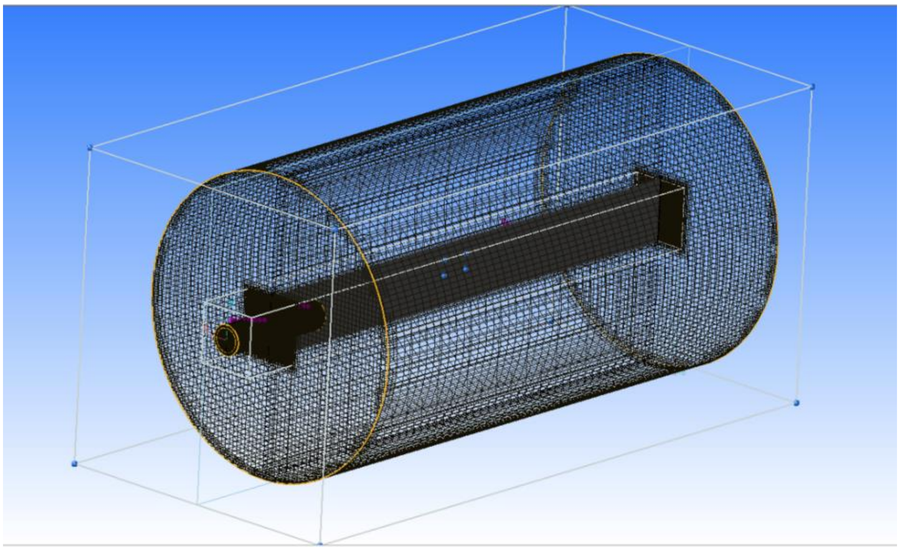

Figure 12.1- Proposed 3D Model configuration

4. Investigate the effect of the process parameters (including flow rate, applied voltage, contact angle) and fluid parameters (like fluid permittivity, surface tension and viscosity) on the droplet diameter and the electric field distribution including the liquid and jet surface area, surface angle, jet radius and jet length for the 3D model.
5. Comparisons of purpose-acquired experimental results and computational results.
6. Explore the adaptability of this model to co-axial EHD problems like co-axial electrospraying and electrospinning

It must be iterated here that the nature of the equations solved, the numerical methods used, and the characteristics of the specific solver deployed to ensure that no further model development is needed to extend our simulations from axisymmetric to full 3D.

REFERENCES

[1] V. Thavasi, G. Singh, and S. Ramakrishna, “Electrospun nanofibers in energy and environmental applications,” *Energy Environ. Sci.*, vol. 1, no. 2, p. 205, 2008.

[2] A. Castellanos, *Electrohydrodynamics*, vol. 380. Springer, 2014.

[3] D. A. Saville, “Electrohydrodynamics: The Taylor-Melcher leaky dielectric model,” *Annu. Rev. Fluid Mech.*, vol. 29, pp. 27–64, 1997.

[4] A. I. Zhakin, “Electrohydrodynamics,” *Physics-Uspekhi*, vol. 55, no. 5, p. 465, 2012.

[5] A. Ramos and C.-H. Chen, “Electrohydrodynamic Stability,” in *Electrokinetics and Electrohydrodynamics in Microsystems*, vol. 530, Springer Vienna, 2011, pp. 177–220.

[6] J. Zeng, D. Sobek, and T. Korsmeyer, “Electro-hydrodynamic modeling of electrospray ionization: CAD for a/spl mu/fluidic device-mass spectrometer interface,” vol. 2, pp. 1275–1278.

[7] A. Najjaran, R. Ebrahimi, M. Rahmanpoor, and A. Najjaran, “Numerical Simulation of Electrohydrodynamic (EHD) Atomization in the Cone-Jet Mode,” in *Applied Mechanics and Materials (Volumes 325-326)*, 2013, vol. 325, pp. 180–185.

[8] D. H. Reneker and A. L. Yarin, “Electrospinning jets and polymer nanofibers,” *Polymer (Guildf).*, vol. 49, no. 10, pp. 2387–2425, 2008.

[9] G. Viswanadam and G. G. Chase, “Modified electric fields to control the direction of electrospinning jets,” *Polymer (Guildf).*, vol. 54, no. 4, pp. 1397–1404, 2013.

[10] L. M. Bellan and H. G. Craighead, “Control of an electrospinning jet using electric focusing and jet-steering fields,” *J. Vac. Sci. Technol. B*, vol. 24, no. 6, pp. 3179–3183, 2006.

[11] Y. Yang, Z. Jia, L. Hou, Q. Li, L. Wang, and Z. Guan, “Controlled deposition of electrospinning jet by electric field distribution from an insulating material surrounding the barrel of the polymer solution,” *Dielectr. Electr. Insul. IEEE Trans.*, vol. 15, no. 1, pp. 269–276, 2008.

[12] V. Barinov and K. Levon, “Controlled electrospinning of fibers.” Google Patents, 2012.

[13] X. Wang and T. Lin, *Needleless electrospinning of nanofibers: Technology and applications*. CRC Press, 2013.

[14] S. K. L. Levengood and M. Q. Zhang, “Chitosan-based scaffolds for bone tissue engineering,” *J. Mater. Chem. B*, vol. 2, no. 21, pp. 3161–3184, 2014.

[15] J. F. Cooley, “Apparatus for electrically dispersing fluids.” Google Patents, 1902.

[16] A. Baji, Y. W. Mai, S. C. Wong, M. Abtahi, and P. Chen, “Electrospinning of polymer nanofibers: Effects on oriented morphology, structures and tensile properties,” *Compos. Sci. Technol.*, vol. 70, no. 5, pp. 703–718, 2010.

[17] Z.-M. Huang, Y. Z. Zhang, M. Kotaki, and S. Ramakrishna, “A review on polymer nanofibers by electrospinning and their applications in nanocomposites,” *Compos. Sci. Technol.*, vol. 63, no. 15, pp. 2223–2253, 2003.

[18] T. Subbiah, G. S. Bhat, R. W. Tock, S. Parameswaran, and S. S. Ramkumar, “Electrospinning of nanofibers,” *J. Appl. Polym. Sci.*, vol.

96, no. 2, pp. 557–569, 2005.

[19] G. Taylor, “Electrically driven jets,” *Proc. R. Soc. London. A. Math. Phys. Sci.*, vol. 313, no. 1515, pp. 453–475, 1969.

[20] I. Hayati, A. I. Bailey, and T. F. Tadros, “Investigations into the mechanisms of electrohydrodynamic spraying of liquids: I. Effect of electric field and the environment on pendant drops and factors affecting the formation of stable jets and atomization,” *J. Colloid Interface Sci.*, vol. 117, no. 1, pp. 205–221, 1987.

[21] L. Iarrondo and R. S. J. Manley, “Electrostatic Fiber Spinning from Polymer Melts .1. Experimental-Observations on Fiber Formation and Properties,” *J. Polym. Sci. Part B-Polymer Phys.*, vol. 19, no. 6, pp. 909–920, 1981.

[22] S. B. Warner, A. Buer, S. C. Ugbolue, G. C. Rutledge, and M. Y. Shin, “A fundamental investigation of the formation and properties of electrospun fibers,” *Natl. Text. Cent. Annu. Rep.*, pp. 83–90, 1998.

[23] N. Tucker, J. J. Stanger, M. P. Staiger, H. Razzaq, and K. Hofman, “The History of the Science and Technology of Electrospinning from 1600 to 1995,” *J. Eng. Fiber. Fabr.*, vol. 7, no. 2_suppl, p. 155892501200702, Jun. 2012.

[24] D. H. Reneker and I. Chun, “Nanometre diameter fibres of polymer, produced by electrospinning,” *Nanotechnology*, vol. 7, no. 3, pp. 216–223, Sep. 1996.

[25] M. Ziabari, V. Mottaghitalab, and A. K. Haghi, “Application of direct tracking method for measuring electrospun nanofiber diameter,” *Brazilian J. Chem. Eng.*, vol. 26, no. 1, pp. 53–62, 2009.

[26] J. D. Schiffman and C. L. Schauer, “A review: electrospinning of

biopolymer nanofibers and their applications," *Polym. Rev.*, vol. 48, no. 2, pp. 317–352, 2008.

[27] Z. Dong, S. J. Kennedy, and Y. Wu, "Electrospinning materials for energy-related applications and devices," *J. Power Sources*, vol. 196, no. 11, pp. 4886–4904, 2011.

[28] S. Ramakrishna, K. Fujihara, W.-E. Teo, T. Yong, Z. Ma, and R. Ramaseshan, "Electrospun nanofibers: solving global issues," *Mater. today*, vol. 9, no. 3, pp. 40–50, 2006.

[29] D. Li and Y. Xia, "Electrospinning of nanofibers: reinventing the wheel?," *Adv. Mater.*, vol. 16, no. 14, pp. 1151–1170, 2004.

[30] P. D. Dalton, C. Vaquette, B. L. Farrugia, T. R. Dargaville, T. D. Brown, and D. W. Hutmacher, "Electrospinning and additive manufacturing: converging technologies," *Biomater. Sci.*, vol. 1, no. 2, pp. 171–185, 2013.

[31] N. Bhardwaj and S. C. Kundu, "Electrospinning: a fascinating fiber fabrication technique," *Biotechnol. Adv.*, vol. 28, no. 3, pp. 325–347, 2010.

[32] K. Sasipriya, R. Suriyaprabha, P. Prabu, and V. Rajendran, "Synthesis and characterisation of polymeric nanofibers poly (vinyl alcohol) and poly (vinyl alcohol)/silica using indigenous electrospinning set up," *Mater. Res.*, vol. 16, no. 4, pp. 824–830, 2013.

[33] J. Doshi and D. H. Reneker, "Electrospinning process and applications of electrospun fibers," pp. 1698–1703.

[34] K. H. Lee, H. Y. Kim, H. J. Bang, Y. H. Jung, and S. G. Lee, "The change of bead morphology formed on electrospun polystyrene fibers," *Polymer (Guildf).*, vol. 44, no. 14, pp. 4029–4034, 2003.

[35] J. . Deitzel, J. Kleinmeyer, D. Harris, and N. . Beck Tan, “The effect of processing variables on the morphology of electrospun nanofibers and textiles,” *Polymer (Guildf).*, vol. 42, no. 1, pp. 261–272, 2001.

[36] Q. Yang, Z. Li, Y. Hong, Y. Zhao, S. Qiu, C. Wang, and Y. Wei, “Influence of solvents on the formation of ultrathin uniform poly(vinyl pyrrolidone) nanofibers with electrospinning,” *J. Polym. Sci. Part B Polym. Phys.*, vol. 42, no. 20, pp. 3721–3726, Oct. 2004.

[37] A. K. Haghi and M. Akbari, “Trends in electrospinning of natural nanofibers,” *Phys. status solidi*, vol. 204, no. 6, pp. 1830–1834, Jun. 2007.

[38] H. Fong, I. Chun, and D. . Reneker, “Beaded nanofibers formed during electrospinning,” *Polymer (Guildf).*, vol. 40, no. 16, pp. 4585–4592, 1999.

[39] T. Uyar and F. Besenbacher, “Electrospinning of uniform polystyrene fibers: The effect of solvent conductivity,” *Polymer (Guildf).*, vol. 49, no. 24, pp. 5336–5343, 2008.

[40] A. Koski, K. Yim, and S. Shivkumar, “Effect of molecular weight on fibrous PVA produced by electrospinning,” 2004.

[41] T. J. Sill and H. A. von Recum, “Electrospinning: Applications in drug delivery and tissue engineering,” *Biomaterials*, vol. 29, no. 13, pp. 1989–2006, 2008.

[42] C. Zhang, X. Yuan, L. Wu, Y. Han, and J. Sheng, “Study on morphology of electrospun poly(vinyl alcohol) mats,” *Eur. Polym. J.*, vol. 41, no. 3, pp. 423–432, 2005.

[43] L. LARRONDO and R. S. J. MANLEY, “Electrostatic Fiber Spinning from Polymer Melts .3. Electrostatic Deformation of a Pendant Drop of

Polymer Melt," *J. Polym. Sci. Part B-Polymer Phys.*, vol. 19, no. 6, pp. 933–940, 1981.

[44] C. J. Buchko, L. C. Chen, Y. Shen, and D. C. Martin, "Processing and microstructural characterization of porous biocompatible protein polymer thin films," *Polymer (Guildf).*, vol. 40, no. 26, pp. 7397–7407, 1999.

[45] E. T. Thostenson, C. Y. Li, and T. W. Chou, "Nanocomposites in context," *Compos. Sci. Technol.*, vol. 65, no. 3–4, pp. 491–516, 2005.

[46] A. L. Andrady, *Science and technology of polymer nanofibers*. John Wiley & Sons, 2008.

[47] B. Bugarski, B. Amsden, M. F. A. Goosen, R. J. Neufeld, and D. Poncelet, "Effect of electrode geometry and charge on the production of polymer microbeads by electrostatics," *Can. J. Chem. Eng.*, vol. 72, no. 3, pp. 517–521, 1994.

[48] S. Rafiel, S. Maghsoodloo, B. Noroozi, V. Mottaghitalab, and A. K. Haghi, "Mathematical modeling In electrospinning process of nanofibers: A detailed review," *Cellul. Chem. Technol.*, vol. 47, no. 5–6, pp. 323–338, 2013.

[49] K. Garg and G. L. Bowlin, "Electrospinning jets and nanofibrous structures," *Biomicrofluidics*, vol. 5, no. 1, p. 13403, 2011.

[50] D. H. Reneker, A. L. Yarin, H. Fong, and S. Koombhongse, "Bending instability of electrically charged liquid jets of polymer solutions in electrospinning," *J. Appl. Phys.*, vol. 87, no. 9, pp. 4531–4547, 2000.

[51] A. L. Yarin, S. Koombhongse, and D. H. Reneker, "Bending instability in electrospinning of nanofibers," *J. Appl. Phys.*, vol. 89, no. 5, pp. 3018–3026, 2001.

[52] M. M. Hohman, M. Shin, G. Rutledge, and M. P. Brenner, “Electrospinning and electrically forced jets. I. Stability theory,” *Phys. Fluids*, vol. 13, no. 8, pp. 2201–2220, 2001.

[53] M. M. Hohman, M. Shin, G. Rutledge, and M. P. Brenner, “Electrospinning and electrically forced jets. II. Applications,” *Phys. Fluids*, vol. 13, no. 8, pp. 2221–2236, 2001.

[54] J. Zeng, “Electrohydrodynamic modeling and its applications to microfluidic devices,” pp. 13–19.

[55] J. R. Melcher and G. I. Taylor, “Electrohydrodynamics: a review of the role of interfacial shear stresses,” *Annu. Rev. Fluid Mech.*, vol. 1, no. 1, pp. 111–146, 1969.

[56] Y. Imura, “The incorporation of electrohydrodynamics and other modifications into a dry spinning model to develop a theoretical framework for electrospinning,” 2012.

[57] A. R. Blythe and D. Bloor, *Electrical properties of polymers*. Cambridge University Press, 2005.

[58] Z. Ahmad, “Polymeric dielectric materials,” *Dielectr. Mater.*, pp. 3–26, 2012.

[59] Z. Li and C. Wang, “Effects of Working Parameters on Electrospinning,” 2013, pp. 15–28.

[60] T. Nitanan, P. Opanasopit, P. Akkaramongkolporn, T. Rojanarata, T. Ngawhirunpat, and P. Supaphol, “Effects of processing parameters on morphology of electrospun polystyrene nanofibers,” *Korean J. Chem. Eng.*, vol. 29, no. 2, pp. 173–181, Feb. 2012.

[61] A. K. Haghi and M. Akbari, “Trends in electrospinning of natural nanofibers,” *Phys. status solidi*, vol. 204, no. 6, pp. 1830–1834, Jun.

2007.

[62] K. W. Kim, K. H. Lee, M. S. Khil, Y. S. Ho, and H. Y. Kim, “The effect of molecular weight and the linear velocity of drum surface on the properties of electrospun poly(ethylene terephthalate) nonwovens,” *Fibers Polym.*, vol. 5, no. 2, pp. 122–127, 2004.

[63] C. L. Casper, J. S. Stephens, N. G. Tassi, D. B. Chase, and J. F. Rabolt, “Controlling surface morphology of electrospun polystyrene fibers: Effect of humidity and molecular weight in the electrospinning process,” *Macromolecules*, vol. 37, no. 2, pp. 573–578, Jan. 2004.

[64] S. Megelski, J. S. Stephens, D. Bruce Chase, and J. F. Rabolt, “Micro- and nanostructured surface morphology on electrospun polymer fibers,” *Macromolecules*, vol. 35, no. 22, pp. 8456–8466, Oct. 2002.

[65] D. H. Reneker and I. Chun, “Nanometre diameter fibres of polymer, produced by electrospinning,” *Nanotechnology*, vol. 7, no. 3, p. 216, 1996.

[66] C. Mit-Uppatham, M. Nithitanakul, and P. Supaphol, “Ultrafine electrospun polyamide-6 fibers: Effect of solution conditions on morphology and average fiber diameter,” *Macromol. Chem. Phys.*, vol. 205, no. 17, pp. 2327–2338, Nov. 2004.

[67] M. Cloupeau and B. Prunet-Foch, “Electrostatic Spraying of Liquids in Con-jet Mode,” 1989.

[68] M. Cloupeau and B. Prunet-Foch, “Electrohydrodynamic spraying functioning modes: a critical review,” *J. Aerosol Sci.*, vol. 25, no. 6, pp. 1021–1036, 1994.

[69] J. Rosell-Llompart, J. Grifoll, and I. G. Loscertales, “Electrosprays in the cone-jet mode: From Taylor cone formation to spray development,”

Journal of Aerosol Science, vol. 125. Elsevier Ltd, pp. 2–31, 01-Nov-2018.

[70] A. Jaworek and A. Krupa, “Classification of the Modes of EHD Spraying,” *J. Aerosol Sci.*, vol. 30, no. 7, 1999.

[71] A. Jaworek and A. Krupa, “Generation and characteristics of the precession mode of EHD spraying,” *J. Aerosol Sci.*, vol. 27, no. 1, pp. 75–77, 1996.

[72] A. Jaworek, W. Balachandran, A. Krupa, J. Kulon, and W. Machowski, “Electrohydrodynamic Atomization of Viscous Liquids,” 2003.

[73] Jaworek A and Krupa A, “Main Modes of Electrohydrodynamic Spraying of Liquids,” in *Third International Conference on Multiphase Flow, ICMF’98*, 1998.

[74] M. Cloupeau and B. Prunet-Foch, “Electrostatic spraying of liquids: Main functioning modes,” *J. Electrostat.*, vol. 25, no. 2, pp. 165–184, 1990.

[75] G. Taylor, “Disintegration of Water Drops in an Electric Field,” *Proc. R. Soc. A Math. Phys. Eng. Sci.*, vol. 280, no. 1382, pp. 383–397, Jul. 1964.

[76] Z. Wang, L. Tian, L. Xia, J. Dong, J. Wang, and J. Tu, “Experimental Study on Repetition Frequency of Drop/Jet Movement in Electro-Spraying of Deionized Water,” *Aerosol Air Qual. Res.*, vol. 18, pp. 301–313, 2018.

[77] S. Faraji, B. Sadri, B. Vajdi Hokmabad, N. Jadidoleslam, and E. Esmaeilzadeh, “Experimental study on the role of electrical conductivity in pulsating modes of electrospraying,” *Exp. Therm. Fluid Sci.*, vol. 81, pp. 327–335, Feb. 2017.

[78] A. Ponce-Torres, N. Rebollo-Munõz, M. A. Herrada, A. M. Ganãn-Calvo, and J. M. Montanero, “The steady cone-jet mode of electrospraying close to the minimum volume stability limit,” *J. Fluid Mech.*, vol. 857, pp. 142–172, Dec. 2018.

[79] P. D. Noymer and M. Garel, “Stability and atomization characteristics of electrohydrodynamic jets in the cone-jet and multi-jet modes,” *J. Aerosol Sci.*, vol. 31, no. 10, pp. 1165–1172, 2000.

[80] D. S. Jang, R. Jetli, and S. Acharya, “Comparison of the piso, simpler, and simplec algorithms for the treatment of the pressure-velocity coupling in steady flow problems,” *Numer. Heat Transf.*, vol. 10, no. 3, pp. 209–228, Sep. 1986.

[81] H. Khawaja and M. Moatamedi, “Semi-Implicit Method for Pressure-Linked Equations (SIMPLE)-solution in MATLAB®,” 2018.

[82] O. Lastow and W. Balachandran, “Numerical simulation of electrohydrodynamic (EHD) atomization,” *J. Electrostat.*, vol. 64, no. 12, pp. 850–859, 2006.

[83] K. Sarkar, P. Hoos, and A. Urias, “Numerical Simulation of Formation and Distortion of Taylor Cones,” *J. Nanotechnol. Eng. Med.*, vol. 3, no. 4, p. 41001, 2012.

[84] A. L. Yarin, S. Koombhongse, and D. H. Reneker, “Taylor cone and jetting from liquid droplets in electrospinning of nanofibers,” *J. Appl. Phys.*, vol. 90, no. 9, pp. 4836–4846, 2001.

[85] D. Sun, C. Chang, S. Li, and L. Lin, “Near-field electrospinning,” *Nano Lett.*, vol. 6, no. 4, pp. 839–842, 2006.

[86] X. Wu, R. D. Oleschuk, and N. M. Cann, “Characterization of microstructured fibre emitters: in pursuit of improved nano electrospray

ionization performance," *Analyst*, vol. 137, no. 18, pp. 4150–4161, 2012.

[87] R. P. A. Hartman, D. J. Brunner, D. M. A. Camelot, J. C. M. Marijnissen, and B. Scarlett, "Electrohydrodynamic atomization in the cone-jet mode physical modeling of the liquid cone and jet," *J. Aerosol Sci.*, vol. 30, no. 7, pp. 823–849, 1999.

[88] A. K. Sen, J. Darabi, D. R. Knapp, and J. Liu, "Modeling and characterization of a carbon fiber emitter for electrospray ionization," *J. Micromechanics Microengineering*, vol. 16, no. 3, p. 620, 2006.

[89] Chen and Chuan-Hua, *Electrohydrodynamic Stability*, vol. 530. Springer Vienna, 2011.

[90] W. K. H. Panofsky and M. Phillips, *Classical electricity and magnetism*. Courier Corporation, 2005.

[91] J. Fernández de La Mora, "The fluid dynamics of Taylor cones," *Annu. Rev. Fluid Mech.*, vol. 39, pp. 217–243, 2007.

[92] J. R. Melcher, *Continuum electromechanics*, vol. 2. MIT press Cambridge, 1981.

[93] ESI-GROUP, "CFD-ACE+ 2016.0 Manual ." ESI Group, France, pp. 507–531, 2016.

[94] V. Benci and L. Luperi Baglini, "A generalization of Gauss' divergence theorem," 2015.

[95] C. W. Hirt and B. D. Nichols, "Volume of fluid (VoF) method for the dynamics of free boundaries," *J. Comput. Phys.*, vol. 39, no. 1, pp. 201–225, 1981.

[96] Peterson and Richard, "The Numerical Solution of Free-Surface Problems for Incompressible, Newtonian Fluids," The University of

Leeds, The University of Leeda, 1999.

[97] G. K. Karch, F. Sadlo, C. Meister, P. Rauschenberger, K. Eisenschmidt, B. Weigand, and T. Ertl, “Visualization of piecewise linear interface calculation,” pp. 121–128.

[98] T. Young, “An Essay on the Cohesion of Fluids,” *Philos. Trans. R. Soc. London*, vol. 95, no. 0, pp. 65–87, 1805.

[99] I. Vágó and M. Gyimesi, *Electromagnetic fields*. Akadémiai Kiadó, 1998.

[100] V. Shtern and R. Barrero, “Striking Features of Fluid Flows in Taylor Cones Related to Electrosprays,” *J. Aerosol Sci*, vol. 25, no. 6, pp. 1049–1063, 1994.

[101] S. N. Jayasinghe and A. Townsend-Nicholson, “Stable electric-field driven cone-jetting of concentrated biosuspensions,” *Lab Chip*, vol. 6, no. 8, pp. 1086–1090, 2006.

[102] R. T. Collins, M. T. Harris, and O. A. Basaran, “Breakup of electrified jets,” *J. Fluid Mech.*, vol. 588, pp. 75–129, Oct. 2007.

[103] J. M. Lopez-Herrera, A. M. Ganan-Calvo, S. Popinet, M. A. Herrada, J. M. López-Herrera, and A. M. Gañán-Calvo, “Electrokinetic effects in the breakup of electrified jets: a Volume-Of-Fluid numerical study,” *Int. J. Multiph. Flow*, vol. 71, pp. 14–22, 2015.

[104] J. Bae, J. Lee, and S. Hyun Kim, “Effects of polymer properties on jetting performance of electrohydrodynamic printing,” *J. Appl. Polym. Sci.*, vol. 134, no. 35, p. 45044, Sep. 2017.

[105] S. E. Park, J. Y. Hwang, K. Kim, B. Jung, W. Kim, and J. Hwang, “Spray deposition of electrohydrodynamically atomized polymer mixture for active layer fabrication in organic photovoltaics,” in *Solar*

Energy Materials and Solar Cells, 2011, vol. 95, no. 1, pp. 352–356.

[106] N. V. Krasnov and S. I. Shevchenko, “Comprehensive studies of electrohydrodynamic spraying of liquids,” *Rev. Sci. Instrum.*, vol. 66, no. 6, pp. 3623–3626, 1995.

[107] C. H. Chen, D. A. Seville, and I. A. Aksay, “Scaling laws for pulsed electrohydrodynamic drop formation,” *Appl. Phys. Lett.*, vol. 89, no. 12, 2006.

[108] P. K. Baumgarten, “Electrostatic spinning of acrylic microfibers,” *J. Colloid Interface Sci.*, vol. 36, no. 1, pp. 71–79, 1971.

[109] M. J. Laudenslager and W. M. Sigmund, “Electrospinning,” in *Encyclopedia of Nanotechnology*, B. Bhushan, Ed. Dordrecht: Springer Netherlands, 2012, pp. 769–775.

[110] A. Jaworek, W. Machowski, A. Krupa, and W. Balachandran, “Viscosity effect on electrohydrodynamic (EHD) spraying of liquids,” 1999.

[111] A. Jaworek, W. Machowski, A. Krupa, and W. Balachandran, “Viscosity effect on EHD spraying using AC superimposed on DC electric field,” *Conf. Rec. - IAS Annu. Meet. (IEEE Ind. Appl. Soc.*, 2000.

[112] D. R. Chen and D. Y. H. Pui, “Experimental investigation of scaling laws for electrospraying: Dielectric constant effect,” *Aerosol Sci. Technol.*, vol. 27, no. 3, pp. 367–380, Sep. 1997.

[113] S. Zargham, S. Bazgir, A. Tavakoli, A. S. Rashidi, and R. Damerchely, “The Effect of Flow Rate on Morphology and Deposition Area of Electrospun Nylon 6 Nanofiber,” *J. Eng. Fiber. Fabr.*, vol. 7, no. 4, p. 155892501200700, Dec. 2012.

[114] A. Haider, S. Haider, and I. K. Kang, “A comprehensive review summarizing the effect of electrospinning parameters and potential

applications of nanofibers in biomedical and biotechnology," *Arabian Journal of Chemistry*, vol. 11, no. 8. Elsevier B.V., pp. 1165–1188, 01-Dec-2018.

[115] J. Bae, J. Lee, and S. Hyun Kim, "Effects of polymer properties on jetting performance of electrohydrodynamic printing," *J. Appl. Polym. Sci.*, vol. 134, no. 35, Sep. 2017.

[116] A. Barrero, A. M. Gañán-Calvo, J. Dávila, A. Palacios, and E. Gómez-González, "The role of the electrical conductivity and viscosity on the motions inside Taylor cones," *J. Electrostat.*, vol. 47, no. 1–2, pp. 13–26, 1999.

[117] "What is Zeta Potential." [Online]. Available: https://www.brookhaveninstruments.com/what-is-zeta-potential. [Accessed: 02-Aug-2018].

[118] "Electric polarization | physics | Britannica." [Online]. Available: https://www.britannica.com/science/electric-polarization. [Accessed: 19-Dec-2019].

[119] "Debye screening - what it is and how it affects zeta." [Online]. Available: https://www.materials-talks.com/blog/2018/10/03/debye-screening-how-it-affects-zeta-potential/. [Accessed: 19-Dec-2019].